Chair of Designing Plastics and Composite Materials

Master's Thesis

# Implementation of a finite element model to predict the impact behaviour of 3D-printed PMMA specimens

Christian Moser, BSc

June 2020

MONTANUNIVERSITÄT LEOBEN
www.unileoben.ac.at

# AFFIDAVIT

I declare on oath that I wrote this thesis independently, did not use other than the specified sources and aids, and did not otherwise use any unauthorized aids.

I declare that I have read, understood, and complied with the guidelines of the senate of the Montanuniversität Leoben for "Good Scientific Practice".

Furthermore, I declare that the electronic and printed version of the submitted thesis are identical, both, formally and with regard to content.

Date 08.06.2020

Signature Author
Christian, Moser

# Acknowledgements

First of all, I would like to thank all people who supported me during my study at Montanuniversitaet Leoben.

I would like to thank the colleagues at the chair of Designing Plastics and Composite Materials who supported me in terms of scientific knowledge as well as formal aspects of writing this thesis.

In particular, I would like to thank Univ.-Prof. Dipl.-Ing. Dr.techn. Clara Schuecker for giving me the opportunity to work at her chair during my studies. This employment equipped me with additional knowledge in the field of Polymer Science and Engineering. Furthermore, I would like to thank her for enabling and reviewing not only this master's thesis but also my bachelor's thesis. Apart from that, she gave me an understanding of the complex topic of material damage modelling and common unwanted effects when used in finite element modelling.

Special thanks go to my supervisor Dipl.-Ing. Dr.mont. Martin Pletz who was always on hand with help and advice during the whole progress of this thesis. This is also true for my bachelor's thesis as well as my employment at the chair of Designing Plastics and Composite Materials. Without him, this master's thesis would not be at this scientific level.

I thank Dipl.-Ing. Dr.mont. Martin Spoerk and Dipl.-Ing. Lukas Hentschel (Chair of Polymer Processing). They provided me with detailed information on the process parameters for the parts which were already 3D-printed before I started this thesis. Moreover, they manufactured all the test specimens with varying infill geometries necessary for completing this thesis.

Furthermore, I would like to thank Dipl.-Ing. Sandra Petersmann (Chair of Materials Science and Testing of Polymers) for executing all impact tests required for my thesis and providing me with all data necessary to evaluate the results.

Finally I thank my mother, Mag. Karin Moser, for making this study possible and supporting me all these years. Without her, the completion of my study and this thesis would not have been possible.

# Abstract

In this thesis, the impact behaviour of 3D-printed PMMA (poly-methyl-methacrylate) specimens is predicted using Finite Element modelling. As an example, cranial implants have to withstand impact loads, while the 3D-printing process allows production of complex geometries. The ideal infill geometry to perform well under impact (i.e. absorb more energy than other geometries) is not known beforehand. The goal of this thesis is to find the best performing infill structure using Finite Element modelling instead of manufacturing and testing possible infill geometries.

In collaboration with the chairs of Polymer Processing as well as Materials Science and Testing of Polymers of Montanuniversitaet Leoben, solid specimens were 3D-printed and tested according to the standard for impact testing of polymers. The experimental setup was modelled and the results of the solid specimens were the basis for calibrating two material models to predict the absorbed energy during impact. The test specimens' damage and failure behaviour is reproduced using a material damage model. The brittle damage model in ABAQUS represented the test results best. To use the brittle damage model, the material law has to be isotropic and linear elastic. Nevertheless, the damaged material behaviour is anisotropic because the distributed damage is modelled via stiffness degradation in the direction of loading. To evaluate these material models, an alternative infill structure was manufactured and tested. The test results were then compared to the predicted simulation results. Furthermore, the results of both infill structures were considered for the calibration of a third material model. To evaluate the prediction quality of those three material models, two new geometries were manufactured and their simulation results compared to the test results. Two out of the three calibrated material models gave a qualitatively correct prediction for the absorbed energy. This means that the FE models answer the question which infill geometries perform better (i.e. absorb more energy) during impact. However, when it comes to the absolute values of absorbed energy, the simulation results deviate from the test results. For the main issue of this work, which was to find infill geometries which perform better than others during impact, the qualitatively correct results are a satisfying outcome. The quantitative results might be improved in future work by implementing an enhanced material law in combination with the calibrated damage models.

# Kurzfassung

In dieser Arbeit wird das Schlagverhalten von 3D-gedruckten PMMA (Polymethylmethacrylat) Prüfkörpern mit Hilfe der Finite-Elemente-Modellierung vorhergesagt. Beispielsweise müssen Schädelimplantate Stoßbelastungen standhalten, während das 3D-Druck-Verfahren die Herstellung komplexer Geometrien ermöglicht. Die ideale Füllstruktur, die bei Stoßbelastungen mehr Energie absorbiert als andere Strukturen, ist zunächst nicht bekannt. Das Ziel dieser Arbeit ist es, die am besten geeignete Füllstruktur mit Hilfe der Finite-Elemente-Modellierung zu bestimmen, anstatt mögliche Strukturen herzustellen und zu testen.

In Zusammenarbeit mit den Lehrstühlen für Kunststoffverarbeitung sowie Werkstoffkunde und Prüfung der Kunststoffe an der Montnuniversität Leoben wurden voll gefüllte Prüfkörper 3D-gedruckt und entsprechend der Norm für die Schlagprüfung von Polymeren geprüft. Der Versuchsaufbau wurde modelliert und die Ergebnisse der Prüfkörper bildeten die Grundlage für die Kalibrierung von zwei Materialmodellen zur Vorhersage der absorbierten Energie während des Einschlags. Das Schädigungs- und Versagensverhalten der Prüfkörper wird mit Hilfe eines Schädigungsmodells für das Material abgebildet. Das spröde Schädigungsmodell in ABAQUS bildete die Versuchsergebnisse am besten ab. Um dieses Schädigungsmodell zu verwenden, muss das Materialgesetz isotrop und linear-elastisch sein. Dennoch ist das geschädigte Materialverhalten anisotrop, da die Schädigung in Form von Steifigkeitsabbau in Belastungsrichtung modelliert wird. Um diese Materialmodelle zu bewerten, wurde eine alternative Füllstruktur hergestellt und getestet. Die Testergebnisse wurden dann mit den Vorhersagen der Simulationen verglichen. Darüber hinaus wurden die Ergebnisse beider Füllstrukturen für die Kalibrierung eines dritten Materialmodells berücksichtigt. Um die Vorhersagequalität dieser drei Materialmodelle zu bewerten, wurden zwei neue Geometrien hergestellt und ihre Simulationsergebnisse mit den Testergebnissen verglichen. Zwei der drei kalibrierten Materialmodelle ergaben eine qualitativ korrekte Vorhersage in Bezug auf die absorbierte Energie. Dies bedeutet, dass die FE-Modelle die Frage beantworten, welche Füllstrukturen bei Schlagbelastung besser abschneiden (d.h. mehr Energie absorbieren). Wenn es jedoch um die absoluten Werte der absorbierten Energie geht, weichen die Simulationsergebnisse von den Testergebnissen ab. Die Aufgabenstellung dieser Arbeit lautete, Füllstrukturen zu finden, die mehr Energie absorbieren als andere. Hierfür sind die qualitativ korrekten Vorhersagen ein zufriedenstellendes Ergebnis. Die quantitativen Ergebnisse könnten in zukünftigen Arbeiten durch die Implementierung eines erweiterten Materialgesetzes in Kombination mit den kalibrierten Schädigungsmodellen verbessert werden.

# Table of Contents

# 1 Introduction

Due to an ageing population and the increase of traumatic injuries, reconstructive surgery of bones is becoming more frequent with about 500 000 bone graft procedures each year in the United States [1]. Therefore, previous research evaluated suitable materials for implants inserted in the skull (cranial implants) among which there is the material class of polymers. The medical use of synthetic polymers dates back to the 1960s as materials for syringes and catheters. Nowadays, polymers are used in a wide variety of medical applications such as disposables or long-term implants. The most important reason polymers are used instead of metals is that sterility can easily be achieved. This property is also relevant for research regarding cranial implants. The popularity of polymer materials in medical engineering is a consequence of their easy and inexpensive processability allowing to produce complex geometries. In case of cranial implants, the materials employed have to fulfill requirements such as biocompatibility, adequate mechanical properties and long-term stability within the human body [2].

For medical applications, the processability of certain polymers via additive manufacturing techniques is of special interest. Materials suitable for the so-called 3D-printing process are standard polymers like poly-methyl-methacrylate (PMMA), acrylonitrile-butadiene-styrole (ABS) and poly-styrene (PS), as well as engineering polymers like poly-amides (PA). High performance plastics such as poly-ether-ether-ketone (PEEK) and plastics gained from renewable resources (bioplastics), namely poly-lactide (PLA), are further options with ABS, PLA, PMMA and PEEK being the more commonly used materials [3]. For cranial implants, ABS and PLA are not the material of choice as the one named first is not biocompatible, while the latter is biodegradable which means that it is only suitable for short-term implants which are designed to decompose after a certain time in the body [4]. PMMA and PEEK feature several properties which make them suitable materials for long-term implants such as biological inertia and biomechanical properties close to those found in bone [5, 6]. An advantage of PMMA is that it is a rather low cost material contrary to the expensive PEEK [7].

As a consequence, Petersmann et al. [8] chose the material PMMA to investigate the impact behaviour of 3D-printed plates with varied infill patterns and volume fractions of infill material. The researchers wanted to find infill structures which absorb as much energy as possible because this property is crucial for cranial implants

As producing and testing components is very expensive and time-consuming, in these days computer simulation plays a big role for part design. Therefore, the next step following Petersmann et al. work, is to implement a simulation model of the standardized impact test for rigid polymers in this work. The model represents the testing procedure according to *ÖNORM EN ISO 6603:2* [9]. As the material properties of 3D-printed mate-

rials differ from the properties of the same sort of polymer used for injection molding or extrusion [10], the core topic of this thesis is to develop a material model and also a damage model for the 3D-printed PMMA to fit the existing test data and predict the behaviour of various infill geometries. As a result, the model is used for optimizing the geometry to absorb as much energy as possible in the impact test.

# 2 Theory

In this chapter, the necessary theoretical knowledge and the software used for computing the loading of components are described. This helps to understand the approach followed in this thesis. This chapter also gives a first glance at what results acquired from an impact test are decisive for the task of maximizing energy absorption of the specimen.

## 2.1 Background

Firstly, the used software and some background information on the Finite Element Method (FE, respectively FEM) are given in this section. The first section shows the reasons for application of FE-simulation, while the second one describes the specific FE software used in this work – ABAQUS by Simulia (Dassault Systèmes, FR) [1]

### 2.1.1 Finite element method

The base idea of the finite element method is that in practice, the behaviour of loaded parts cannot always be calculated analytically. Therefore, numerical (approximative) computations are needed. In FEM, the continuous geometry is *discretised* generating a mesh representing the geometry. The mesh properties are of high importance as the mesh is responsible for the accuracy of the results. A common application of FE is to apply mechanical loads (e.g. forces or displacements) – which are known or expected to act on the part or assembly – and observe the stresses and strains that will occur during that certain situation. Nowadays, FE simulation is also used for thermal, acoustic, electrodynamic and many other problem formulations [11].

Finite element method for describing physical problems is a daily tool for engineers as they are an alternative to very costly experimental methods [12]. Especially for 3D-printed parts it is also a time-saving routine to set up a numerical model and compute the effects of certain load cases instead of manufacturing and testing the desired specimens.

The results obtained from FE simulations are the basis for the designing process. Correctly interpreted, the output information helps to adjust the geometry of parts based on the loading situation to fulfill certain predefined requirements. Furthermore, a material can be selected based on simulation results without dealing with possibly varying manufacturing processes and tooling for the specific materials which again saves time and lowers the cost of the designing process.

[1] https://www.3ds.com/

### 2.1.2 ABAQUS

As previously mentioned, the FE software used in this work is ABAQUS (Simulia, Dassault Systèmes, FR) [13]. This software covers all processes necessary for a finite element computation: setting up a model (pre-processing), computing the numerical results and illustrating and evaluating the results for interpretation (post-processing). Pre-processing means that all necessary data in order to be able to compute the physical values of interest is given to the software. So, in pre-processing, the geometry and its discretization (mesh), material model, assembly, contact definition and loading scenarios are defined.

ABAQUS offers a range of solvers. The most important keywords regarding FE solvers are *implicit* and *explicit* and describe the used time-stepping method. In the implicit approach, a solution of the set of finite element equations involves iteration until a convergence criterion is satisfied for each increment. Contrary to that, in the explicit approach, the finite element equations are formulated in another way to be directly solvable. As a result, the solution at the end of the increment is determined without iteration [14]. The implicit method leads to solutions that are unconditionally stable and facilitate larger time steps. Despite this advantage, the implicit method can be extremely time-consuming when solving dynamic and nonlinear problems. Contrary to that, explicit computation offers a faster solution for dynamic problem formulations which might be high strain rates or velocities occurring during the simulation [15]. Contrary to the implicit approach, in the explicit approach only small time regions can be covered efficiently. Summed up, the implicit approach is mostly used for quasi-static or time-independent problems in which as a best-case scenario, no non-linearities occur, while, as a rule of thumb, explicit approach is used for dynamic (time-dependent) loading scenarios.

The software ABAQUS is used in this work to automize the generation of models using the scripting language *Python*[2]. All operations which can be done using the graphical user interface (GUI) can also be executed using Python. Doing so, the creation and simulation of many similar models with certain variable parameters can be accelerated drastically [16].

## 2.2 State of the art

In this section, the chosen material and standardized impact test for solid polymers are briefly described. Furthermore, relevant research dealing with impact simulation of brittle materials is summarized, because the general approach of these publications can be adapted for this thesis. Then, the basis of this thesis – the impact testing of 3D-printed PMMA plates with varied infill structures – is described in more detail.

[2] https://www.python.org/

### 2.2.1 Poly-methyl-methacrylate (PMMA)

Since this work follows the research of Petersmann et al. [8], the material of the specimens in the impact test and in the model is a grade of poly-methyl-methacrylate (PMMA) for 3D-printing (Herz, Austria). PMMA is an amorphous and brittle polymer with its chemical structure shown in Figure 2.1. Additionally, it is transparent, weatherproof and rather stiff for a polymer material with a Young's modulus of about $3000\,\mathrm{MPa}$ depending on the grade. These are the reasons why PMMA is suitable for outdoor applications. The material is well-known for its trademark names Plexiglas© (Röhm), Degalan© (Evonik), Altuglas© (Arkema) and Acrylite© (Evonik Cyro) [17, 18]. While the mechanical properties of PMMA grades that have been used for many years as material in manufacturing processes like injection molding and extrusion are well documented, the evaluation of a PMMA based 3D-printing process exposed that the mechanical properties of 3D-printed PMMA differ from that values [10].

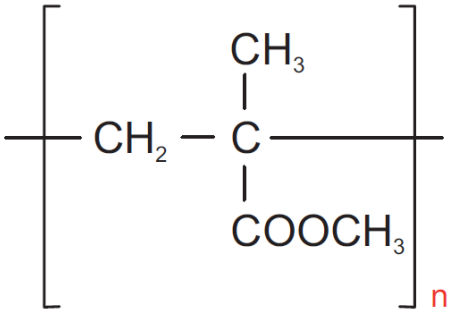


Figure 2.1: Chemical structure of PMMA according to [19].

### 2.2.2 Determination of the impact behaviour of plastics

In this section, the impact test procedure according to *ÖNORM EN ISO 6603:2* [9] is briefly described. This test was performed in the work of Petersmann et al. [8] for the manufactured specimen geometries and is replicated in the simulation model. In this scenario, the test specimen is punctured at its centre using a lubricated striker. The striker is aligned perpendicularly to the test specimen surface and pierces through the test specimen at nearly uniform velocity. The result is a force-displacement or force-time diagram. In Figure 2.2, the schematic with all components according to Seidler, Altstädt, Grellmann [20] is shown.

According to the standard, the striker's tip is a hemisphere for which the diameter of choice is $20\,\mathrm{mm}$. The striker's surface is lubricated, so that the friction between the striker and test specimen is reduced. The clamping device consists of two parts, a supporting ring and a clamping ring. The inside diameter of both rings is suggested to be $40\,\mathrm{mm}$. A recommended clamping force of $3\,\mathrm{kN}$ is applied on the clamping ring. This force leads to a contact pressure of approximately $1.3\,\mathrm{MPa}$ regarding the contact surface with the specimen. The preferred impact velocity of the striker is $4.4\,\mathrm{m/s}$.

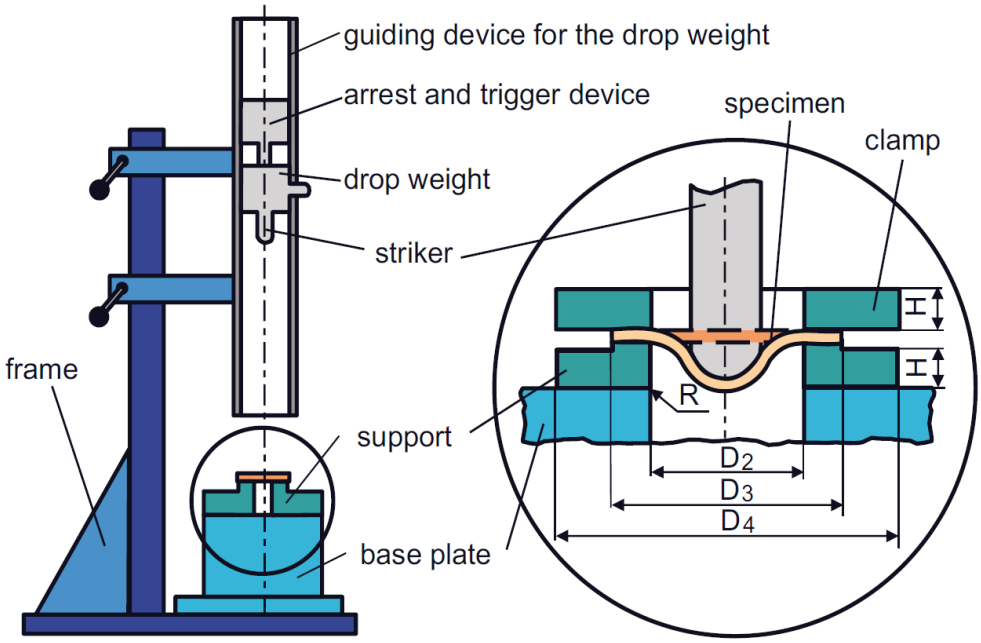


Figure 2.2: Schematic view of the impact test according to [20].

### 2.2.3 Damage modelling

These days there are numerous methods of modelling damage, divided into Continuum Damage Mechanics (CDM) and Fracture Mechanics (FM). In ABAQUS, there are several models of continuum damage mechanics for ductile, brittle and composite materials implemented. Furthermore, there are many ways to model crack extension using fracture mechanics available in ABAQUS. However, this section concentrates on the theoretical background of both methods rather than describing the implemented models within ABAQUS in detail.

#### 2.2.3.1 Continuum Damage Mechanics

Generally, Continuum Damage Mechanics (CDM) is used to model the effects of defects at the macroscopic scale. In a 1D approach, the CDM approach is based on using the effective cross-sectional area in a uniaxial tensile test. In Figure 2.3, the reduced cross-sectional area due to material damage is shown, which is the nominal area $S$ reduced by the damaged area $S_{\mathrm{D}}$. The fraction of the defects to the nominal area $D$ (Equation 2.1) is commonly considered as a damage variable [21].

$$D = \frac{S_{\mathrm{D}}}{S} \tag{2.1}$$

With the definition of $D$ above, the damage variable lies between $0$ and $1$. While $D = 0$ means that the material is undamaged, the material is fully broken if $D = 1$. In the range between those values ($0 < D < 1$), damage has occurred in the material. Using the damage variable $D$ from equation 2.1, the effective stress (Equation 2.2) can be expressed using $D$, as described in Equation 2.3:

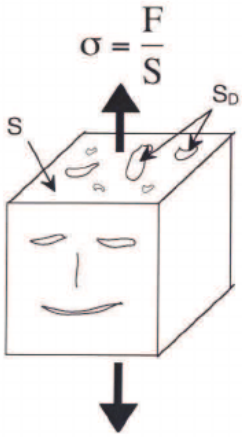


Figure 2.3: Cross section of a damaged material according to [22]

$$\sigma_{\text{eff.}} = \frac{F}{S - S_{\text{D}}} \tag{2.2}$$

$$\sigma_{\text{eff.}} = \frac{\sigma}{1 - D} \tag{2.3}$$

This definition is the effective stress for tensile loading. In compression, defects can close and therefore the effective surface is larger than $S$ - $S_{\text{D}}$. For the case that all defects close, the effective compressive stress is equal to the nominal stress. Using Hooke's Law [23], the effective strain and as a result the elasticity modulus of the damaged material $E_{\text{d}}$ is:

$$E_{\text{d}} = E(1 - D) \tag{2.4}$$

A straightforward 3D extension of this uniaxial theory is the approach of Lemaitre and Chaboche [24]. In this model, the stiffness tensor $\underline{\underline{C_{\text{d}}}}$ of the damaged material is defined as:

$$\underline{\underline{C_{\text{d}}}} = \underline{\underline{C}}(1 - D) \tag{2.5}$$

Summarized, in CDM, an increasing amount of damage in the material leads to a decrease in material stiffness [21].

In FE-Software, there are different CDM models implemented with criteria for damage initiation and damage evolution. Two specific FE implementations are mentioned here, as they will be used in this thesis, namely the ductile and the brittle damage model in ABAQUS.

The damage initiation criterion used in the ductile damage model introduces an equivalent plastic strain at damage onset $\varepsilon_{\mathrm{D}}^{pl}$, which is dependent on the stress triaxiality $\eta$ and the equivalent plastic strain rate $\dot{\varepsilon}^{pl}$. The criterion of damage initiation is defined as follows:

$$D = \int \frac{d\varepsilon^{pl}}{\varepsilon_{\mathrm{D}}^{pl}(\eta, \dot{\varepsilon}^{pl})} = 1 \tag{2.6}$$

Once the damage initiation criterion has been reached, ABAQUS defines the effective plastic displacement $\dot{u}^{pl}$ evolution using the characteristic element length $L$ and the plastic strain rate $\dot{\varepsilon}^{pl}$ (Equation 2.7). Setting $u_{fail}^{pl}$ to $0$ would lead to instantaneous failure.

$$\dot{u}^{pl} = L \cdot \dot{\varepsilon}^{pl} \tag{2.7}$$

While the ductile damage model in ABAQUS needs an isotropic, elastoplastic material law, the brittle damage model only supports an isotropic and linear elastic material law prior to damage initiation. Nevertheless, the damaged material of the brittle damage model becomes anisotropic because damage is modelled via stiffness degradation that is dependent on the direction of loading. Figure 2.4 shows the schematic stress-strain curves to be modelled using the two mentioned material models with the plastic area in the material law being highlighted for the ductile damage model.

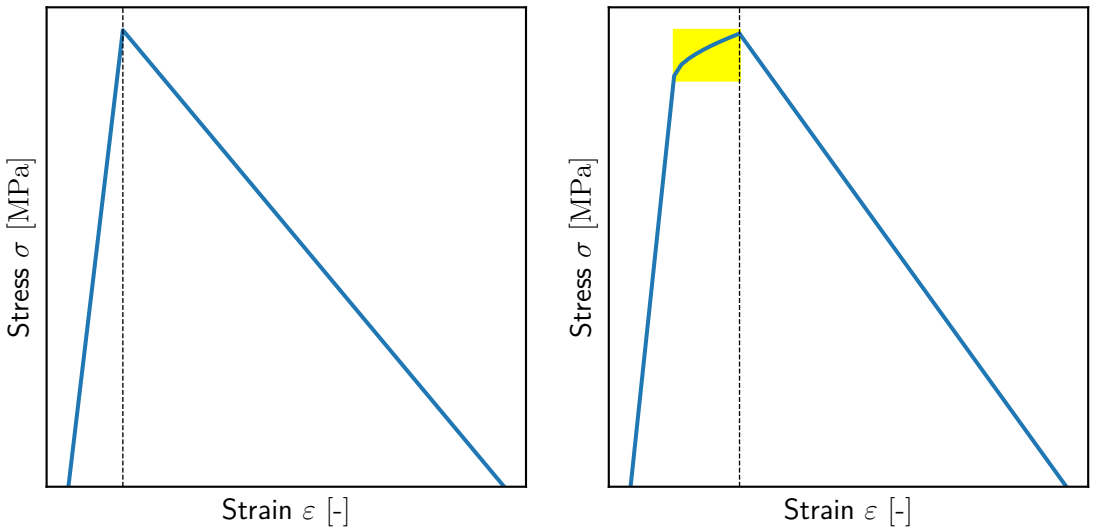


(a) Schematic stress-strain curve for the brittle damage model.

(b) Schematic stress-strain curve for the ductile damage model with the plastic region highlighted.

Figure 2.4: Comparison of stress-strain curves to be modelled using (a) the brittle damage model and (b) the ductile damage model. The dashed line marks the beginning of damage.

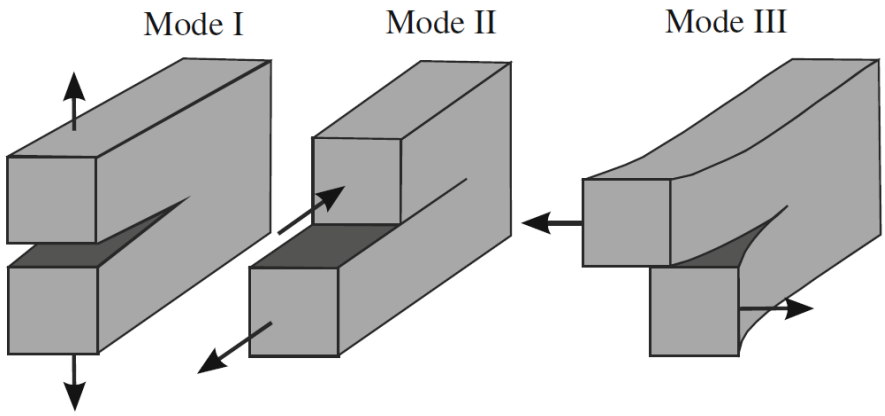


Figure 2.5: Definition of the crack load modes

#### 2.2.3.2 Fracture Mechanics

The basic idea of Fracture Mechanics (FM) is that fracture is the result of crack propagation, starting with an initial imperfection. Therefore, FM describes if a crack does or does not propagate. This section concentrates only on Linear Elastic Fracture Mechanics (LEFM). In LEFM it is assumed that in the region of crack propagation, no plastic deformation occurs. For plastic deformations, there are several other concepts such as the J-Integral-Concept, the Crack-Tip-Opening Displacement (CTOD) Concept and the Crack Resistance (R-) Curve Concept [20].

There are three modes in which a crack can be opened. The most critical is a tensile opening of the crack which is referred to as mode I. The three modes of crack opening are shown in Figure 2.5.

The so-called *K-concept* in LEFM expresses the stress state near the crack tip using a stress intensity factor $K$. The stress intensity factor which is dependent on the nominal stress $\sigma_{\mathrm{N}}$ and the crack length $a$ is defined according to equation 2.8. The stress intensity factor depends on the geometry, which is symbolised in equation 2.8 with $f(geometry)$. A higher stress intensity factor means that the factor of the singularity is different, which is schematically shown in Figure 2.6. Due to the assumption of no plastic zone at the crack tip, in LEFM there is a stress singularity at the crack tip.

$$K = \sigma_{\mathrm{N}} \sqrt{\pi\ a} \cdot f(geometry) \tag{2.8}$$

A crack under mode I loading starts to propagate if the stress intensity factor for mode I loading $K_{\mathrm{I}}$ reaches the value of $K_{\mathrm{IC}}$ which is called the mode I fracture toughness. Therefore, there is no crack propagation as long as $K_{\mathrm{I}} < K_{\mathrm{IC}}$ [20]. The index I in this case refers to mode I loading, which is, as previously mentioned, the most critical loading scenario.

Another concept is based on energy balance during crack propagation [25]. During crack propagation there is dissipative energy $\mathcal{D}$ consumed. The dissipative energy is di-

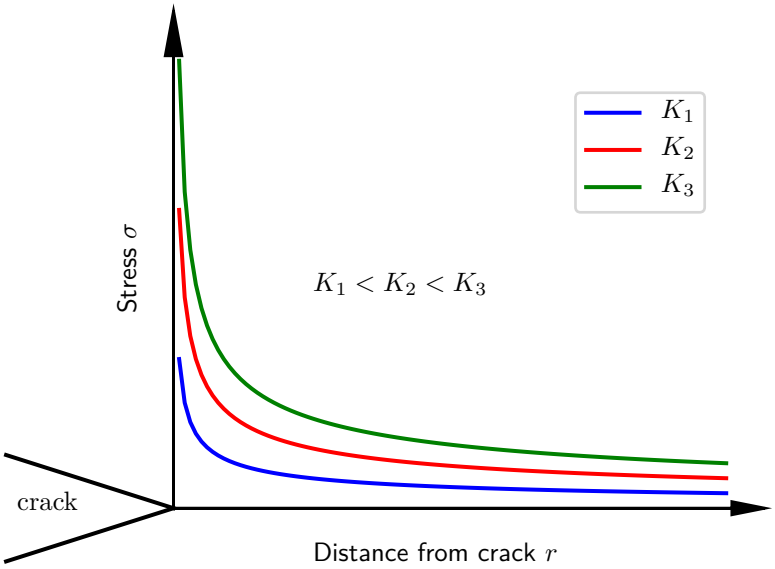


Figure 2.6: Schematic comparison of stress distributions close to the crack for varied $K$ values.

rectly related to the creation of new surfaces. Therefore, it is proportional to the change in crack area $\Delta A$ and the material constant $\gamma$. As for crack propagation 2 new surfaces have to be created, the factor 2 is needed in the expression for $\mathcal{D}$ (equation 2.9). The change in dissipated energy per change in crack area can then be expressed with the material constant $\gamma$. Considering the total potential $\Pi$ which decreases as energy is dissipated, the energy for creating 2 new surfaces can be expressed using $\Pi$ instead of $\mathcal{D}$ (equation 2.10).

$$\mathcal{D} = 2\gamma A \tag{2.9}$$

$$\frac{\Delta \mathcal{D}}{\Delta A} = 2\gamma = -\frac{\Delta \Pi}{\Delta A} \tag{2.10}$$

The right-hand side describes the available potential energy $-\Delta\Pi$ which is supplied by an external load and the stored internal energy during crack propagation. This expression is called energy release rate $G$. In equation 2.11, the expression for $G$ is given for infinitesimal crack propagation is given.

$$G = -\frac{d\Pi}{dA} \tag{2.11}$$

The fracture criterion for this concept is that the critical energy release rate $G_{\mathrm{C}}$ is two times $\gamma$ as this enables the crack to propagate and develop two new surfaces. Summed up, there is no crack propagation as long as the following equation is fulfilled:

$$G < G_{\mathrm{c}} \tag{2.12}$$

With equation 2.11 and $G_{\mathrm{C}} = 2\gamma$:

$$-\frac{d\Pi}{dA} < 2\gamma \tag{2.13}$$

For an isotropic, homogenous material there is a correlation between the infinitesimal energy release rate $G_{\mathrm{I}}$ and the stress intensity factor $K_{\mathrm{I}}$ as stated by Kuna [25].

$$G_{\mathrm{I}} = \frac{K_{\mathrm{I}}^2}{E'} \tag{2.14}$$

$E'$ in this equation is equal to the Young's modulus $E$ for plane stress. For plane strain $E'$, is equal to $E/(1-\nu^2)$. This expression can also be used for the critical values of energy release rate $G_{\mathrm{C}}$ and the fracture toughness $K_{\mathrm{C}}$

$$G_{\mathrm{C}} = \frac{K_{\mathrm{C}}^2}{E'} \tag{2.15}$$

#### 2.2.3.3 Cohesive Zone Models

The approach of cohesive zone models is the assumption that failure occurs in a narrow strip-shaped zone in front of the main crack. Therefore, the damage of the material occurs only in this small region with the rest of the material remaining free of damage. The name Cohesive Zone Models dates back to Barenblatt [26], who first implemented such a model and referred to the small region in front of the crack tip as *cohesive zone*. In his approach, failure is modeled continuously and therefore the stress singularities at the crack tip disappear. This is an essential property of all cohesive zone models. Cohesive zone models are used for material failure occurring in a narrow band (e.g. delamination in compounds, adherenced components), transmitting force across the crack faces. This characteristic phenomena are also present in fiber-reinforced materials or polymers, where forces are transmitted by fiber pullout or by stretched molecular chains (crazes), as shown in Figure 2.7 [25]. In the Figure, $l_{\mathrm{cz}}$ stands for the length of the cohesive zone.

The central aspect of cohesive zone models is the function that describes the interaction force between the two interfaces (crack faces). This law is an interface property which is independent of the external load. Usually the *cohesive law* is a relation between the boundary tractions $\sigma$ and the distance between the two faces $\delta_{\mathrm{n}}$. There are many different cohesive laws which are different due to various materials and failure mechanisms. In Figure 2.8, some typical shapes of the traction $\sigma$ as a function of the separation $\delta$ are shown. Generally, stress increases at first until reaching a maximum $\sigma_{\mathrm{C}}$ which is called *cohesive strength*. After a certain separation $\delta_{\mathrm{C}}$, which is referred to as the *decohesion length*, no stress can be transmitted. Integrating the separation law according to equation 2.16, the area below the graph can be computed. This area is equal to the specific fracture energy per surface area $G_{\mathrm{C}}$ which was described in the previous section [25]. This correlation is also visualized in Figure 2.8.

$$\int_0^{\delta_{\mathrm{C}}} \sigma(\delta_{\mathrm{n}}) d\delta_{\mathrm{n}} = G_{\mathrm{C}} \tag{2.16}$$

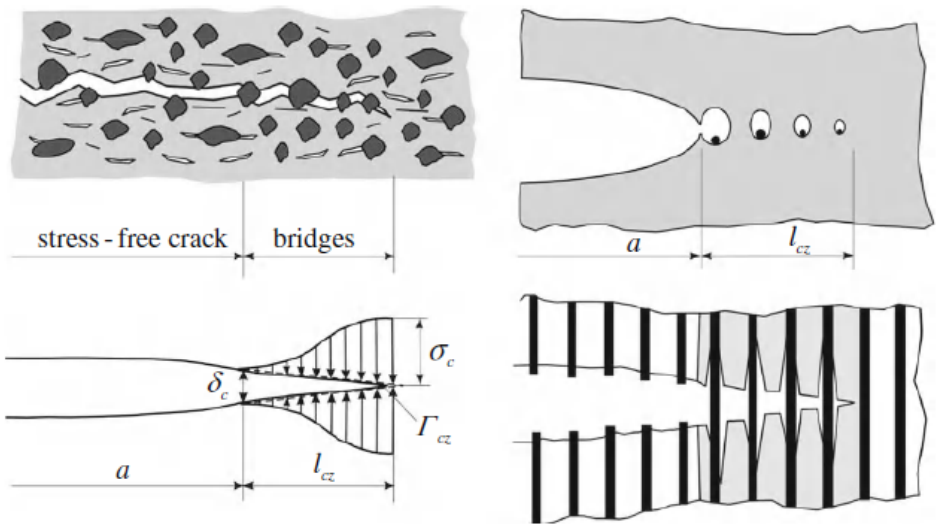


Figure 2.7: Example of a cohesive zone model and micromechanical explanations for (brittle) heterogeneous materials, ductile fracture and fiber reinforced composites according to [25].

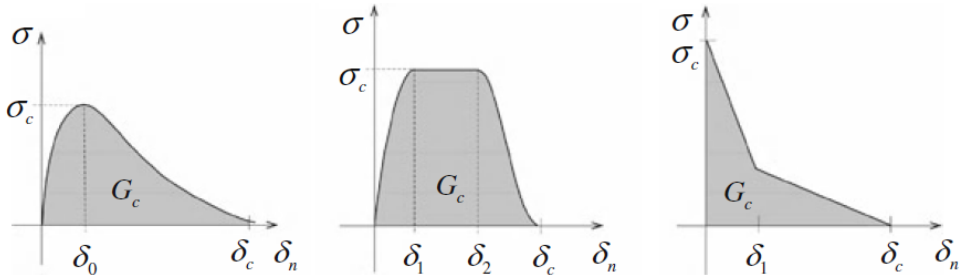


Figure 2.8: Typical shapes of cohesive laws according to [25].

The crack propagation criterion for this approach reads as follows: a crack initiates when $\delta_{\mathrm{n}} = \delta_{\mathrm{C}}$. The parameters needed for this damage model can be obtained from experiments. While $\sigma_{\mathrm{C}}$ can be obtained from the ultimate strength of the material, $G_{\mathrm{C}}$ is a result of fracture mechanics experiments. The critical separation $\delta_{\mathrm{C}}$ can be obtained from measurements of the fracture process zone [25].

### 2.2.4 Previous work on the damage behaviour of PMMA

Khan et al. [27] developed a material model to describe the brittle damage behaviour of plexiglas. Their approach was performing indentation tests first and then approximating the test data using FE analysis by varying the parameters of the material damage model. In their work, a sharp tip indenter was used. After the test, the load-deflection curve was evaluated and a FE model representing the test procedure was set up. With the load-deflection curve as a starting point, the stress-strain curve was calibrated as well as other material parameters (i.e. hardness and fracture toughness). Then, a mathematical expression to approximate the strain-dependent stress was developed in or-

der to model the material for the FE analysis. The stress-strain curve fitted to the observed test data is shown in Figure 2.9.

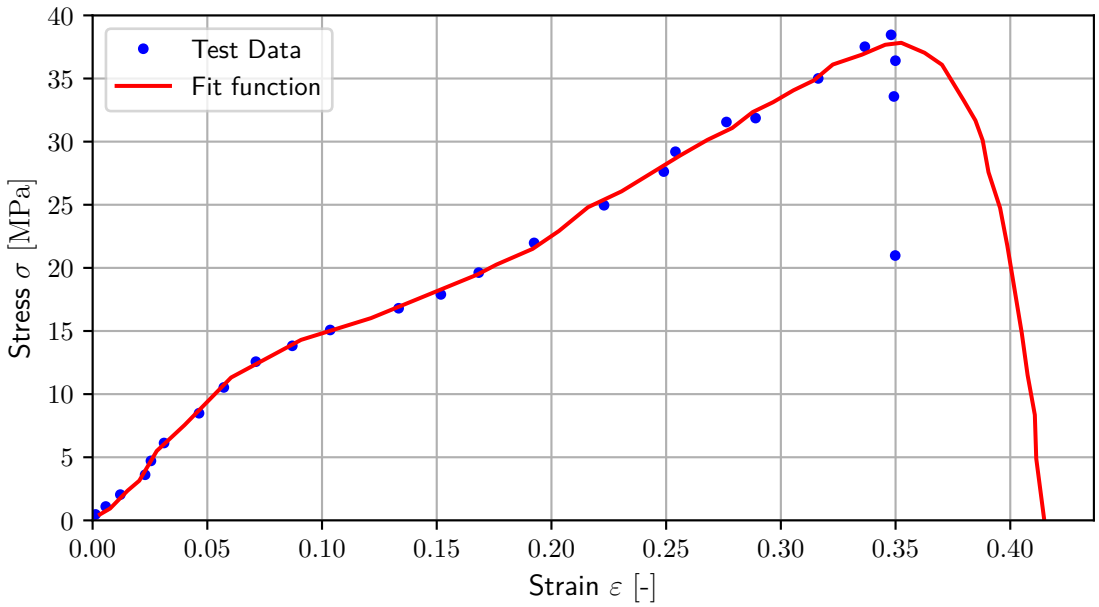


Figure 2.9: Stress-strain curve approximated to the indentation test results in [27].

Based on this curve, the damage parameters for the brittle cracking model implemented in the ABAQUS software were obtained and then varied until reaching a proper result as seen in Figure 2.10. In their work, the brittle cracking model allowed to get simulation results very close to the test data. This damage model uses a given post-cracking stress-strain curve which is applied on elements exceeding the specified failure-stress.

Summarized, the approach in their work was to fit the material model using the force-deflection curve test data to reproduce the test situation via FE simulation. This procedure can be adapted, considering that the test situation is quite different from the impact test described in Section 2.2.2. However, this difference in the experimental setup is only relevant for the geometrical setup of the model.

### 2.2.5 Optimization of energy absorption of 3D-printed PMMA plates under impact loading

Petersmann et al. [8] performed impact tests on PMMA plates with varied infill structures in order to find geometries that absorb more energy during impact than others. To ensure a better data acquisition, the impact velocity was set to $1\,\mathrm{m/s}$ contrary to the recommended $4.4\,\mathrm{m/s}$ mentioned in Section 2.2.2. The mass of the striker was increased to a total of $59.48\,\mathrm{kg}$ to guarantee full puncture with the velocity of the striker remaining nearly constant.

To produce parts via 3D-printing, the geometry has to be divided into horizontal layers. Within these layers, the 3D-printer extrudes the material along a path to form the part

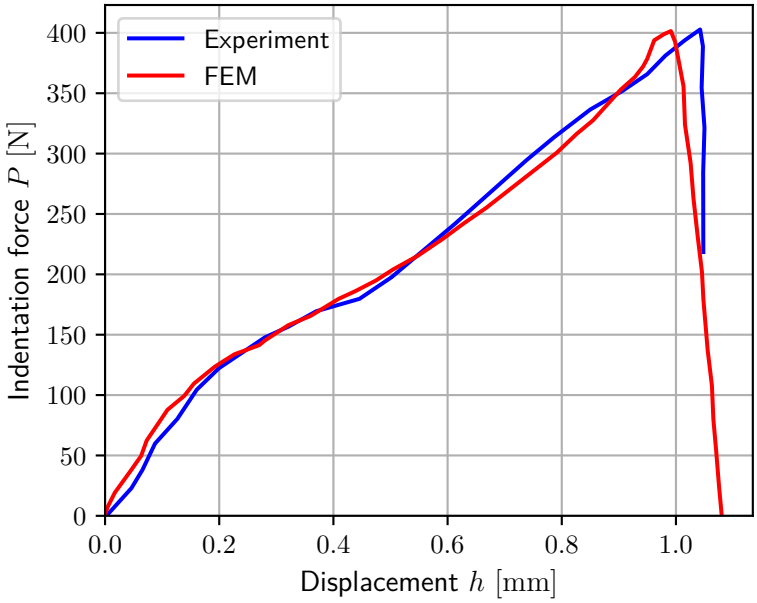


Figure 2.10: Comparison between the simulation and test results in [27].

geometry. This process of converting the geometry to a path the 3D-printer follows is called slicing [28]. For slicing, Petersmann et al. [8] used the software Slic3r Prusa Edition (Alessandro Ranellucci)[3]. In Figure 2.11, the dimensions of the test specimens as well as the tested infill structures implemented in the slicing software are shown. According to the illustration, each infill structure was manufactured with varying infill densities.

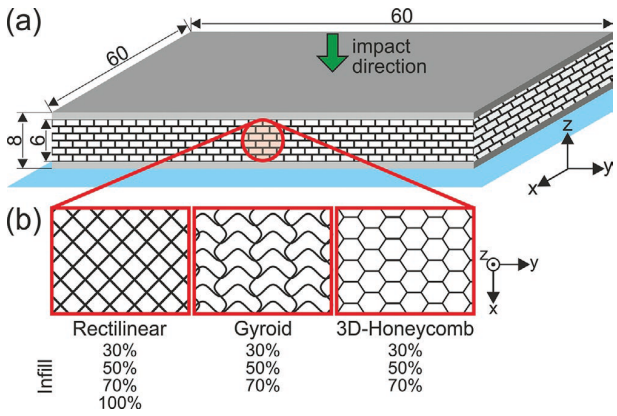


Figure 2.11: Schematic representation of the test specimen geometry with varying infill structures according to [8].

The tests have shown that the infill densities tremendously influence the failure behaviour of the test specimens (Figure 2.12). Thus, the same material shows smooth puncture at lower infill densities while failing due to cracks propagating throughout the specimens at higher infill densities.

[3]https://slic3r.org/

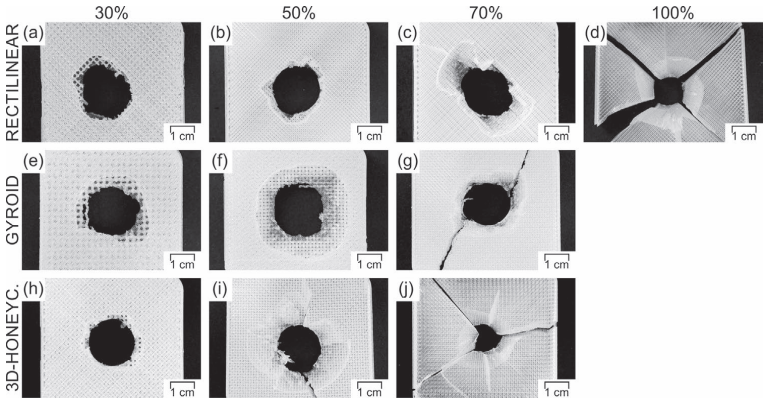


Figure 2.12: Comparison of the failure patterns due to varied infill structures and infill densities described in [8].

In their work, a topology optimization using the software OptiStruct (Altair, USA)[4] was performed. This was the first use of FE simulation on to find well performing inner structures in terms of energy absorption. Therefore, the loading scenario was represented by a Hertzian pressure distribution. The objective was to minimize the compliance of the part while constraining the remaining mass to $50\,\%$ of the completely filled plate. Another procedure was a material optimization, more specifically the inclusion of an elastomeric component besides the brittle PMMA material. This elastic component should increase the amount of absorbed energy as it acts as a crack stopper. The resulting geometry of the topology optimization as well as the material optimized stacking can be seen in Figure 2.13.

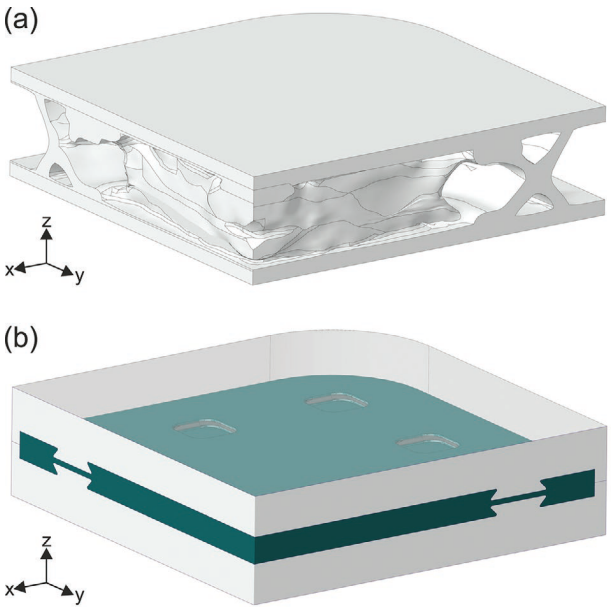


Figure 2.13: (a): Visualization of the geometry of the topology optimization and (b): the included elastic layer in order as material optimization mentioned in [8].

[4] https://www.altair.com/optistruct/

Both – topology and material optimized geometries – were manufactured and the force-displacement curves as well as the amount of absorbed energy were examined. In Figure 2.14, the definitions for common parameters in such force-displacement curves are given.

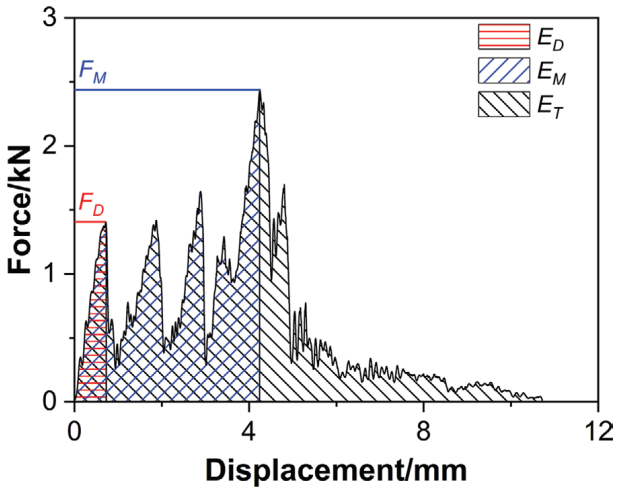


Figure 2.14: Definition of force ($F_D$) and energy at first damage ($E_D$), maximum global force ($F_M$) and energy at global force maximum ($E_M$) as well as total absorbed energy ($E_T$) exemplarily shown for the impact test performed on a PMMA sandwich plate with $50\,\%$ rectilinear infill [8].

# 3 Approach

In this chapter, the modeling of the impact test according to *ÖNORM EN ISO 6603:2* is described. The main aspects are the modelling of all relevant parts of the experimental set-up, the specimen geometry and the material model including the damage and failure model. The model build-up is done via a Python script and therefore, all parameters can be easily changed and variations be simulated without having to manually change the model. All parameters are entered into an Microsoft Excel table which is then read by the script which generates the model in ABAQUS.

At the end of this chapter, all relevant parameters for the test specimen's damage behaviour are listed as a summary. The others are described in the corresponding sections with the constant or initial values chosen.

## 3.1 Geometry of the model

### 3.1.1 Test setup

As mentioned in the previous chapter and seen in Figure 2.2 on page 6, there are several parts that have to be modeled in order to represent the experiment. These components are the clamping ring, the supporting ring and the striker. The rings are important to fix the position of the test specimen during the experiment and serve as the regions for applying the boundary conditions and loads in the model.

All parts except the test specimen are modeled as discrete rigid parts. *Discrete* means that the part has to be meshed and *rigid* means that the body is not deformable. The definition as rigid parts leads to a decrease in computation time. As the testing machine's components (e.g. the clamping) are much stiffer than the test specimen, the definition as rigid parts is valid. All parts are axisymmetrical with a constant cross section, therefore the cross sections are sketched in 2D and afterwards revolved around the center axis. All necessary components of the testing machine implemented in the model are shown in Figure 3.1.

The dimensions of the parts are taken from *ÖNORM EN ISO 6603:2* since the test set-up at Montanuniversitaet Leoben – according to [8] – is exactly the same. For the additional mass of the striker and the clamping force, the parameters from the tests in Leoben are used because they are not the same as the recommendations in the standard. In Figure 3.2, dimensional suggestions of the clamping and supporting ring according to the standard are shown. Table 3.1 shows all key parameters for the model besides the recommended values according to *ÖNORM EN ISO 6603:2* and the values used in the model to represent the experiments performed in Leoben. These values can all be changed

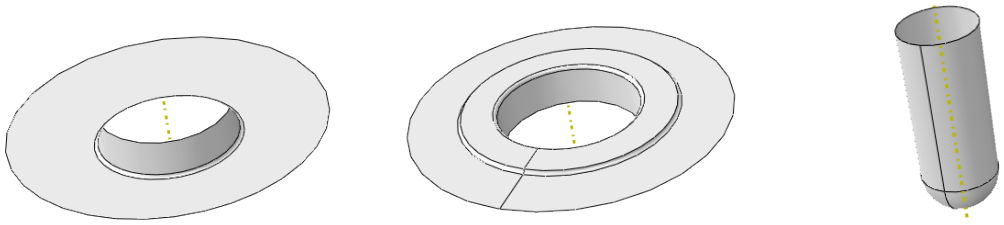

(a) Clamping ring (b) Supporting ring (c) Striker

Figure 3.1: Visualization of the different parts used in the model

within the Excel sheet. However, as in this thesis the experiments should be reproduced, the values used in the experiment are implemented in the model and remain unchanged through all stages of this thesis.

Dimensions in millimetres

| Specimen type | Side of square or diameter of disc | |
|---|---|---|
| | 60 | 140 |
| $D_2$ | 40 ± 2 | 100 ± 5 |
| $D_3$ | 60 | 140 |
| $D_4$ | ⩾ 90 | ⩾ 200 |
| $H$ | 12 | 12 |
| $R$ | 1 | 1 |

**Key**
1 Clamping ring (optional)
2 Test specimen support

(a)

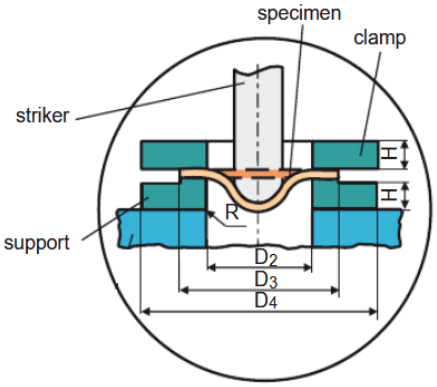


(b)

Figure 3.2: The recommended geometry for the clamping device (a) according to the standard [9] and (b) visualized by Grellmann, Seidler [20].

In ABAQUS, rigid parts need a Reference Point (RP) on which the loads are applied. The striker mass is modeled using the *Inertia* feature applied on the RP in ABAQUS. This feature assigns the total mass of the striker to the part. This is necessary due to the rigid definition of the striker and therefore not possible to achieve via a material definition including its density, as there is no material assigned to the rigid bodies.

### 3.1.2 Test specimen

Naturally, the most important component of the model is the test specimen. As shown in Figure 2.11 on page 14, the outer dimensions of the test specimen are $60$ x $60$ x $8\,\mathrm{mm}$. Furthermore, all corners are rounded with $r$ = $8\,\mathrm{mm}$. At the top and the bottom, there are *solid* (i.e. completely filled) layers which are $1\,\mathrm{mm}$ thick, while the inner structure with a height of $6\,\mathrm{mm}$ can be freely designed with some modelling related limits. As

Table 3.1: Parameters in the model regarding the different components of the experimental setup.

| Parameter | Suggested value according to the standard | Value used in the model |
|---|---|---|
| *Supporting and clamping ring* | | |
| Inner diameter | 40 mm | 40 mm |
| Outer diameter | $\geq$ 90 mm | 90 mm |
| Height | 12 mm | 12 mm |
| Striker diameter | 20 mm | 20 mm |
| Clamping force | 3 kN | 3.7 kN |
| Impact mass | – | 59.48 kg |

the model has to be meshable using the same element size while keeping the simulation time within an acceptable range, there are some restrictions in terms of geometry. These restrictions are discussed in more detail later. After all limiting factors have been described, the restrictions are easier to understand.

To correctly align all components, the thickness direction of the test specimen is defined as the z-axis when designed in an external CAD Program (e.g. CATIA, AutoCAD, SolidWorks). In the script, the options for the geometry file's format to import into ABAQUS are *.stp*, *.igs* and *.catpart*. Additionally, the completely filled test specimen is computed automatically in ABAQUS. The *solid* plate test specimen is shown in Figure 3.3.

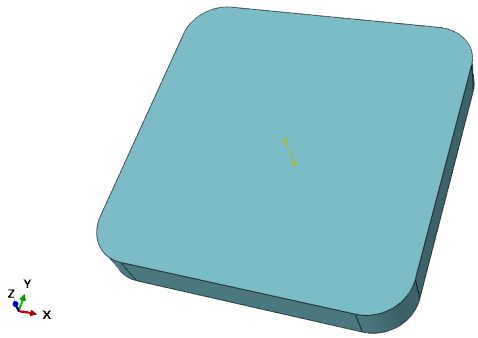


Figure 3.3: Visualization of the *solid* test specimen with the rounded edges.

## 3.2 Model setup

In this section, the alignment of all parts is described as well as the boundary conditions. As the impact test scenario is a dynamic load, an explicit model is built up. Also, the contact definitions in ABAQUS with all used properties are explained.

### 3.2.1 Geometrical setup

As mentioned before, the normal direction of the test specimen is defined as the z-axis. The parts are aligned in a way so that the striker moves in negative z-direction during the test. The initial distances between all parts are set in the Excel Sheet. The assembly is shown in Figure 3.4. For better visualization, the distances between the parts are increased. The variable $s1$ describes the initial distance of the lower tip of the striker to the upper surface of the test specimen, $s2$ is the initial gap between the clamping ring to the test specimen and $s3$ is the initial space between the lower surface of the test specimen and the supporting ring. The distances used in the model are listed in Table 3.2.

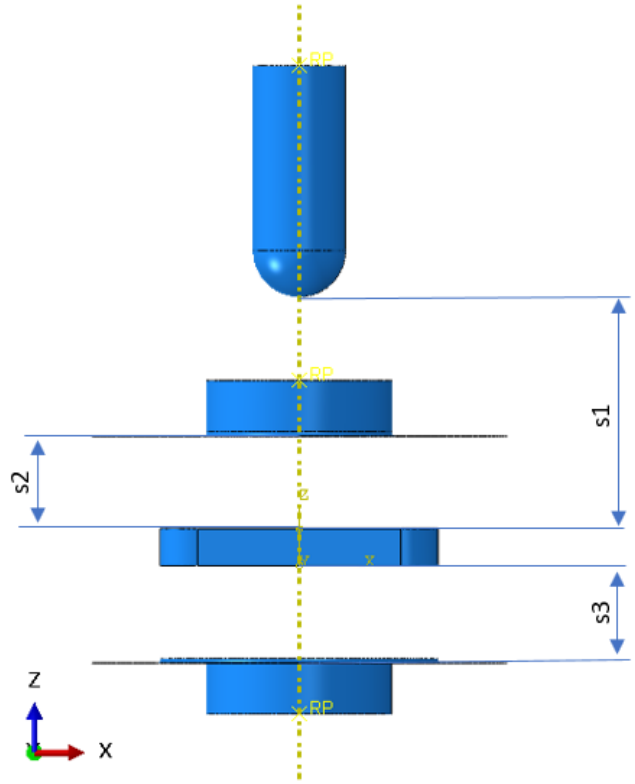


Figure 3.4: The assembly of all necessary parts with the initial distances $s1$, $s2$ and $s3$ between the parts.

| Variable | Distance |
|---|---|
| $s1$ | $0.1\,\mathrm{mm}$ |
| $s2$ | $0.001\,\mathrm{mm}$ |
| $s3$ | $0.001\,\mathrm{mm}$ |

Table 3.2: Values for the distances between the striker, clamping ring and supporting ring to the test specimen in the model.

### 3.2.2 Contact modelling

For the contact between all parts, two interaction properties and general contact are defined. One interaction property represents the contact between the specimen and the two rings. The other one defines the contact between the striker and the specimen. The general contact property describes the self-contact for the test specimen.

For the contact between the rings and the test specimen, the properties read as follows: The tangential behaviour is modelled with the penalty method having a variable coefficient of friction with a default value of $\mu = 0.3$. The normal behaviour uses the *hard contact* formulation of ABAQUS and allows a separation after contact. The contact formulation is *surface to surface*. The normal behaviour is the same for the interaction between the striker and the specimen. Contrary to the tangential behaviour of the first interaction property, the contact between the striker and the test specimen is considered frictionless (i.e. $\mu = 0.0$) as the striker is lubricated according to *ÖNORM EN ISO 6603:2* . The contact formulation is *surface to node* which means the surface of the striker can have contact with all of the nodes in the specimen.

Besides the contact definitions between the components in the model, there is also general contact defined. The general contact definition ensures that knocked-out structures of the specimen can still come into contact with the other components or the rest of the specimen. Without general contact, such structures would just move through other components without getting into contact. The interaction property for the general contact is modelled with the penalty formulation for tangential behaviour. Concerning normal behaviour, the *hard contact* formulation is implemented allowing a separation after contact. The variation of the coefficient of friction for the general contact (default: $\mu_{\mathrm{gen.}} = 0.5$) is investigated as for the coefficient of friction between the rings and the specimen.

### 3.2.3 Boundary conditions

As described in Section 3.1.1, the boundary conditions are applied on the clamping and supporting ring. To do so, a reference point for every component has to be specified – as they are discrete rigid bodies – and then selected as the region for the boundary condition to apply them on the whole body. For the supporting ring, all degrees of freedom are constrained. Therefore, this part does neither translate nor rotate. For the clamping ring, the boundary condition is similar with the exception that the clamping ring is allowed to move along the z-axis. The clamping force of $3.7\,\mathrm{kN}$ is applied in negative z-direction onto the clamping ring, while the ring may still be moved upwards by the test specimen. The choice that the clamping ring is able to moves in z-direction despite the clamping force is based on the experimental observations. The clamping force is applied in an individual step before the striker's initial velocity is applied. Using the clamping force as a boundary condition leads to dynamic phenomenons in the way that the motion of the clamping ring starts to oscillate. After observing the influence of the oscillation on the simulation results its effect is considered irrelevant making this boundary condition a legit decision.

Regarding the striker, the same constraints of DOFs (degrees of freedom) as for the clamping ring are made at the corresponding reference point. The initial velocity of the striker is set to $1\,\mathrm{m/s}$ as a *predefined field* to be along the negative z-axis without displacements in the other directions or any rotations possible. In Table 3.3, all boundary conditions are summed up for a better overview.

Table 3.3: List of all boundary conditions applied in the model.

| Component | Description |
|---|---|
| Supporting ring | All DOFs constrained |
| Clamping ring | only motion in z-direction is possible<br>vertical clamping force: $3.7\,\mathrm{kN}$ |
| Striker | only motion in z-direction is possible<br>vertical initial velocity: - $1\,\mathrm{m/s}$ |

### 3.2.4 Factors in the model influencing computation time

In this section, the important parameters which affect computation time are described. Furthermore, their implementation in the model in order to guarantee accurate results within an acceptable range of computation time is explained. The timespan of the model is chosen to capture full puncture. Therefore, the existing force-displacement curves of Petersmann et al. [8] are used as a basis for the step-time.

#### 3.2.4.1 Mesh

Using the explicit solver, the mesh affects computation time in two ways. The first one, as in every simulation, is the fact that using smaller and therefore more elements increases the time needed to compute the results. Additionally, the stable time increment addressed in the previous section is highly influenced by the element size of the mesh. As a result, the goal is to find an element size to be small enough to give accurate results while being not too small as this would raise computation time without affecting the results in a noticeable scale. On the other hand, the element size must be small enough that the geometry of the part – also new infill geometries that are constructed – can be represented without generating highly distorted elements.

For the explicit solver, there are only elements with linear shape functions available in ABAQUS. This means that a single element cannot represent bending. Therefore, it is essential that every feature in the geometry (e.g. thin ribs) is meshed with at least two elements over its thickness. Otherwise, the computed results would be inaccurate and meaningless.

Another factor to be thought of when choosing the element size is the material model or more specifically the damage, respectively failure model. As in this thesis the brittle failure model of ABAQUS is used, the results are also affected by the shape of the elements which again makes a mesh with high quality elements inevitable.

Considering all these parameters, an element size of $0.5\,\mathrm{mm}$ is chosen after some trial simulations. Remembering the dimensions of the test specimen being $60$ x $60$ x $8\,\mathrm{mm}$, the model would consist of $120$ x $120$ x $16$ elements which is $230\,400$ elements for the solid plate without round edges. As the element quality is especially important in the region where the striker hits the test specimen, the component is partitioned. This ensures the center of the body to be modelled using approximately cubic-shaped elements solely (Figure 3.5a). In Figure 3.5b and 3.5c, the meshed part is visualized to show the shape of the elements in different regions of the test specimen's geometry. Due to the rounded edges, there are slightly fewer elements in the model than in the rough estimate with a total of $227\,792$ elements.

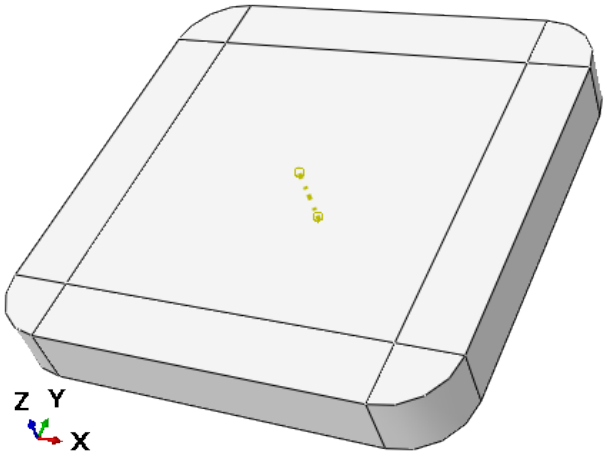


(a) Geometrical sectioning of the part to ensure a high quality mesh.

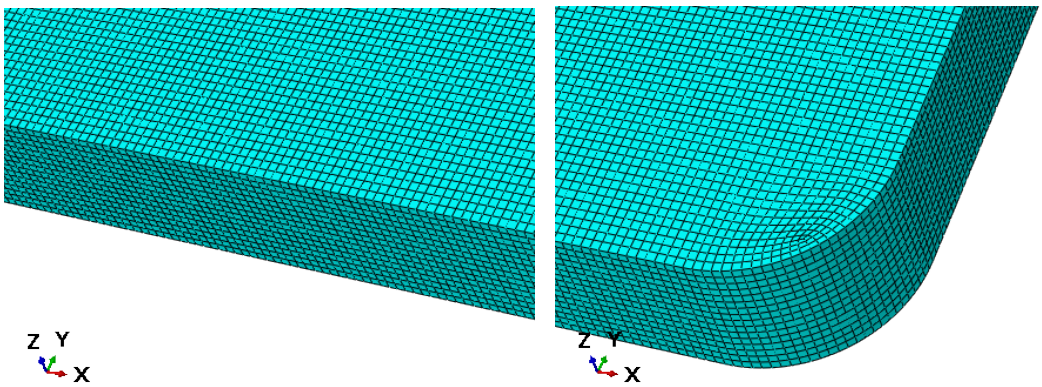


(b) The elements show a nearly perfect cubic shape for nearly the whole test specimen.

(c) View of few smaller and distorted elements to represent the rounded edges.

Figure 3.5: Geometrical partitioning and visualization of FE mesh

#### 3.2.4.2 Mass scaling

For keeping the computation time low, the technique of mass scaling is used in the model. As the stable time increment for explicit computations is proportional to the time an elastic wave needs to pass through an element, the element size, the element's

Young's modulus, and density of the material are the decisive values. The wave speed $v_\mathrm{s}$ through an isotropic, elastic material is defined by its Young's modulus $E$, density $\rho$ and a factor $K$ which varies for continuum, shell or beam elements and includes the material's Poisson's ratio $\nu$. The mathematical correlation according to Stommel et al. [29] is given in equation 3.1 with the factor $K$ for continuum elements being described in equation 3.2.

$$v_\mathrm{s} = K \cdot \sqrt{\frac{E}{\rho}} \tag{3.1}$$

$$K = \sqrt{\frac{1-\nu}{(1+\nu)(1-2\nu)}} \tag{3.2}$$

The stable time increment $t_\mathrm{stable}$ is the time a wave needs to travel the distance of the smallest element edge $l_\mathrm{crit,el}$. The stable time increment $t_\mathrm{stable}$ thus calculates as:

$$t_\mathrm{stable} = \frac{l_\mathrm{crit,el}}{v_\mathrm{s}} \tag{3.3}$$

As a consequence, the smallest stable time increment over all elements defines the stable time increment for the whole model. Considering equation 3.1, the wave speed $v_\mathrm{s}$ can be reduced by increasing the material's density $\rho$. A lower wave speed, on the other hand, increases the stable time increment $t_\mathrm{stable}$ according to equation 3.3. This is the definition of mass scaling. Mass scaling raises the density of elements with small necessary time increments resulting in a lower wave speed (equation 3.1) and therefore increases the stable time increment. Due to the fact that the geometry of the part is partitioned in a way to ensure nearly perfect cube-elements in the area of interest, this raised density is only applied on elements which are in regions not that important for the model and simulation results (i.e. the rounded corners of the specimen). The value for the increment time every element should have is chosen as the stable time increment for a perfect cube with the edge length of the desired element size, which is $0.5\,\mathrm{mm}$ for all simulations in this thesis. For the values of $E$ used, which are $2500$ and $5000\,\mathrm{MPa}$, the stable time increment is $3.41 \cdot 10^{-7}\,\mathrm{s}$ and $2.30 \cdot 10^{-7}\,\mathrm{s}$, respectively.

This process is only permitted if the mass of the whole system is not changed too much, as this would alter the results. For the *solid* test specimen, the mass of the whole model was only raised by $0.12\,\%$ and this only concerns elements far away from the impact region. However, this small difference raised the stable time increment by a factor of $4$. As a consequence, the computation time is reduced by $75\,\%$ with this minor intervention.

## 3.3 Material

### 3.3.1 Elastic model for 3D-printed PMMA

For extrusion and injection molding grades of PMMA, the mechanical properties are well documented. However, there are nearly no data sheets of 3D-printable grades available. The chosen material model is based on the impact behaviour of the 3D-printed test specimens shown in Section 2.2.5. The material is modelled as isotropic and linear-elastic. Linear-elasticity has to be assumed for the use of the brittle damage model in ABAQUS. For the ductile damage model, an elastoplastic material law is implemented. The assumption of an isotropic elasticity is not really representing the effects of the 3D-printing process, though. Due to the 3D-printing process, there are weld-lines between the extruded strands of material. As a result, this manufacturing method leads to anisotropic material behaviour. The reason for choosing an isotropic material law despite that circumstance is that due to the lacking data on mechanical properties for the processed PMMA grade, all material parameters have to be calibrated. Therefore, the isotropic material law keeps the material model simple with only few parameters calibrated with experimental results. As the explicit computation also needs a density of the material (Equation 3.1), the material model is limited to the parameters Young's modulus $E$, Poisson's ratio $\nu$ and the material's mass density $\rho$.

### 3.3.2 Damage model

The damage model of the material highly affects the results of the FE simulation. As a consequence of the failure patterns shown in Figure 2.12 on page 15, a brittle failure model for the material is chosen. In ABAQUS, this model is called *Brittle Cracking* and in the documentation it is referred to as *Cracking model for concrete*. The parameters needed for the post-cracking model are the tensile strength $\sigma_{\mathrm{t}}$ at which the damage of the material begins and then values for stress-strain pairs $\sigma_{\mathrm{True}}$, $\varepsilon_{\mathrm{True}}$ of the material after first cracking.

There are two approaches to provide the necessary post-cracking parameters. Providing the post-cracking stresses and strains in a tabular form, the post-cracking stress-strain behaviour of the material is defined in a piecewise linear function between the given data pairs, see Figure 3.6.

The second approach for defining the failure behaviour of the material is limited to a single linear section. For that approach, the tensile-strength $\sigma_{\mathrm{t}}$ is needed as well as the fracture energy $G_{\mathrm{F}}$. In this case, the post-cracking stress-strain curve is described as a stress-displacement curve. With the area below the linear function $\sigma(u)$ being equivalent to the given $G_{\mathrm{F}}$, the displacement $u_{\mathrm{fail}}$ ($\sigma$ = 0) can be computed using equation 3.4. As $G_{\mathrm{F}}$ is the area under the post-cracking stress-strain curve leaving out the linear-elastic pre-cracking curve, $G_{\mathrm{F}}$ is not the material parameter of fracture energy $G_{\mathrm{IC}}$ In Figure 3.7, the linear function computed by ABAQUS with given $\sigma_{\mathrm{t}}$ and $G_{\mathrm{F}}$ is visualized.

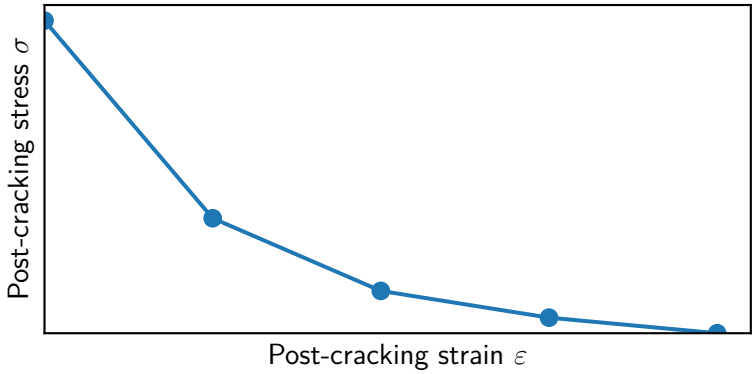


Figure 3.6: The brittle post-cracking material model according to the ABAQUS Documentation.

$$u_{\text{fail}} = \frac{2G_{\text{F}}}{\sigma_{\text{t}}} \tag{3.4}$$

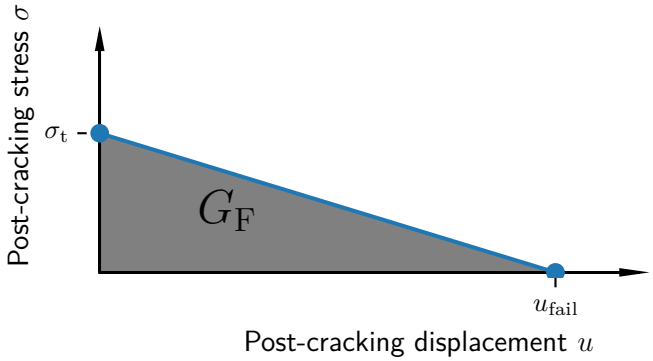


Figure 3.7: The brittle post-cracking material model when using fracture energy $G_{\text{F}}$ as a parameter – as found in the ABAQUS Documentation.

Using equation 3.4, the two approaches can be transformed into one another considering the element size $elsize$ with $u/elsize$ being equal to the technical strain of the element $\varepsilon_{\text{tech.,fail}}$. The element size is needed in this relation, because – as mentioned before – the approach using the fracture energy computes a failure displacement and not a failure strain. Therefore, the edge length of an element influences the strain at which the element fails and thus the energy absorption. This is visualized in Figure 3.8. Furthermore, the geometry of the elements affects the results in terms of energy absorption. To investigate the effects of different meshes, simple models are built up and the results are discussed in the next chapter.

$$\varepsilon_{\text{True,fail}} = ln\left(1 + \frac{u_{\text{fail}}}{elsize}\right) \tag{3.5}$$

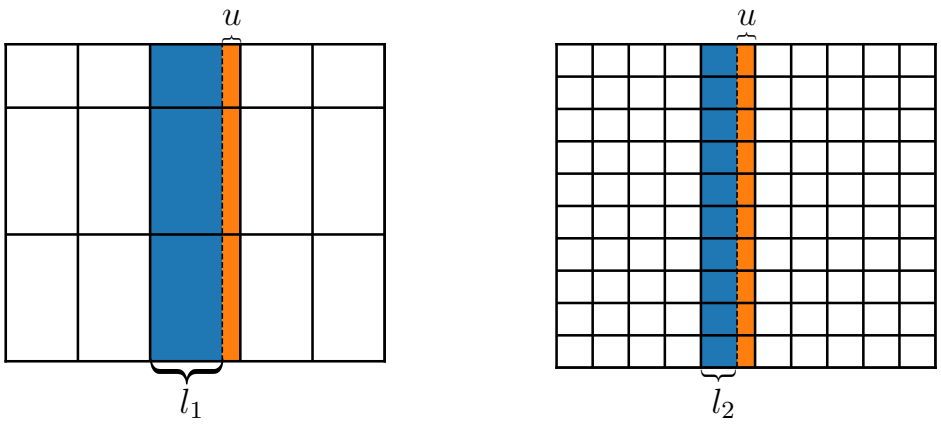


(a) Visualization of a rough mesh with $elsize\, l_1$

(b) Visualization of a finer mesh with $elsize\, l_2$

Figure 3.8: Comparison of different meshes where different strains $\varepsilon$ in the elements occur for the same displacement $u$ (orange).

$$\varepsilon_{\text{True,fail}} = ln\left(1 + \frac{2 \cdot G_{\text{F}}}{\sigma_{\text{t}} \cdot elsize}\right) \tag{3.6}$$

Summed up, both approaches can be transformed into one another resulting in the exact same post-cracking stress-strain curve. In Table 3.4, the converted list of stress-strain values for a given $G_{\text{F}}$, considering equation 3.6, is shown.

Table 3.4: Transformed values for post-cracking stress-strain approach for a given $G_{\text{F}}$.

| post-cracking stress $\sigma$ | post-cracking strain $\varepsilon$ |
|---|---|
| $\sigma_{\text{t}}$ | $0$ |
| $0$ | $\varepsilon_{\text{True,fail}}$ |

Besides dealing with the tensile failure behaviour, the shear behaviour has to be defined in the brittle cracking material model. While crack initiation is based on Mode I loading, post-cracking behaviour includes Mode II crack opening as well as Mode I. The shear retention model in ABAQUS describes the post-cracking shear stiffness as a function of crack opening strain. The shear-retention-factor $\rho$ is considered relative (i.e. in a range from $0$ to $1$) to the uncracked shear modulus. The test procedure for such experimental data is difficult, leading to initial assumptions how the shear-retention-factor function might look like. In this case, the ABAQUS documentation suggests the same curve as for the stress after first crack as seen in the previous Figures. As the shear-retention-factor has to be provided in the tabular form of $\rho$ and $\varepsilon$, the described transformation from fracture energy to stress-strain data is necessary even when using fracture energy as a parameter for the tensile post-cracking behaviour. As the user input for the model is the fracture energy $G_{\text{F}}$, the stress-strain data is determined and given

to ABAQUS by the Python script. As an initial guess, the table for the shear-retention-factor is nearly the same as for the post-cracking stress-strain table, as seen in Table 3.5. This table can also be changed in the Excel-Sheet independent from the tensile-failure behaviour. Using the keyword *default* instead of entering data pairs, the failure-strain $\varepsilon_{\mathrm{True,fail}}$ is taken from the table of the tensile-failure data. In Figure 3.9, the curve for the suggested initial guess of the retention factor is schematically shown.

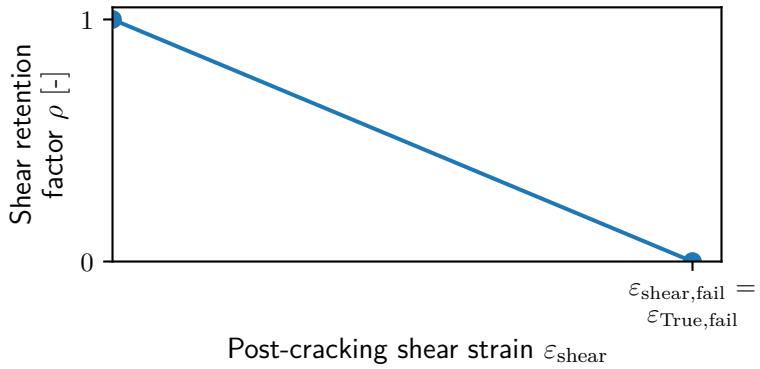


Figure 3.9: Visualization of the initial assumption for the post-cracking shear behaviour and the parameters $\rho$ and $\varepsilon_{\mathrm{shear}}$

Table 3.5: Initial assumption of the shear failure behaviour of the 3D-printed PMMA material.

| shear-retention-factor $\rho$ | post-cracking strain $\varepsilon$ |
|---|---|
| 1 | 0 |
| 0 | $\varepsilon_{\mathrm{True,fail}}$ |

An optional parameter for the brittle failure model in ABAQUS is the element deletion strain respectively element deletion displacement. Dependent on the approach chosen for the tensile failure behaviour, the software interprets this value either as a strain or displacement. This parameter is important for the simulation as elements which exceed this value are deleted and no longer part of the model, once this situation occurs. As the stiffness of the damaged material rapidly reaches zero, the elements have to be deleted at the right time in order to prevent the simulation from aborting due to excessive distortion appearing in the concerned elements. However, if the element deletion strain is not the same as the failure strain element deletion leads to the build up of spurious force and energy. In Figure 3.10, the difference between the failure strain $\varepsilon_{\mathrm{fail}}$ and the element deletion strain $\varepsilon_{\mathrm{del}}$ is shown. The failure strain is the strain at which $\sigma = 0$ in the post-cracking stress-strain curve. The strain at which an element is deleted can be lower or higher than $\varepsilon_{\mathrm{fail}}$.

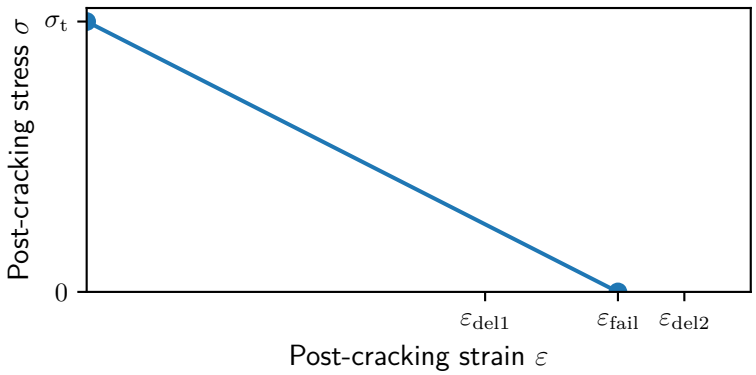


Figure 3.10: Example for different values of $\varepsilon_{\mathrm{del}}$ showing that the element deletion strain can be chosen independently from the failure strain $\varepsilon_{\mathrm{fail}}$.

## 3.4 Restrictions due to the model build-up

In the previous sections it was briefly addressed that for ensuring low computation-times there are certain restrictions for designing new infill geometries of the test specimen. Remembering the goal of this thesis – finding inner structures for the 3D-printed test specimen which absorb high amounts of energy during the test – the designing of new geometries is an essential part in this thesis besides the model build-up and simulation workflow. Keeping the computation time in an acceptable range is of high importance. As a consequence, the mesh limits the freedom of the designing process tremendously. The chosen element size and type, which are described in more detail in Section 3.2.4.1, cause a big restriction for the designing process. The consequence of an element size of $0.5\,\mathrm{mm}$ limits the thickness of every feature in the geometry to a minimum of $1\,\mathrm{mm}$. Therefore, the geometrical possibilities using a 3D-printing manufacturing do not limit the geometry because the reason of all geometrical limitations is computation time. The printer would be able to print features only $0.5\,\mathrm{mm}$ of width in-plane and could print layers which are only $0.25\,\mathrm{mm}$ thick.
The listed restrictions cause the designing process to be rather fundamental. This results in comparing the predictions of geometries with different features used as infill structures more than designing very fine structures which might be more suitable to fulfill the energy absorption target which was the actual goal of the thesis in the first place.

To provide a clean mesh in the area of impact for all designs of test specimen, the geometry is additionally partitioned so that every layer of $1\,\mathrm{mm}$ in thickness is a separate cell. As a consequence, a perfect mesh in the center of the test specimen is ensured. These layer partitions created for meshing the imported designs are visible in Figure 3.11.

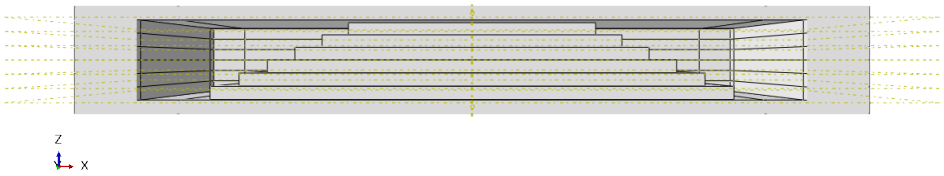


Figure 3.11: Visualization of the partitions created for test specimens with an infill geometry different from the solid plate.

## 3.5 Evaluation of simulation data

The result gained from the experiment is a force-displacement curve of the striker tip. From this curve the absorbed energy can be computed. To compare the simulation results to the experimental setup, the desired output is the reaction force and displacement of the striker. After the simulation, the force-displacement curve is compared to the test results. Therefore, the output parameters in ABAQUS are the total contact force between the striker and test specimen in z-direction and the displacement of the striker along the z-axis.

Another part of the evaluation of simulation results is the process of representing the actual material behaviour using the FE model. Finding the best parameters for a material model is achieved via manual iteration. After every iteration, the force-displacement curve is compared against the test curves. Furthermore, the absolute values for the absorbed energy of both, the simulation and the experiment, are compared. At the first stage, after every simulation only one parameter is varied significantly in order to understand the influence of the parameters on the force-displacement curve. After that, several parameters are changed at once but to a lesser extent to calibrate the material model.

Remembering the restrictions of the model – described in Section 3.4 – only the completely filled test specimen of the publication by Petersmann et al. [8] can be simulated, as all default patterns provided by the slicing software contain too small features to mesh properly. Firstly, the failure model parameters are calibrated to reproduce the impact behaviour of the "solid" test specimens. After getting an acceptable accuracy for the simulation compared to the experiments, another infill geometry is designed and its impact behaviour predicted via FE-simulation. Then, the material model can be either used for further geometries or adapted to the infill-geometry and again be tested for its prediction accuracy. In Table 3.6, all parameters concerning the impact behaviour of the test specimen set in the Excel sheet for the model build-up are listed.

Table 3.6: Overview of all relevant model parameters with the default values used for following observations. All parameters can be changed in order to fit the simulation results to the experimental test data.

| Parameter | Default value used for following observations |
|---|---|
| Young's modulus $E$ | $5500\,\mathrm{MPa}$ |
| Poisson's ratio $\nu$ | $0.33$ |
| Tensile Strength $\sigma_\mathrm{t}$ | $100\,\mathrm{MPa}$ |
| Fracture Energy $G_\mathrm{F}$ | $0.2\,{}^{\mathrm{J}}/_{\mathrm{mm}^2}$ |
| Shear-failure-strain $\varepsilon_{\mathrm{shear,fail}}$ | $0.005$ |
| Element deletion strain $\varepsilon_\mathrm{del}$ | $0.005$ |
| Coefficient of friction (clamping and supporting ring – test specimen) $\mu$ | $0.3$ |
| Coefficient of friction (general contact) $\mu_\mathrm{gen}$ | $0.5$ |

# 4 Results and Discussion

## 4.1 Implementation of the brittle damage model in ABAQUS

### 4.1.1 Damage model parameters

Implementing a single-element-test, the damage model parameters and their effects are observed. In this model, an understanding for the model is acquired in order to use this damage model for the more comprehensive model of the impact test. The element in the model is a cube with an edge length of $1\,\mathrm{mm}$. Therefore, the values of force and displacement are equivalent to the values of stress and strain.

Starting with a uniaxial tensile test, the parameters influencing the material behaviour are the Young's modulus $E$, tensile strength $\sigma_\mathrm{t}$ and the fracture energy $G_\mathrm{F}$ which determine the post-cracking failure strain $\varepsilon_\mathrm{fail}$. The parameters of the brittle damage model do not have to represent the PMMA material, because these runs should give a qualitative effect of the parameters(Table 4.1).

Table 4.1: The parameters in the single-element-test.

| Parameter | Value |
|---|---|
| Young's modulus $E$ | $5500\,\mathrm{MPa}$ |
| Tensile strength $\sigma_\mathrm{t}$ | $50\,\mathrm{MPa}$ |
| Fracture energy $G_\mathrm{F}$ | $10\,{}^{\mathrm{J}}/_{\mathrm{mm}^2}$ |
| Element deletion strain $\varepsilon_\mathrm{del}$ | $0.2$ |

Investigating the tensile behaviour, at first a strain which leads to complete failure of the material is applied. For the second test, the failure criterion for element deletion $\varepsilon_\mathrm{del}$ is used in the model. As expected, the reaction force drops to zero when reaching $\varepsilon_{del}$. As a consequence, the dissipated energy which is the area below the stress-strain (or force-displacement) curve is reduced due to deleting the element before it has released the given fracture energy (Figure 4.1).

For the next test, a strain which leads to a partly damaged element is applied. Then the strain is released and applied again to see the difference in strain for the undamaged first loading and the damaged second loading. In Figure 4.2, the effect of material damage can be seen in the flatter slope in the stress-strain curve for the second loading (orange curve).

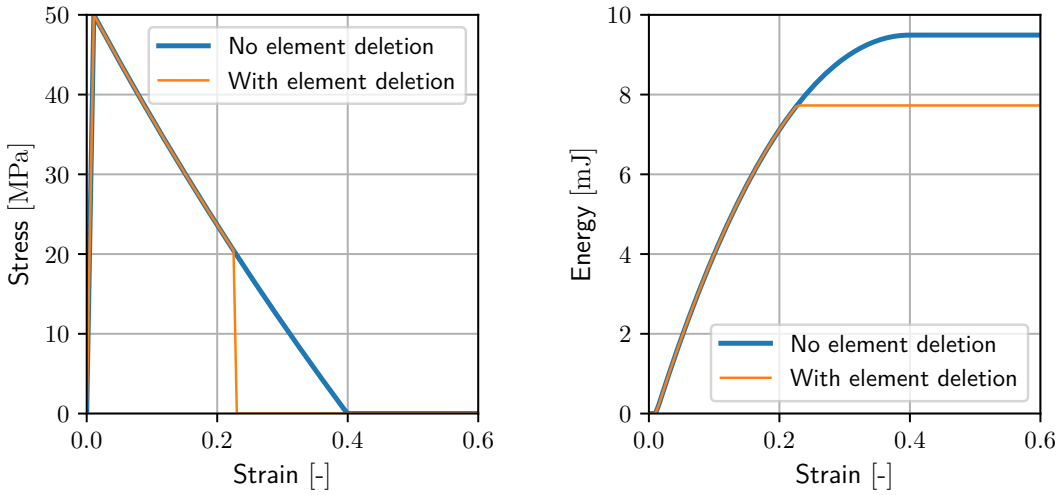


(a) Stress-strain curves with and without failure criterion.

(b) Energy-strain curves with and without failure criterion.

Figure 4.1: The stress-strain and energy-strain curves for a single-element tensile-test.

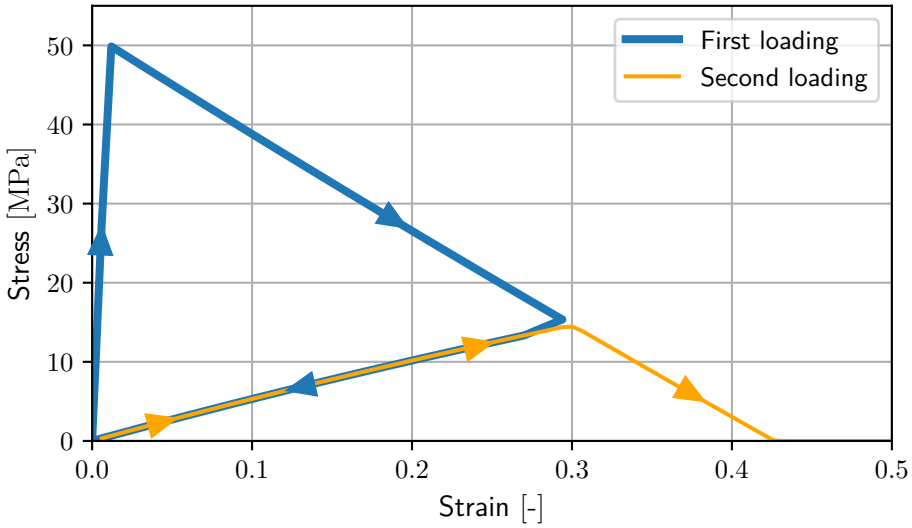


Figure 4.2: The stress-strain curve for two cycles of loading where the first loading damages the material.

Following the tensile test, the next tests performed are pre-damaged shear tests. In Figure 4.3a, the tensile pre-loading before applying the shear strain for 3 different states is shown. For the case *no damage*, no tensile loading is applied. The state *damage* means that a tensile strain of $0.2$ is applied, reducing the tensile stiffness to approximately $50\,\%$ of the undamaged tensile stiffness. The *completely damaged* state means that the tensile stiffness of the material is $0$ before the shear loading is applied. These pre-damaged material states are then loaded with a shear strain. In Figure 4.3b, the effect of pre-damage is visible. While both states of pre-damage decrease the shear stiffness, the amount of damage does not have an effect on the shear stiffness. An explanation is that the mode II crack opening strain is the same for both pre-damaged loading scenarios but this would not work for a completely damaged element.

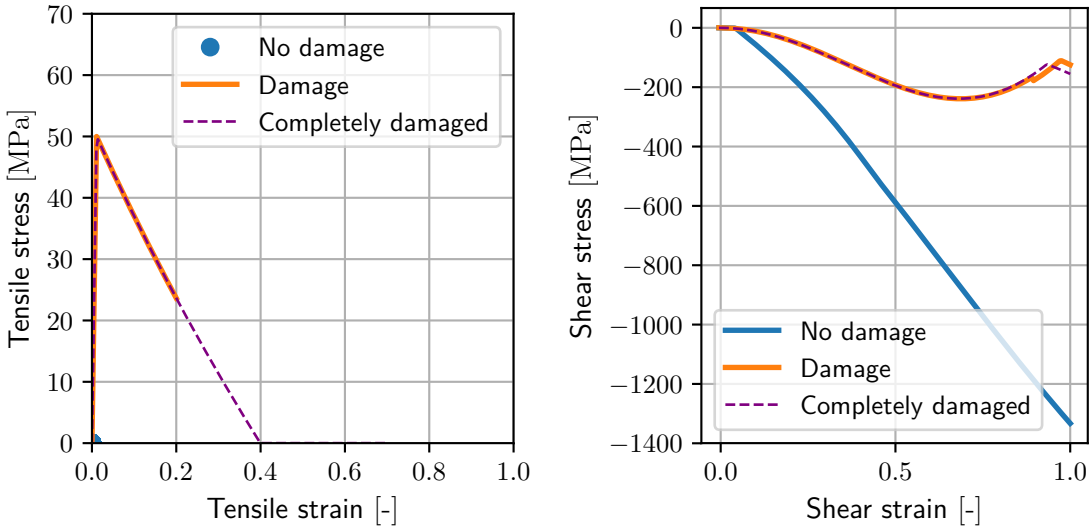


(a) The tensile pre-loading scenarios applied before the shear loading.

(b) The stress-strain curve for shear loading of the 3 pre-damaged states of material.

Figure 4.3: Visualization of the effect of (a) tensile pre-damage on (b) the shear stiffness of a material in the brittle damage model.

As a further observation, the curve for the shear retention factor is varied using different values for $\varepsilon_{\text{shear,fail}}$, where the shear retention factor $\rho = 0$ (Figure 4.4a). The chosen values for $\varepsilon_{\text{shear,fail}}$ are listed in Table 4.2. Then the curve's influence on the shear stiffness is evaluated. The shear loading is applied for the pre-damaged state *damage* as shown in Figure 4.3a before. In Figure 4.4b, the stress-strain curves as a result of the various retention factor curves are shown. There is a local maximum (absolute value) during the shear test. However, the shear stress does not become zero afterwards but with increasing shear loading there is still an increasing stress carried by the element. An explanation is that shear is a combined loading of tensile and compressive loading. While the element does show no more tensile stiffness, the amount of compressive loading can still be absorbed by the element. This also explains that all curves show the same shear stress after the element fails.

Table 4.2: The parameters chosen for the 3 investigated curves for the shear retention factor $\rho$.

| Curve | $\varepsilon_{\text{shear,fail}}[-]$ |
|---|---|
| Retention curve 1 | 1 |
| Retention curve 2 | 0.1 |
| Retention curve 3 | 0.01 |

As final tests using only a single element, tensile and compression loading are applied. Again, the pre-damaged states shown in Figure 4.3a are used. In Figure 4.5, it is shown that the tensile pre-damage does not have an effect on the compressive stiffness. This confirms that also elements which do not show any tensile stiffness are still able to withstand compressive stress. This circumstance is also mentioned in the ABAQUS doc-

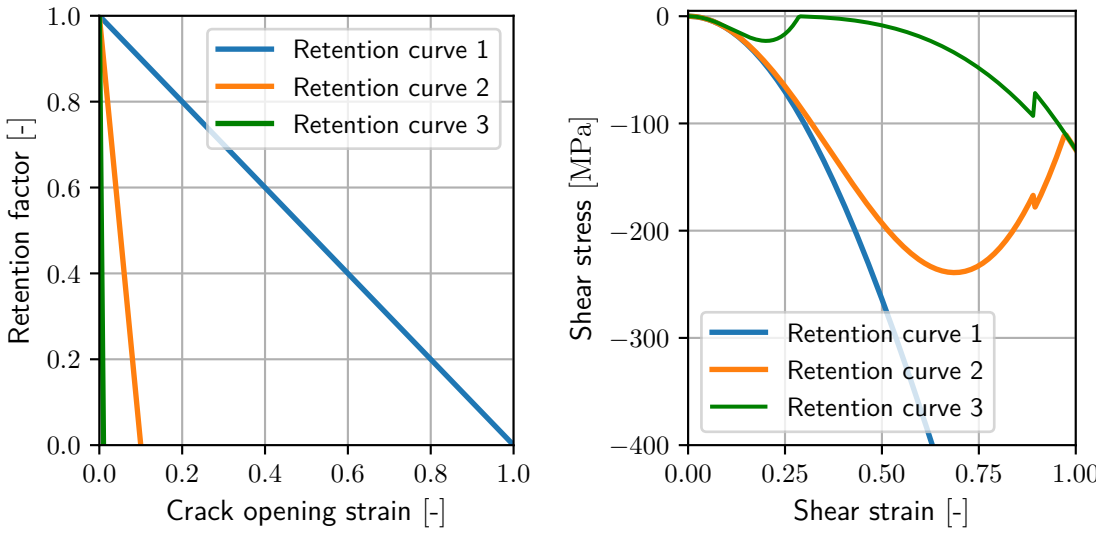


(a) Different curves for the retention factor to investigate their effect on the shear stiffness of a pre-damaged material element.

(b) The stress-time curve for the pre-damaged element under shear loading.

Figure 4.4: Visualization of the effect of (a) different curves for the retention factor on (b) the shear stiffness of a pre-damaged material in the brittle damage model.

umentation regarding element deletion. Element deletion ensures the computation to avoid excessive distorted elements in the model causing an abortion. Nevertheless, deleting the elements also decreases the reaction force if there is any compressive loading component acting on the element which it would be possible to withstand.

Another important aspect about the damage model is that the material law has to be isotropic and linear elastic. As a consequence of the developing cracks, the material behaviour becomes anisotropic. While the intact continuum between the cracks is modelled isotropic, the direction and length of the cracks lead to anisotropic properties for the damaged element.

### 4.1.2 Mesh dependency of the brittle damage model

In this section, the implementation of the brittle damage model in ABAQUS is investigated. Therefore, a simple model with different element shapes is built up. The load in this model is a static displacement using the implicit solver contrary to the model representing the impact test. This model gives an explanation on how the behaviour of the brittle material damage model in ABAQUS is dependent on the mesh.

Figure 4.6 shows the different meshes used at this stage of the thesis. The specimen is a cube with an edge length of $1\,\mathrm{mm}$. The loading scenario is a uniaxial displacement in x-direction. The magnitude of displacement is chosen in a way that the resulting strain exceeds the material limits and therefore ensures failure of some elements in

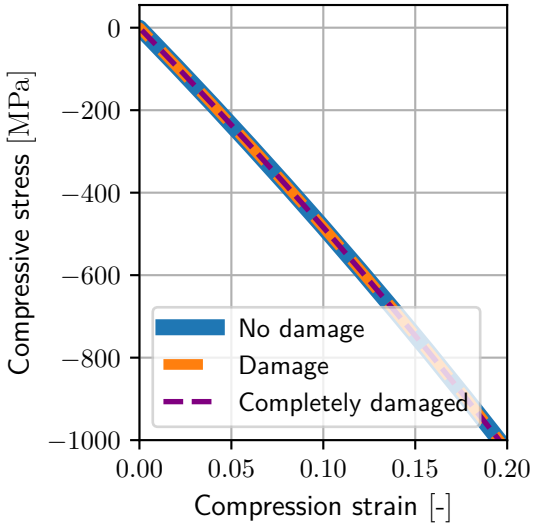


Figure 4.5: The stress-time curve for compressive loading dependent on preceding tensile loading.

the model. The parameters are the same as for the tests in Section 4.1.1 and listed in Table 4.3 for tensile damage and in Table 4.4 for post-cracking shear behaviour. All parameters remain unaltered for the investigation of different meshes.

Table 4.3: The parameters for the mesh study model for the tensile damage model.

| Parameter | Value |
|---|---|
| Tensile strength $\sigma_{\mathrm{t}}$ | $50\,\mathrm{MPa}$ |
| Fracture energy $G_{\mathrm{F}}$ | $10\,{}^{\mathrm{J}}/_{\mathrm{mm}^2}$ |

Table 4.4: The parameters for the mesh study model for the post-cracking shear behaviour.

| shear-retention-factor $\rho$ | post-cracking strain $\varepsilon$ |
|---|---|
| 1 | 0 |
| 0 | 0.001 |

As a result, the dissipated damage energy obtained from the computation varied extremely because of the different element shapes. Understanding the variations in dissipated damage energy, the implementation of the brittle damage model can be explained. As fracture energy is the energy per unit area which is dissipated if a crack propagates, the surface area created is a parameter needed for computing the dissipated damage energy. Without knowing the crack direction, the created surface area of a crack which propagates throughout an element is not known. Therefore, ABAQUS uses the element volume $V_{\mathrm{el}}$ and considers the shape being a cube. As a result, the element has a fictional cubic edge length $a_{\mathrm{cube}} = \sqrt[3]{V_{\mathrm{el}}}$. For failure, the damage model considers the area of a cube surface to be the area $A_{\mathrm{fail}} = a_{\mathrm{cube}}^2$ where the given value of fracture energy is completely released.

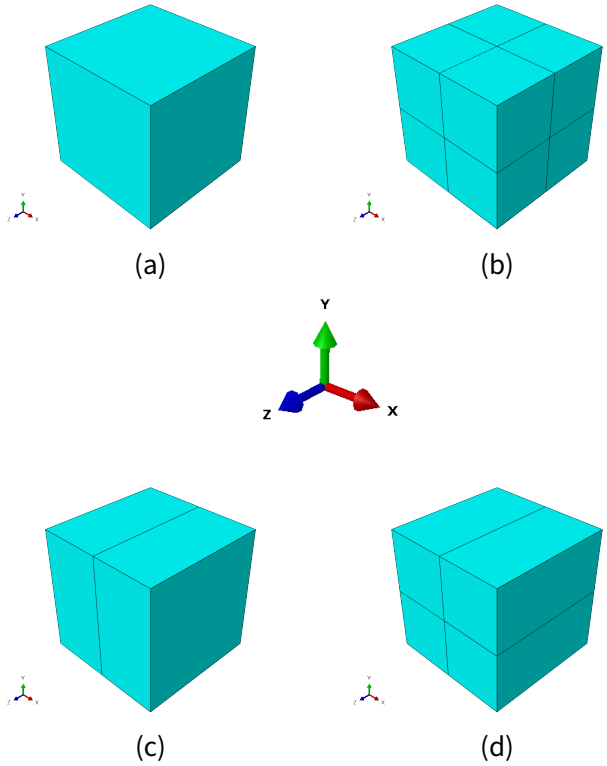


Figure 4.6: Visualization of the different meshes used. (a) 1 element, (b) 8 elements, (c) 4 elements, (d) 2 elements

Considering the loading case in these models, $A_{\text{fail}}$ is the cross-section of the specimen along the x-axis. In this case, it is a square with an edge length of $1\,\text{mm}$. As the damage model in ABAQUS is implemented as described above, mesh (a) of Figure 4.6 is used as the reference, because it is a single element which has the shape of a cube. Using this reference, the damage dissipation energy $D$ (computed from FEM) of the other meshes can be predicted considering the dimensions of the elements. Therefore, the relative dissipation energy $D_{\text{rel}}$ can be expressed using equation 4.1 where the reference dissipation energy is $D_{\text{ref}}$ of the cube-shaped element, $A_{\text{ref}}$ is the failure area of the reference mesh and $n$ is the number of elements which fail.

$$D_{\text{rel}} = D_{\text{ref}} \cdot \frac{A_{\text{fail}}}{A_{\text{ref}}} \cdot n \tag{4.1}$$

Using equation 4.1, the damage dissipation energy for the meshes b, c and d can be predicted very well as shown in Table 4.5.

As shown in Table 4.5, the dissipation energy varies extremely. This preparatory work is the reason for the mesh considerations mentioned in Chapter 3. As a consequence, with using nearly perfectly cubic-shaped elements in the region of interest, such errors

Table 4.5: Computation of the obtained damage dissipation energy from the results according to equation 4.1.

| Mesh | Element-size | Failing el. $n$ | $a_{\text{cube}}$ [mm] | $A_{\text{fail}}$ [mm$^2$] | $D_{\text{rel}}$ [J] | $D_{\text{def}}$ [J] |
|---|---|---|---|---|---|---|
| (a) | 1 x 1 x 1 mm | 1 | 1 | 1 | 10.47 | 10.47 |
| (b) | 0.5 x 0.5 x 0.5 mm | 4 | 0.50 | 0.25 | 10.47 | 10.86 |
| (c) | 0.5 x 1 x 1 mm | 1 | 0.79 | 0.63 | 6.60 | 6.67 |
| (d) | 0.5 x 0.5 x 1 mm | 2 | 0.63 | 0.40 | 8.38 | 8.51 |

in the resulting reaction force as well as dissipated energy can be avoided. In Figure 4.7, the force-displacement and energy-displacement curves for the different meshes are shown to visualize the effect of the mesh on the material damage model.

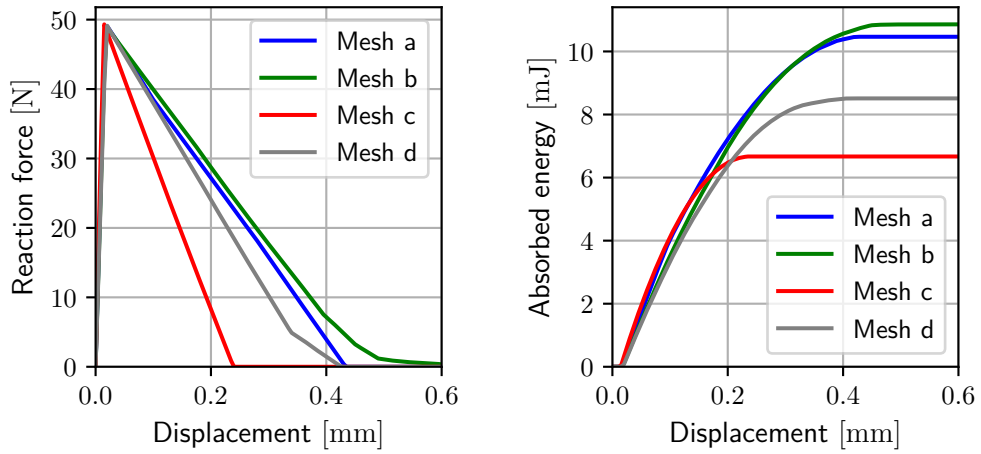


(a) Force-displacement curves for the different meshes

(b) Energy-displacement curves for the different meshes

Figure 4.7: Visualization of the effect of different meshes on the material damage model.

## 4.2 Experimental results for the solid specimens

In this section, the experimental results for the completely filled specimens are discussed. In Figure 4.8a, the force-displacement curves for the striker tip of the impact tests performed by Petersmann et al. [8] are shown. As the representative force-displacement curve, the curve of specimen 4 is chosen. Therefore, in the following, the force-displacement curve of specimen 4 is compared against the simulation results. This curve is the one to approximate using FE simulation as it is closest to the mean of all specimen.

Because the main goal in this thesis is to predict the energy absorption of different infill geometries, the energy dissipated by the specimens is shown in Figure 4.8b. As a result of the force-displacement curves, specimen 4 approximately represents the mean of

all specimens regarding energy absorption. In Table 4.6, the exact values for the dissipated energy of each specimen is shown to visualize that specimen 4 best represents the mean dissipated energy.

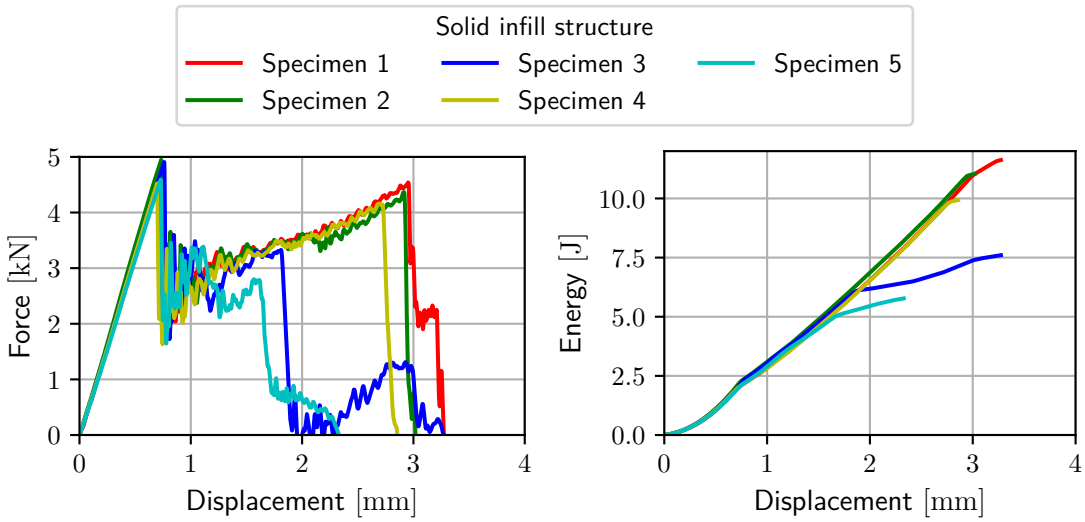


(a) (b)

Figure 4.8: The experimental data for the solid infill structure. (a) shows the force-displacement curves of the 5 specimens and (b) shows the amount of absorbed energy for each specimen.

Table 4.6: Comparison of the absorbed energy for all specimens.

| Specimen | Dissipated energy [J] |
|---|---|
| 1 | 11.62 |
| 2 | 11.04 |
| 3 | 7.60 |
| 4 | 9.93 |
| 5 | 5.77 |
| Mean | 9.19 |

## 4.3 Computed results for the solid specimen

In this section, the results of the FE-simulations are shown. Firstly, the results of a brittle material damage model implemented in ABAQUS are discussed, followed by the ductile damage model.

### 4.3.1 Brittle damage model

Using the brittle damage model, the abrupt failure of the solid specimens in the test can be reproduced via FE-simulation. However, there are many parameters in this damage

model which makes the calibration of the model complex and time-consuming. In the following sections, the influence of the material model parameters is shown. Following, the best approximation for the solid specimens is used to predict the impact behaviour for varying infill geometries.

In Figure 4.9, an example for a computed force-displacement curve is shown. Additionally, the deformation of the specimen is shown at certain displacements to visualize the stages of damage over the force-displacement curve.

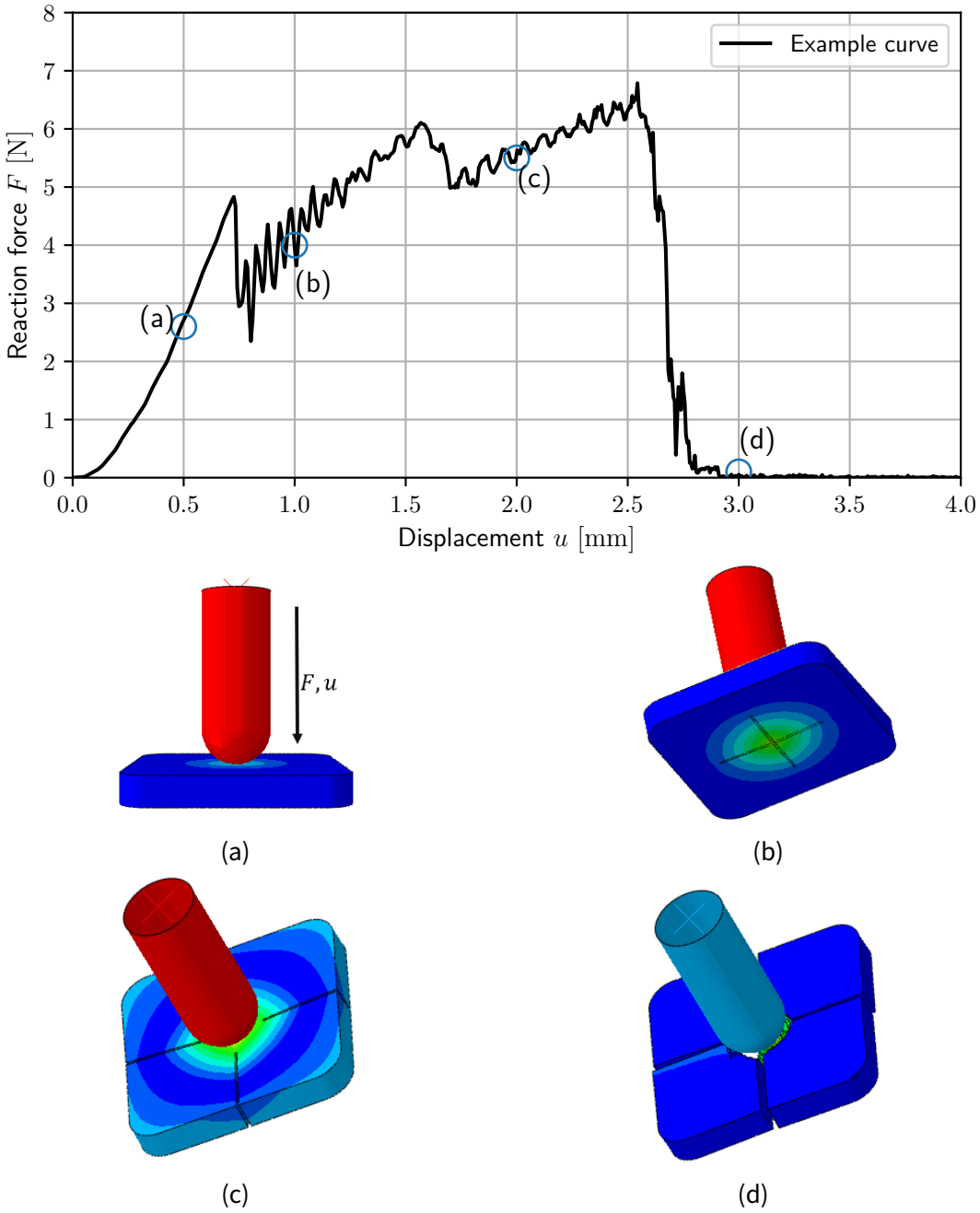


Figure 4.9: Example curve with the states of damage during the impact test.

### Elastic material model parameters

As described in Section 3.3.1 on page 25, the elastic material model for the 3D-printed PMMA is assumed to be isotropic and linear-elastic. Therefore, there are only 2 parameters in the elastic material model. These are the Young's modulus $E$ and the Poisson's ratio $\nu$. Figure 4.10 shows the influence of those parameters on the results. Therefore, reference values of $E$ = $5000\,\mathrm{MPa}$ and $\nu$ = $0.33$ are chosen and then the values for $E$, and $\nu$ are varied. This allows to understand what effect a variation of these parameters has on the results. This understanding is important to calibrate the simulation results to the test data.

The effect of the Young's modulus $E$ until reaching first damage is pretty simple. Up to that point, a higher Young's modulus increases the slope in the force-displacement curve. Furthermore, with increasing $E$, the reaction force after first damage increases. Another effect is that with increasing $E$, the abrupt failure is shifted to higher displacements. Assuming a high Young's modulus allows to fit the force-displacement curve until first damage very well. On the other hand, the high reaction forces after first damage overestimate the test results. Choosing the value for $E$ is therefore a compromise of approximating the behaviour at low displacements and approximating the force-displacement curve after first damage.

Contrary to the Young's modulus, the Poisson's ratio $\nu$ does not affect the magnitude of reaction force. However, the value for $\nu$ highly affects the displacement at which the specimen's abrupt failure occurs. Lower values for $\nu$ lead to a delayed failure compared to higher values for $\nu$.

### Brittle damage model parameters

As listed in Table 3.6 on page 31, there are 7 variable parameters in the test setup with brittle damage. First of all, the effect of the tensile strength $\sigma_{\mathrm{t}}$ is discussed. As seen in Figure 4.11, a higher tensile strength shifts both first damage and abrupt failure to higher displacements. Regarding reaction forces, there is a shifting of the first peak, but except the shifted first peak, the reaction forces are the same after first damage. For example, reaction force is the same for all values of $\sigma_{\mathrm{t}}$ in the range between first damage and abrupt failure (e.g. at a displacement of $1\,\mathrm{mm}$).

The other varied parameter shown in Figure 4.11 is the fracture energy $G_{\mathrm{F}}$. In the Figure, the increase from low $G_{\mathrm{F}}$ to mid $G_{\mathrm{F}}$ gives expected results. That the material with high $G_{\mathrm{F}}$ shows an earlier abrupt failure than the material with mid $G_{\mathrm{F}}$ is unexpected. Therefore, the results for the varied fracture energy are studied more in detail.

The effects of varying $G_{\mathrm{F}}$ from low to mid value can be explained looking at Figure 4.12. The material with lower $G_{\mathrm{F}}$ shows more progressed cracks before the second drop (at $2\,\mathrm{mm}$ displacement) in reaction force (Figures 4.12a, 4.12b). From that point on, the

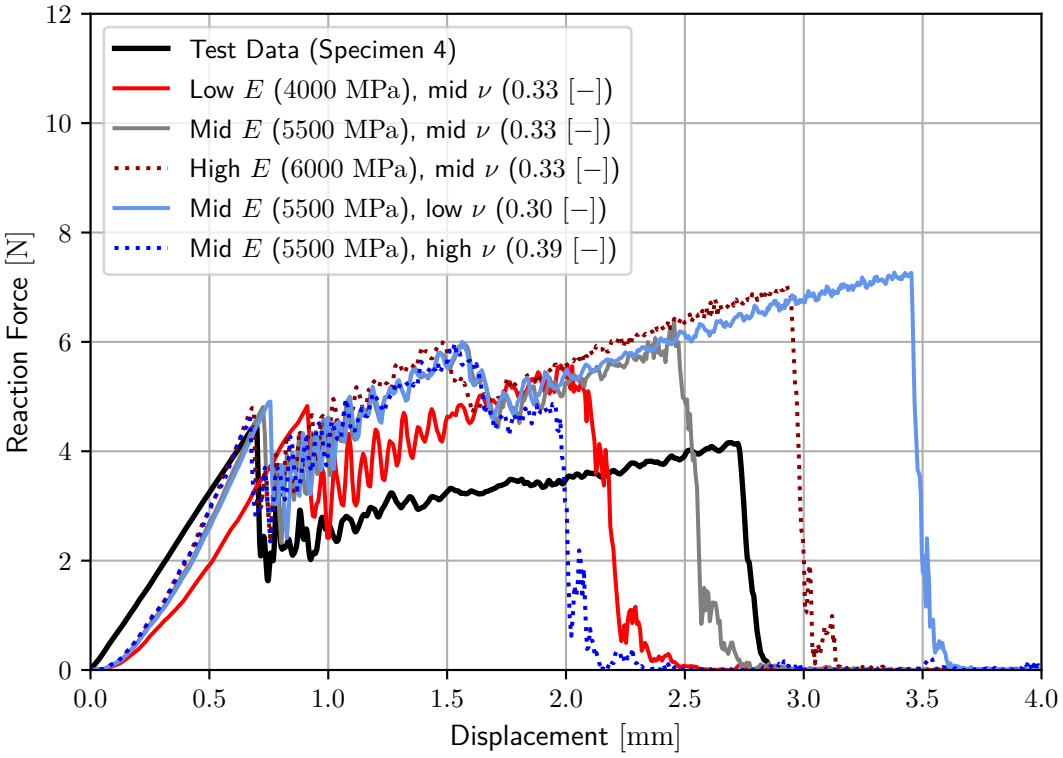


Figure 4.10: Comparison of different values for $E$ and $\nu$ to visualize the effects on the results.

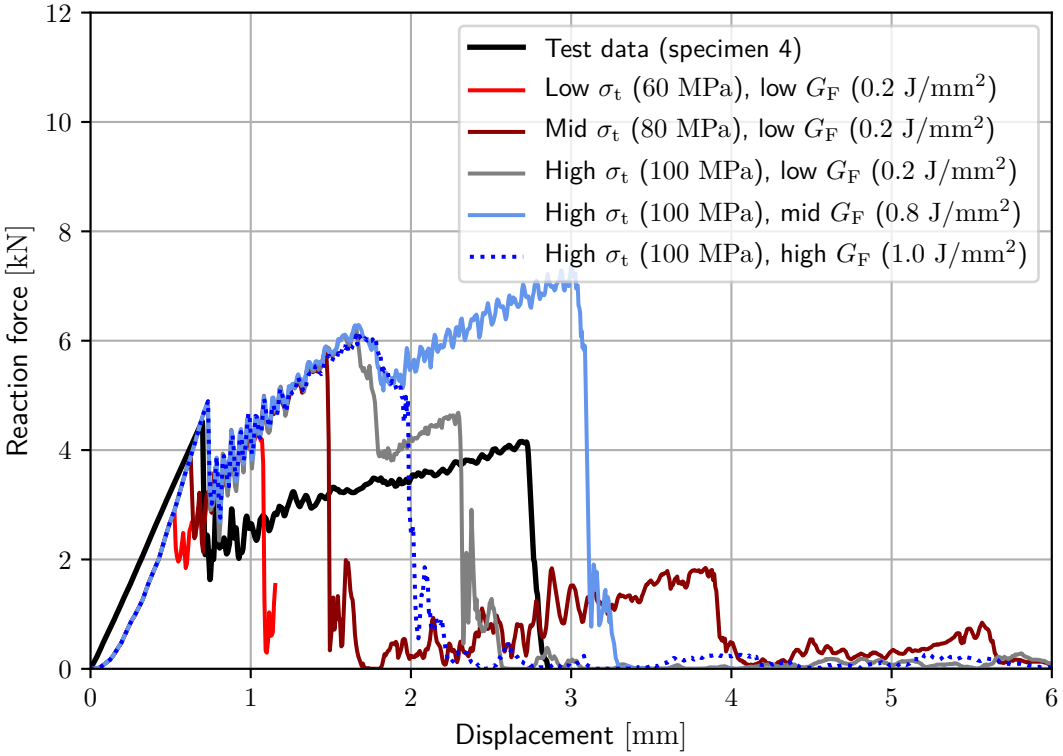


Figure 4.11: Visualization of the effects on the result for different values of $\sigma_t$ and $G_F$.

lower fracture energy leads to an earlier cracking around the area of the striker to hit out the central area of the specimen which results in an earlier drop of reaction force to zero (Figures 4.12c, 4.12d).

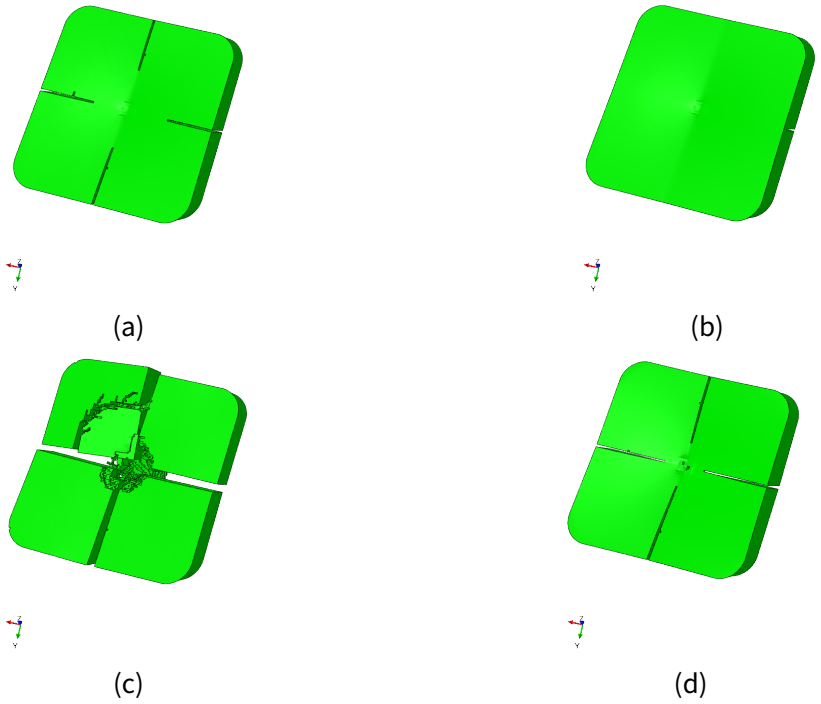


Figure 4.12: Progression of damage for different states during the impact loading. Comparison for low $G_{\mathrm{F}}$ (a, c) and mid $G_{\mathrm{F}}$ (b, d).

Discussing the differences between the mid $G_{\mathrm{F}}$ and high $G_{\mathrm{F}}$ results, again different stages of the loading scenario are visualized (Figure 4.13). For the first stage, the surface opposite to the striker impact is shown (Figures 4.13a, 4.13b). The cracks for the material with mid $G_{\mathrm{F}}$ have already progressed to the specimen's edges at this point. As a consequence, the different sections of the specimen with mid $G_{\mathrm{F}}$ (first 4.13a) are already a bit loose. So the stress at the contact region with the striker is not that high due to a certain mobility of the specimen's sections. On the other hand, the higher $G_{\mathrm{F}}$ leads to a stiffer behaviour as the cracks have not propagated as far as for the mid $G_{\mathrm{F}}$ at this stage. This leads to higher stresses in the contact region. As a result, not only the 4 cracks propagate, but the whole center is hit out of the specimen just after that stage. This explains that the specimen with high $G_{\mathrm{F}}$ already fails at this point. The low and mid $G_{\mathrm{F}}$ show a drop at this displacement due to the 4 cracks propagating throughout the specimen but as the central region is still intact, the specimen is capable of absorbing energy after this damage occurs. Summed up, the fracture energy has an effect on the structural failure behaviour and therefore a more brittle material can shift structural failure to higher displacements. This is an important insight to be considered when trying to represent the test specimens with a material model in FEM.

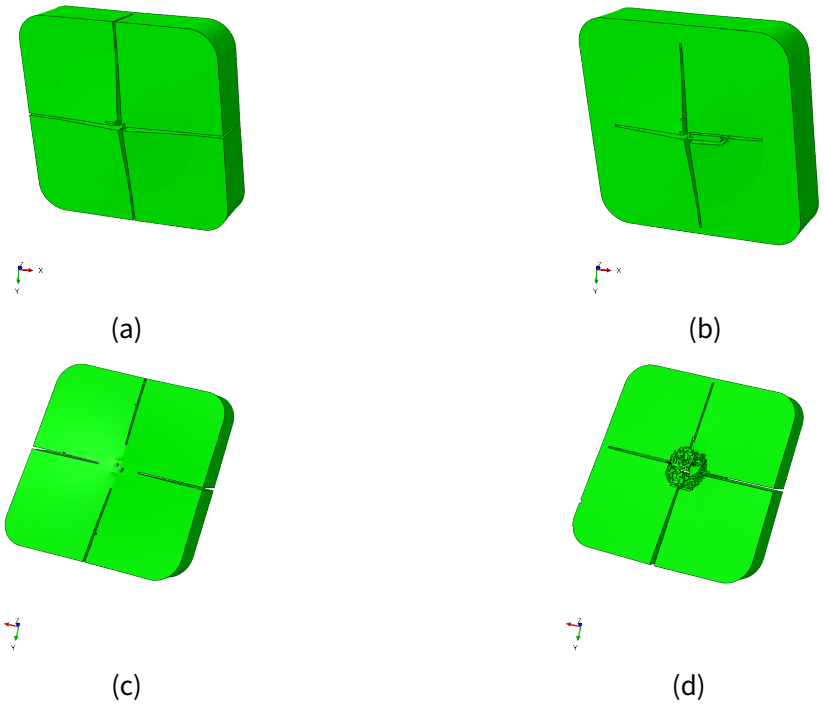


Figure 4.13: Comparison of damage progression for mid $G_{\mathrm{F}}$ (a, c) and high $G_{\mathrm{F}}$ (b, d).

The next two discussed parameters are the element deletion strain $\varepsilon_{\mathrm{del}}$ and the shear-failure strain $\varepsilon_{\mathrm{shear,f}}$. In Figure 4.14, the results for varied values of $\varepsilon_{\mathrm{del}}$ and $\varepsilon_{\mathrm{Shear,f}}$ are shown. The variation of the shear-failure strain $\varepsilon_{\mathrm{shear,f}}$ does not affect the results. According to the knowledge gained in Section 4.1.1, this shows that mode II loading of the developing cracks within the whole specimen is not relevant for the results. Considering the effect of the fracture energy, the information gained varying this parameter is that almost entirely mode I crack opening is occurring within the specimen for this specific test scenario.

Increasing the element deletion strain from the low to the mid value leads to a more abrupt failure at just under $2\,\mathrm{mm}$ of displacement. The material with high element deletion strain, however, shows abrupt failure at just under $3\,\mathrm{mm}$ and therefore the highest displacement of the 3 values. This unexpected variation can be explained using Figure 4.15. Similar to the fracture energy, the element deletion strain affects the structural failure behaviour of the specimen. Thus, a higher value does not necessarily shift final failure to higher displacements. In Figures 4.15a, 4.15b, the state at just under $2\,\mathrm{mm}$ of displacement are shown. For the high element deletion strain $\varepsilon_{\mathrm{del}}$, the state at a displacement of $3\,\mathrm{mm}$ is shown. As the element deletion strain is much higher than the strain at which the elements in the model show zero tensile stiffness, the delayed element deletion leads to excessive distortion and therefore an abortion of the computation. But the capability of a completely damaged element to withstand compressive stresses – as investigated in Section 4.1.1 – leads to much higher reaction forces at displacements above $2\,\mathrm{mm}$.So, the influence of $\varepsilon_{\mathrm{del}}$ in combination with the brittle material damage model is shown and has to be considered when calibrating a material model to represent the specimen's test performance.

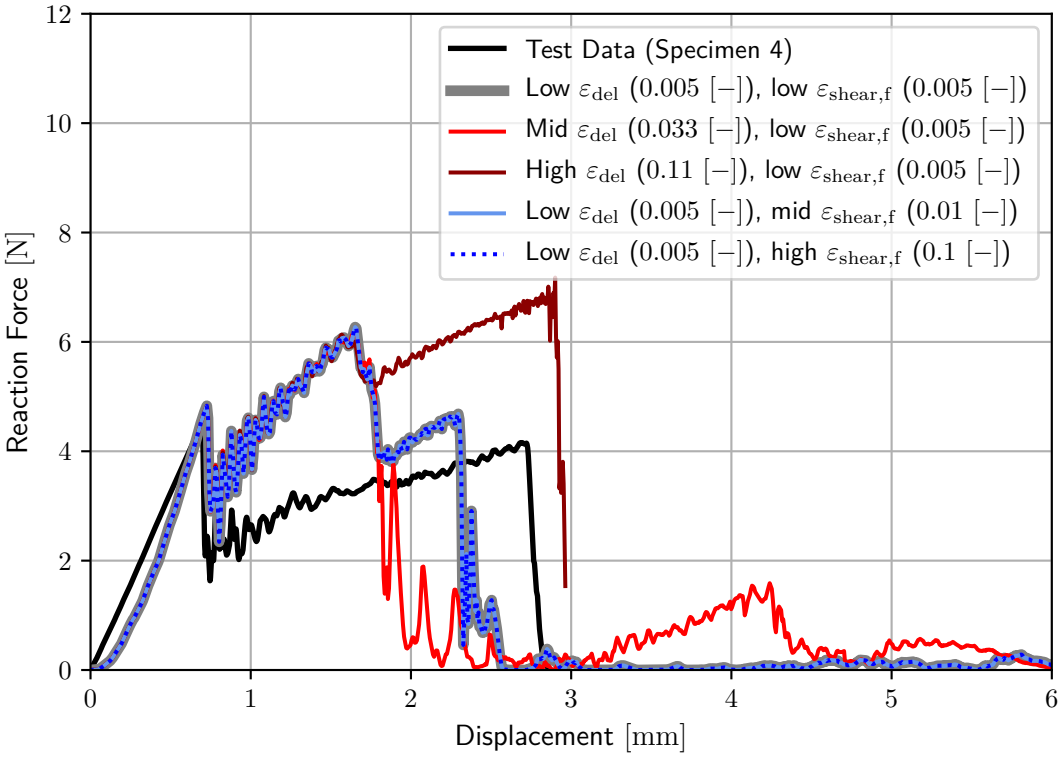


Figure 4.14: Effects of the parameters $\varepsilon_{\mathrm{del}}$ and $\varepsilon_{\mathrm{shear,f}}$ on the results.

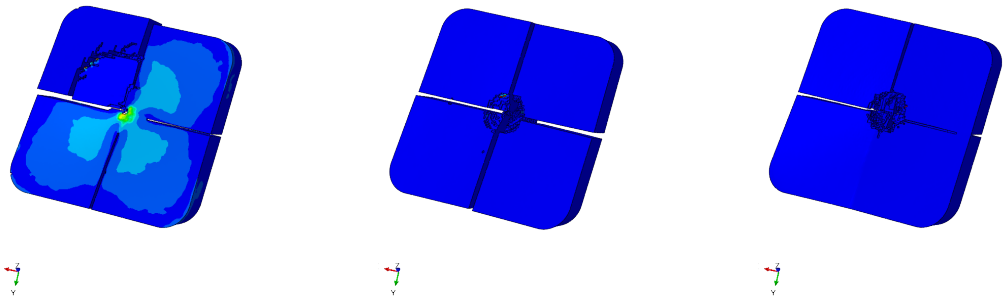

(a) (b) (c)

Figure 4.15: Comparison of damage progression for different values of element deletion strain $\varepsilon_{\mathrm{del}}$. (a): Low value of $\varepsilon_{\mathrm{del}}$, (b): Mid value of $\varepsilon_{\mathrm{del}}$, (c): High value of $\varepsilon_{\mathrm{del}}$.

As described in Section 3.3.2, the post-cracking stress-strain curve is generally modelled as a linear function $\sigma(\varepsilon)$. For the parameter studies, this post-cracking model is extended to see the effect of different post-cracking stress functions on the results. Instead of a linear function, a power law is implemented (equation 4.2). In Figure 4.16a, the post-cracking stress-strain curves dependent on the exponent $p$ (penalty factor) are shown. For a tabular input to the damage model, a piecewise linear curve with $10$ data points is computed.

$$\sigma = \sigma_{\mathrm{t}} \cdot \left(1 - \frac{\varepsilon}{\varepsilon_{\mathrm{True,fail}}}\right)^{p} \tag{4.2}$$

In Figure 4.16b, the results for several values of $p$ are shown (keeping $\varepsilon_{\mathrm{True,fail}}$ constant). Concerning the reaction force, the parameter $p$ has no influence, which means that $p$ does not shift the reaction force to higher nor lower values. The displacement of abrupt failure is shifted with varying $p$. The explanation is the same as for the varying fracture energy before. As the penalty factor alters the stiffness of an element at a certain post-cracking strain, the structural failure behaviour is influenced by the penalty factor. Therefore, similar to the fracture energy, a more brittle material model can shift structural failure to higher displacements.

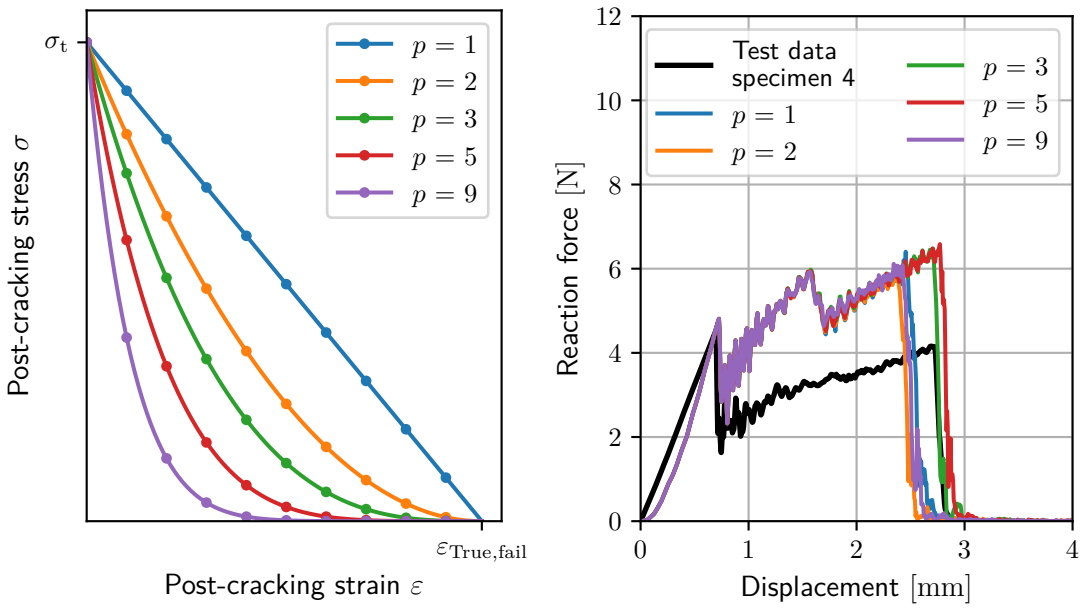


(a) Visualization of the curves according to equation 4.2 with 10 data pairs.

(b) Effect of the exponent $p$ from equation 4.2 on the results.

Figure 4.16: Visualization of (a) various post-cracking stress-strain curves and (b) their influence on the simulation results.

Considering general contact in the model, the parameter $\mu_{\mathrm{gen}}$ is varied. In Figure 4.17, the force-displacement curves for different values of $\mu_{\mathrm{gen}}$ are shown. As seen in the Figure, a higher $\mu_{\mathrm{gen}}$ leads to slightly higher reaction forces. However, there is no trend for the displacement at which abrupt failure occurs. While increasing $\mu_{\mathrm{gen}}$ from $0.2$ to $0.5$ results in delayed failure, a coefficient of friction for the general contact $\mu_{\mathrm{gen}}$ of $0.8$ shows an earlier failure. As for the other parameters, an increasing value of $\mu_{\mathrm{gen}}$ shifts abrupt failure to higher displacements. However, at some extent the structural failure behaviour changes and therefore leads to earlier final failure (Figure 4.18).

The last parameter discussed is the coefficient of friction, $\mu$, between the clamping/-supporting ring and the specimen. As seen in Figure 4.19, the effect of $\mu$ on the results is following the same mechanisms as the general contact. For a low value of $\mu$, the broken parts of the specimen are able to slip away from the center of the clamp. Therefore, the specimen breaks earlier and does not stay in place such as for higher values of $\mu$. The increase from the mid value of $\mu$ to the high value gives the same picture as

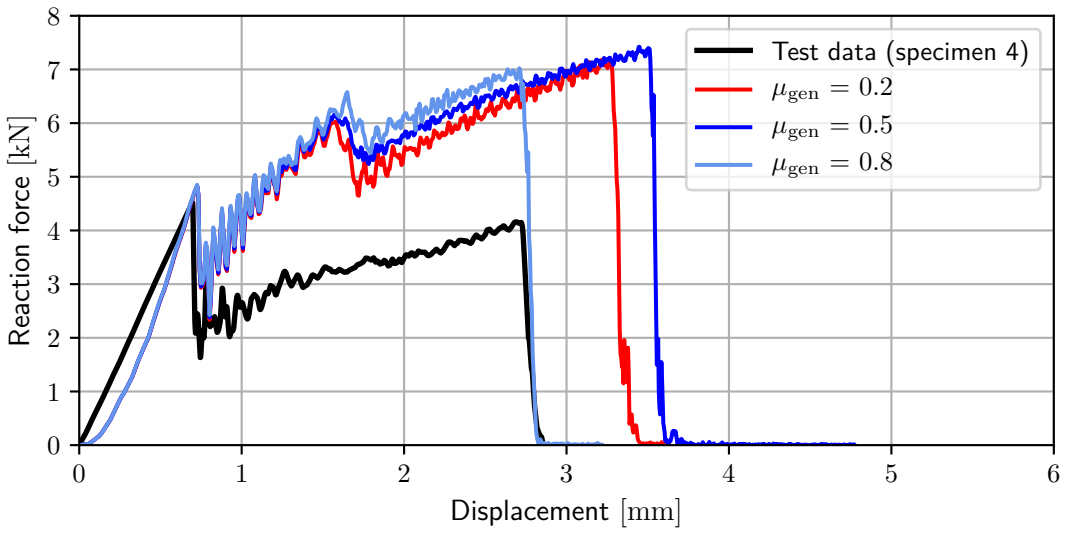


Figure 4.17: The effect of varying the coefficient of friction $\mu_{\text{gen}}$.

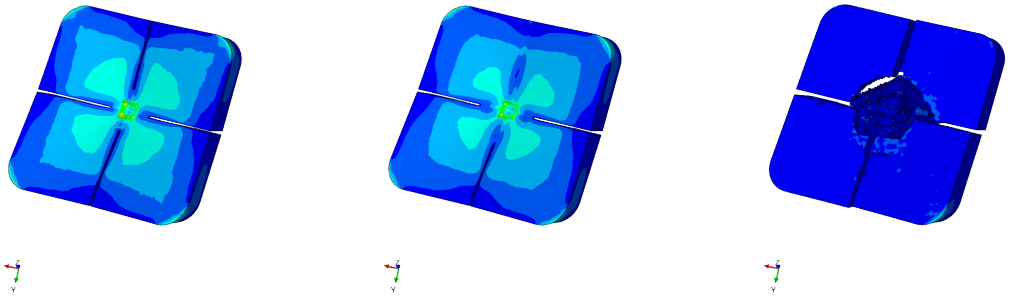

(a) (b) (c)

Figure 4.18: Comparison of damage progression for different values of the coefficient of friction for general contact $\mu_{\text{gen}}$. (a): $\mu_{\text{gen}} = 0.2$, (b): $\mu_{\text{gen}} = 0.5$, (c): $\mu_{\text{gen}} = 0.8$.

for the earlier discussed parameters which influence the structural failure behaviour of the specimen. The specimen takes more force but then the abrupt failure happens at a lower displacement for the high value of $\mu$ than for the mid value of $\mu$. This is due to the change of structural failure, as seen in Figure 4.20

As a summary, all discussed parameters are listed in Table 4.7. If there is a consistent trend visible for the influence of one parameter on the results it is also noted in the Table. This Table is the basis for calibrating the material model to fit the force-displacement curve of test specimen 4.

### 4.3.2 Ductile damage model

Additionally to the brittle damage model, it is attempted to approximate the solid infill geometry using the ductile material damage model (described in Section 2.2.3.1). The reason for this test is that with only one material (and damage) model the performance

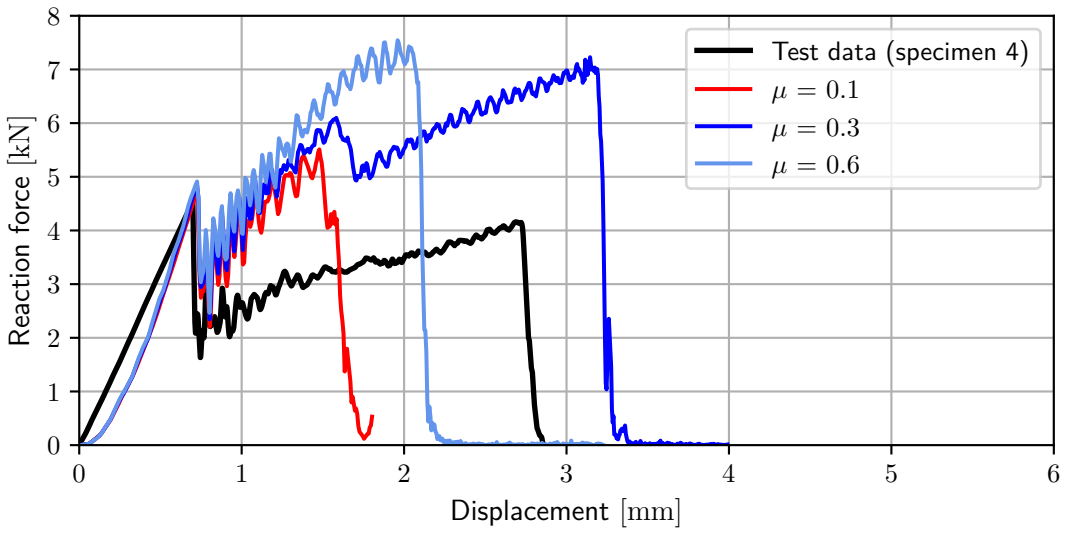


Figure 4.19: The effect of varying coefficient of friction $\mu$ between the clamping/supporting ring and the specimen.

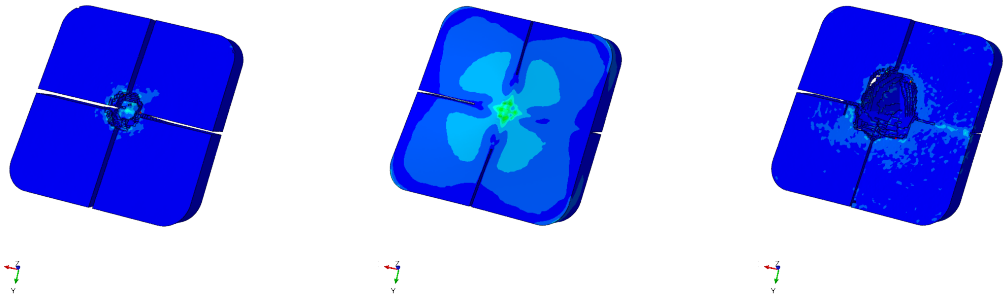

(a) (b) (c)

Figure 4.20: Comparison of damage progression for different values of the coefficient of friction for the contact between the specimen and the rings $\mu$. (a): Low value of $\mu$, (b): Mid value of $\mu$, (c): High value of $\mu$.

of any infill geometry should be predicted via FE-simulation. Therefore, these two damage models are implemented and the ability to approximate the force-displacement curves is compared.

The ductile damage model described in Section 2.2.3.1 is used. Therefore, the parameter for the damage initiation criterion is the plastic fracture strain $\varepsilon_{\mathrm{f}}^{pl}$. The stiffness of the material is then reduced as a function of damage. The second parameter affecting the force-displacement curve is the displacement at failure $u_{\mathrm{f}}$, which is the displacement at which an element is completely damaged and therefore deleted in the model. Varying these two parameters, it is attempted to fit the curve of test specimen 4.

In Figure 4.21, the reference curve of the impact tests is compared to simulation results using the ductile damage behaviour. The force-displacement curve before first damage can be calibrated quite well. Nevertheless, the ductile damage model leads to several peaks after first damage instead of completely cracking at some point. No matter how

Table 4.7: Overview of the effects of the material model using brittle damage model on the results.

| Parameter | Effect on the results for increasing parameter value |
|---|---|
| Young's modulus $E$ | Higher reaction forces, delayed failure |
| Poisson's ratio $\nu$ | Earlier failure |
| Tensile strength $\sigma_{\mathrm{t}}$ | Shifted first damage and abrupt failure |
| Fracture energy $G_{\mathrm{F}}$ | No influence on reaction force<br>Impact on structural failure behaviour |
| Failure strain $\varepsilon_{\mathrm{f}}$ | Impact on structural failure |
| Shear-failure strain $\varepsilon_{\mathrm{shear,fail}}$ | No influence |
| Penalty factor $p$ | Constant reaction forces<br>Similar effect as fracture energy |
| Coefficient of friction $\mu$<br>clamping/supporting – specimen | Higher reaction forces<br>Impact on structural failure |
| Coefficient of friction $\mu_{\mathrm{gen}}$<br>general contact | Higher reaction forces<br>Impact on structural failure |

the parameters of the ductile damage model are varied, the abrupt failure of the solid plate cannot be reproduced. For specimens with low infill densities, this damage model might lead to more reasonable results, but for the solid plate, the computation gives a completely wrong failure behaviour. As a result, the amount of energy dissipated by the solid specimen is far too high compared to the test results.

In Figure 4.22, the failure pattern of the specimen using the ductile damage model is shown. Using the ductile damage model, the striker leaves a smooth hole with the striker's diameter. This is a completely different failure pattern than the test specimens show (Figure 2.12 on page 15).

Considering the failure pattern and the force-displacement curves for both, the ductile and brittle damage model, the brittle damage model is used for the following investigations.

## 4.4 Reference material models based on the solid specimen

In this section, two calibrated material models approximating the test data are described. After every computation, the resulting force-displacement curve is compared to the curve of test specimen 4. Following the comparison of the curves, the parameters of the material and damage model are varied based on their effect on the results (Section 4.3). This process is repeated until the FE model approximates the test curve properly. However, it is not possible to fit the whole curve for the experiment of specimen 4. Therefore, two models are used for predicting different infill geometries.

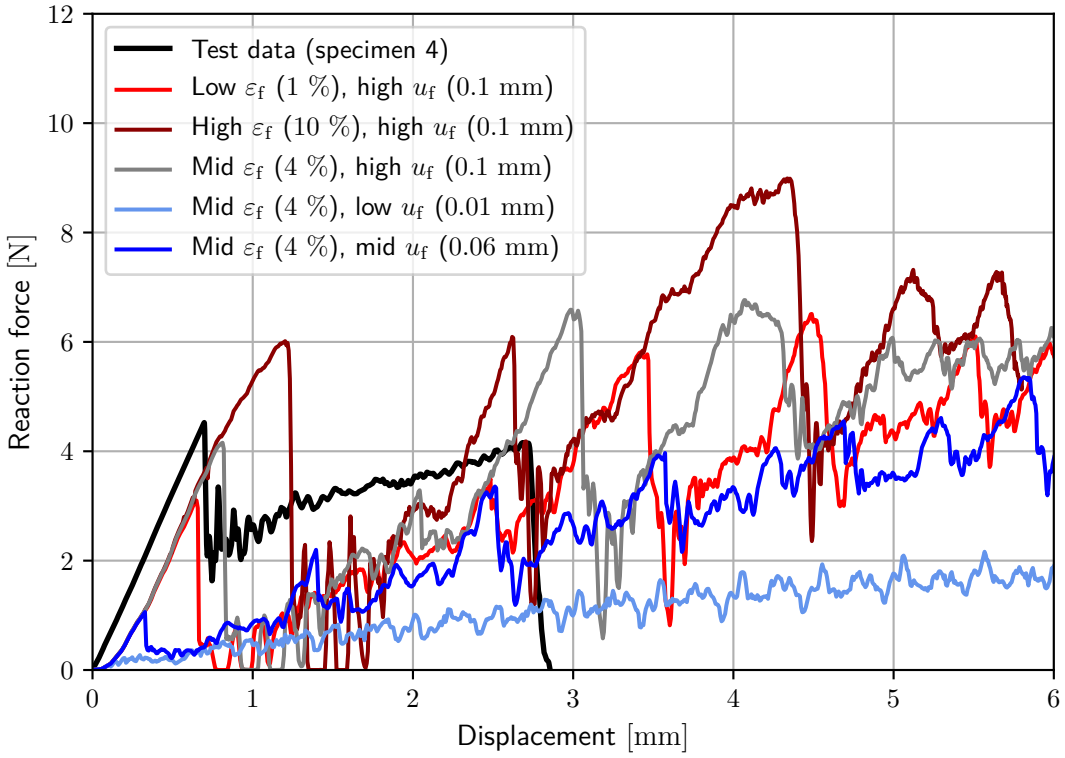


Figure 4.21: Force-displacement curves of the ductile damage model with varied parameters $\varepsilon_f$ and $u_f$

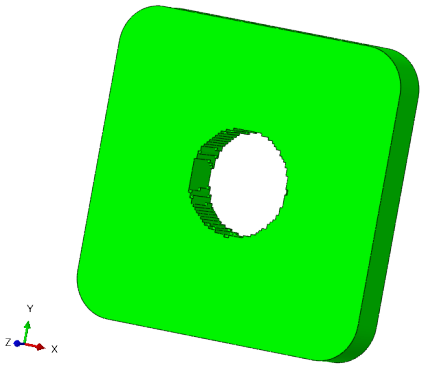

Figure 4.22: Visualization of the failure pattern of the solid specimen using the ductile damage model

### 4.4.1 Material model 1

For the first material model, a high Young's modulus with a value of $E = 5500\,\mathrm{MPa}$ and tensile strength of $\sigma_t = 100\,\mathrm{MPa}$ are chosen. With these values for $E$ and $\nu$, the slope in the force-displacement curve up to first damage can be represented quite well (Figure 4.23). However, using this material model results in too high reaction forces after first damage. Calibrating the Poisson's ratio $\nu$, the penalty factor $p$ and the coefficients

of friction $\mu$, respectively $\mu_{\mathrm{gen}}$, the abrupt failure of the experimental data at approximately $2.75\,\mathrm{mm}$ is met well. All parameters and their values chosen for material model 1 are listed in Table 4.8.

### 4.4.2 Material model 2

In material model 2, a lower Young's modulus of $E = 2500\,\mathrm{MPa}$ is chosen. To meet the displacement of first failure with the lower Young's modulus, the tensile strength is also decreased with $\sigma_{\mathrm{t}} = 67\,\mathrm{MPa}$ (Figure 4.23). For the complete range of displacement, these decreased parameters lead to lower reaction forces. The basic idea of this material model is contrary to material model 1. Material model 2 (low $E$) should approximate the experimental data after first damage and not the range up to first damage. As a consequence, the reaction force up to first damage is underestimated using this material model. After first damage, the reaction force is slightly higher than for test specimen 4. Again, the displacement at which abrupt failure occurs can nearly be met. As for material model 1, all parameters and their values are listed in Table 4.8.

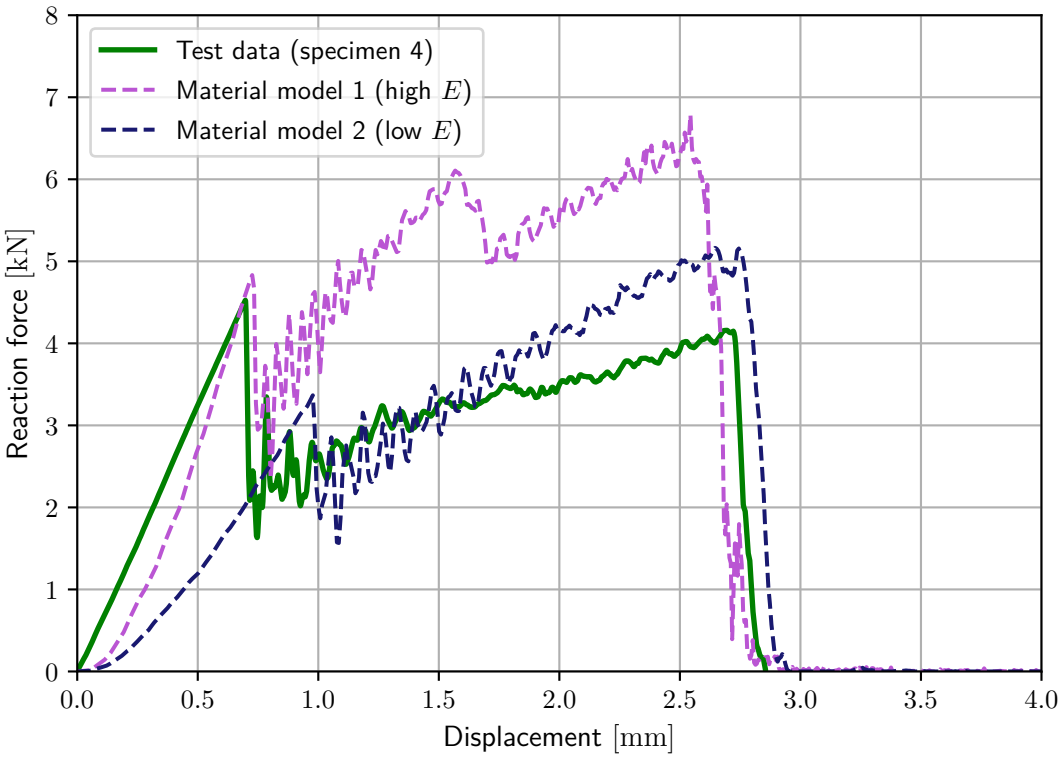


Figure 4.23: Comparison of the test data against the two acquired material models.

### 4.4.3 Comparison of the test results to the developed material models

In Figure 4.24, the dissipated energy for the test as well as for the simulations using the discussed material models is shown. As the experiments vary widely, no specimen

Table 4.8: Overview of the material parameters for the material models based on the results for the solid specimen.

| Parameter | Material Model 1 | Material Model 2 |
|---|---|---|
| Young's modulus $E$ [MPa] | 5500 | 2500 |
| Poisson's ratio $\nu$ [−] | 0.33 | 0.32 |
| Tensile strength $\sigma_{\mathrm{t}}$ [MPa] | 100 | 67 |
| Fracture energy $G_{\mathrm{F}}$ [J/mm²] | $6 \cdot 10^{-4}$ | $6 \cdot 10^{-4}$ |
| Failure strain $\varepsilon_{\mathrm{f}}$ [−] | 0.1 | 0.1 |
| Shear-failure strain $\varepsilon_{\mathrm{shear,f}}$ [−] | $2.4 \cdot 10^{-5}$ | $3.6 \cdot 10^{-5}$ |
| Penalty factor $p$ [−] | 3 | 1 |
| Coefficient of friction $\mu$ [−] clamping/supporting ring – specimen | 0.3 | 0.3 |
| Coefficient of friction $\mu_{\mathrm{gen}}$ [−] general contact | 0.37 | 0.4 |

exactly meets the mean value. Table 4.9 shows the deviation from the mean value for all test specimens and the material models. Material model 1 overestimates the dissipated energy of specimen 4 by approximately 20 % and the mean value by approximately 30 %. Material model 2 underestimates the experimental data of specimen 4 by approximately 15 % and the mean value by approximately 7 %. Regarding the deviation in test results, material model 2 gives a good approximation to the mean value.

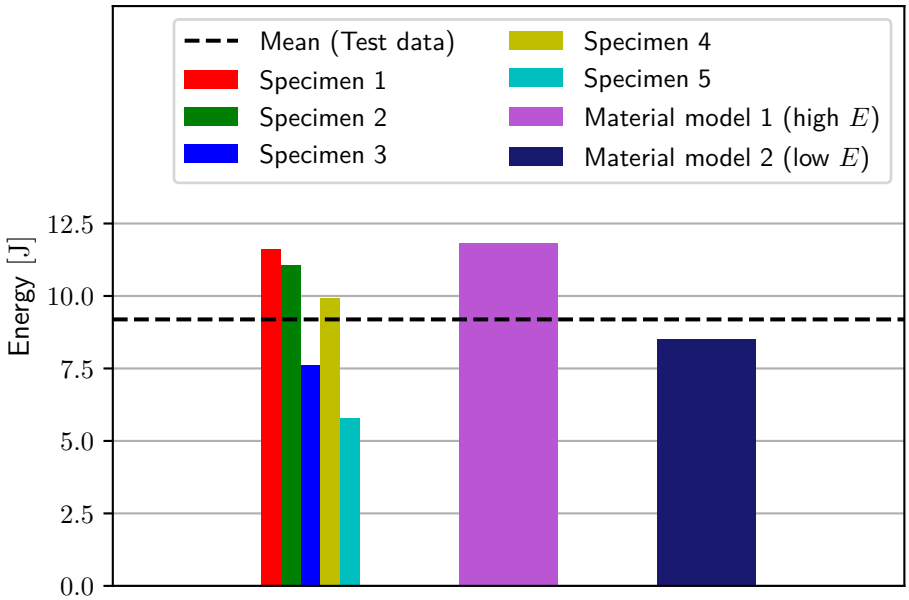


Figure 4.24: Comparison of the dissipated energy of the test specimens and the material models.

Finally, the failure pattern for the two material models is observed. The results are shown in Figure 4.25 together with the failure pattern of the test specimen in [8]. The brittle damage model approximates the failure pattern in terms of 4 cracks across the specimen well. The direction of the cracks, though, is deviating from the experimental

Table 4.9: Overview of the deviation from the mean value of dissipated energy for the test and model results.

| Result | Dissipated energy [J] | Deviation from mean value |
|---|---|---|
| Mean | 9.19 | - |
| Specimen 1 | 11.62 | + 26.40 % |
| Specimen 2 | 11.04 | + 20.13 % |
| Specimen 3 | 7.60 | + 17.30 % |
| Specimen 4 | 9.93 | + 8.05 % |
| Specimen 5 | 5.77 | − 37.21 % |
| Material model 1 | 11.81 | + 28.51 % |
| Material model 2 | 8.49 | − 7.62 % |

results. In the experiments, the crack direction is perpendicular to the extrusion direction of the 3D-printing process. In the computation, the cracks follow the direction of the mesh.

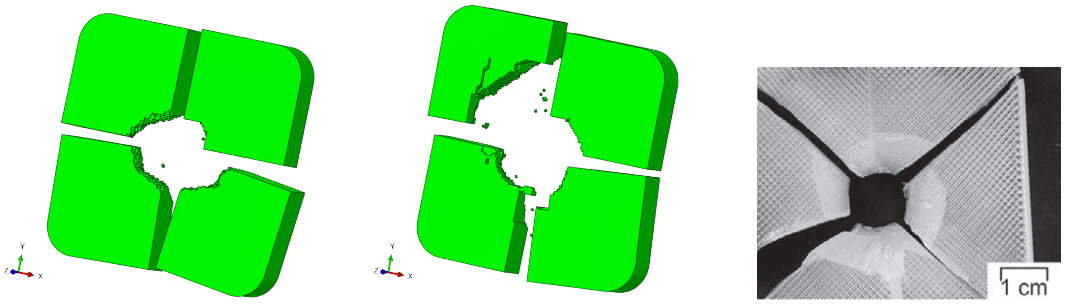


(a) (b) (c)

Figure 4.25: Visualization of the failure patterns for (a) material model 1, (b) material model 2 and (c) the test specimen.

Using the brittle damage model in ABAQUS, the strength of an element varies whether it is loaded in normal or diagonal direction. Keeping Figure 4.25 in mind, the cracks propagate in the direction the mesh is aligned. Based on this information, the mesh of the FE model is set up in a way that the crack direction of the experiments is the direction in which the elements are aligned (Figures 4.26a, 4.26b). The idea of doing so is to better represent the crack directions and the level of reaction force after first damage. Figure 4.26c shows that the rotated mesh represents the crack directions of the test well. Nevertheless, the thought that this representation of the failure behaviour also leads to a better approximation of the force-displacement curves of the experiments is proved wrong. Despite the differences in crack propagation and better representation of the failure pattern, the level of reaction force after first damage is nearly unaltered for the new mesh (Figure 4.27). As a consequence, the regular mesh (described in Section 3.2.4.1) is used for the following observations. Still, there is an influence of the mesh on the failure pattern which may make the use of randomly generated meshes useful for similar investigations.

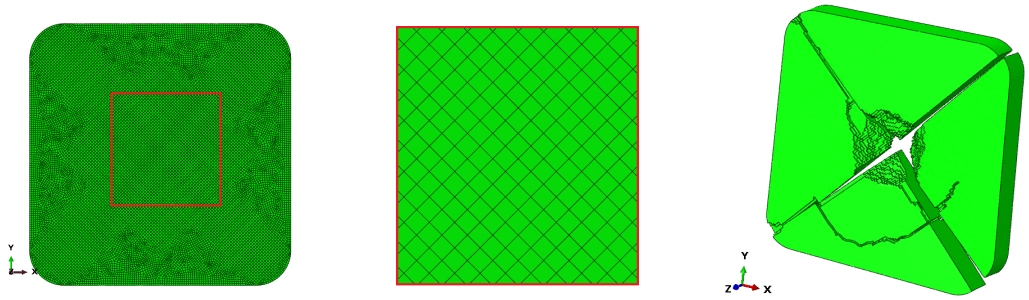

(a) (b) (c)

Figure 4.26: Visualization of (a,b) the rotated mesh and the failure pattern (c) as a result of this mesh.

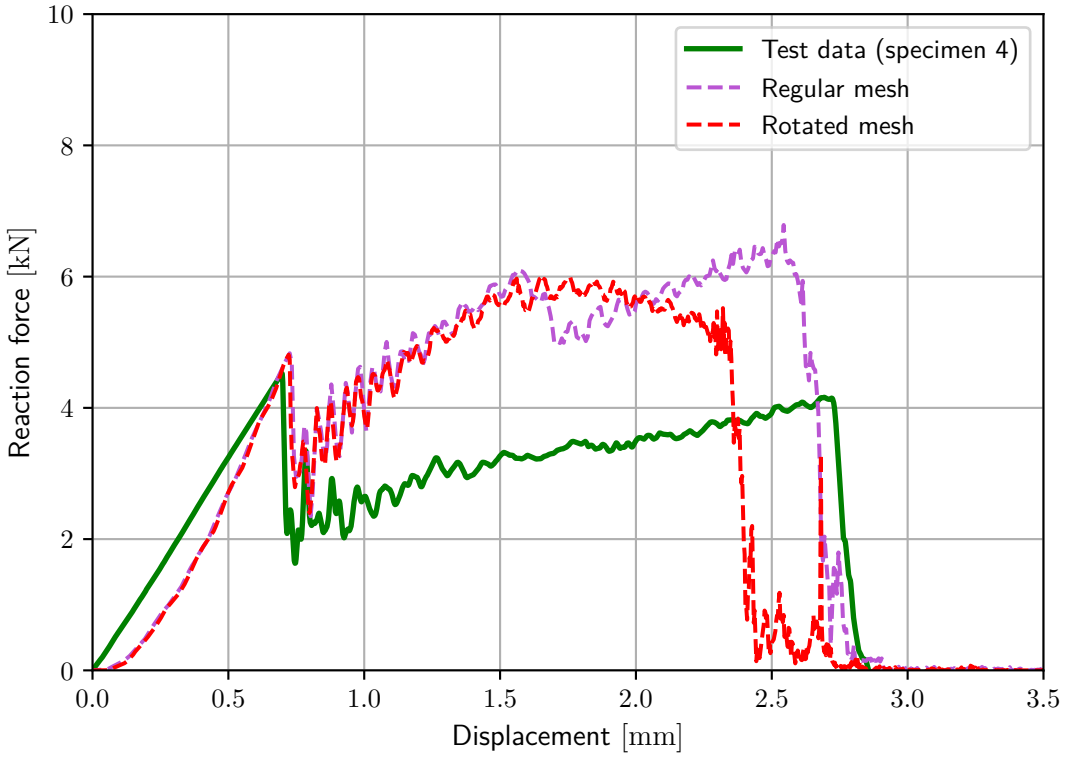


Figure 4.27: Comparison of the test results for material model 1 with the regular and rotated mesh.

## 4.5 Prediction of a linear grid infill structure

A FEM model is set up with the developed material models from Section 4.4 with a varied infill geometry. Then, the accuracy of the predictions of both models is evaluated with impact tests. In Figure 4.28, the infill structure of the observed specimen geometry is shown. All ribs inside the specimen are $2\,\mathrm{mm}$ in width with a distance of $3\,\mathrm{mm}$ in between.

Firstly, the experimental results for the 5 printed and tested specimens are visualized (Figure 4.29). Similar to the solid specimens, the test results vary widely. As the curves

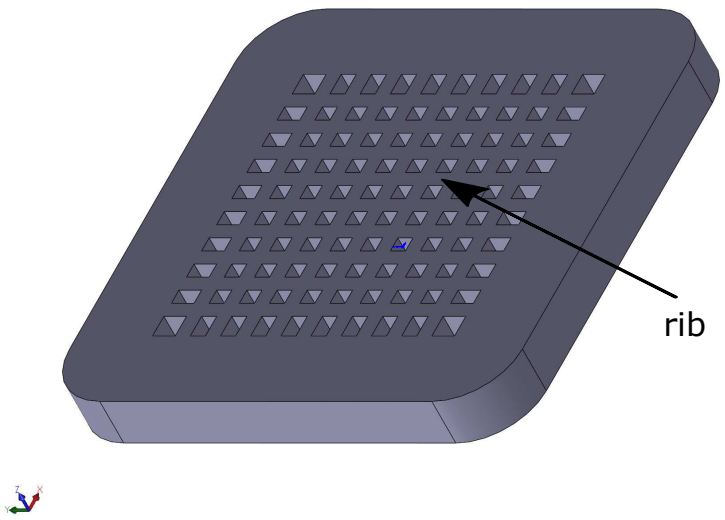


Figure 4.28: Visualization of the grid infill geometry.

for specimens 1 and 3, as well as the curves for specimens 2 and 4 are similar, the curves for the specimens 1, 4 and 5 are compared to the reference material model simulation results in the next sections. In Table 4.10, the values for the dissipated energy for the specimens are given as well as the mean value.

Table 4.10: Comparison of the absorbed energy for the grid infill specimens.

| Specimen | Dissipated energy $[\mathrm{J}]$ |
|---|---|
| 1 | $0.89$ |
| 2 | $2.29$ |
| 3 | $0.89$ |
| 4 | $2.61$ |
| 5 | $1.04$ |
| Mean | $1.54$ |

### 4.5.1 Material models 1 and 2 used for the grid specimen

In Figure 4.30, the simulation results using the reference material models from Section 4.4 are shown as well as the representative test curves. As expected, reference material model 1 overestimates the reaction force and therefore the dissipated energy. While the displacement of failure is met well for reference material model 1, reference material model 2 shows a reaction force at displacements higher than $2\,\mathrm{mm}$. The reason for that is shown in Figure 4.31. After the striker nearly knocks out a smooth hole of the specimen (just under $2\,\mathrm{mm}$ of displacement), there is still a bunch of material in the way of the striker. That material is bent away from the striker due to the previous deformation, but when the striker gets into contact with this part of the specimen, again there

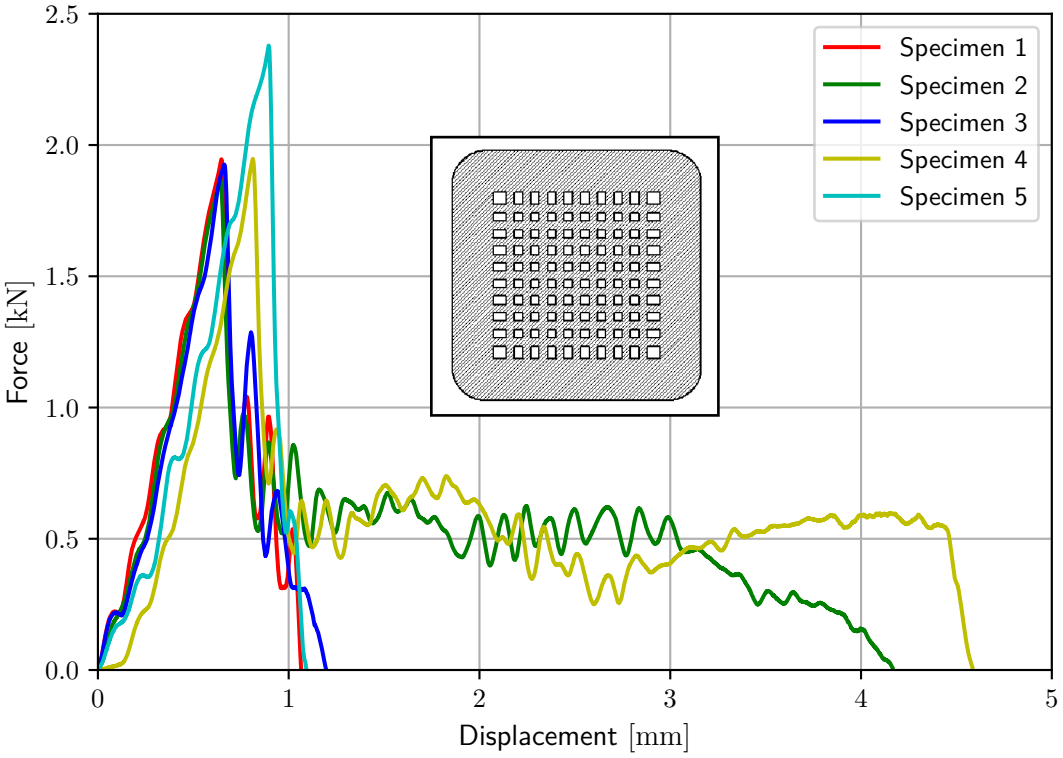


Figure 4.29: The Force-displacement curves from the impact tests for the linear grid infill specimens.

is a reaction force after the drop of reaction force at $2\,\mathrm{mm}$ of displacement. For this geometry, material model 2 overestimates the dissipated energy by approximately $163\,\%$. Therefore, this material model seems useless for other geometries than the solid specimen. Although reference material model 1 also overestimates the dissipated energy by $37\,\%$, the overestimation is in an order of magnitude similar to the deviation for the solid specimen. In Table 4.11, the dissipated energy for the reference material models is given together with the deviation from the mean value of the experiments.

Table 4.11: Comparison of the absorbed energy of the two reference material models to the mean of the test results.

| Model | Dissipated energy [J] | Deviation from mean value |
|---|---|---|
| Mean (test data) | 1.54 | - |
| Material model 1 | 2.11 | + 37.01 % |
| Material model 2 | 4.05 | + 162.99 % |

### 4.5.2 Development of a new material model for the grid infill

The reference models for the solid specimen are no good approximations for the test with the grid infill structure. Therefore, a new material model for the grid infill structure is developed and then all reference materials are evaluated concerning the prediction of other infill structures. As the peak of first damage is represented quite well by reference material model 2, the values for the Young's modulus $E$ and tensile strength $\sigma_\mathrm{t}$

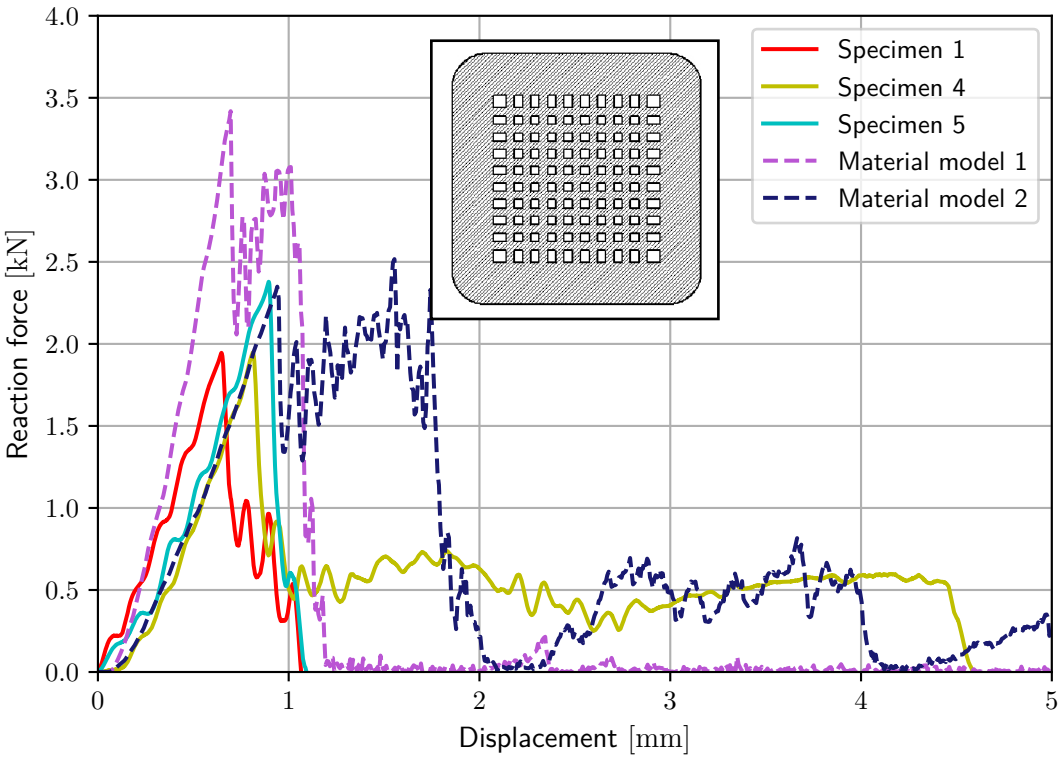


Figure 4.30: The experimental results compared to the results of the reference material model 1.

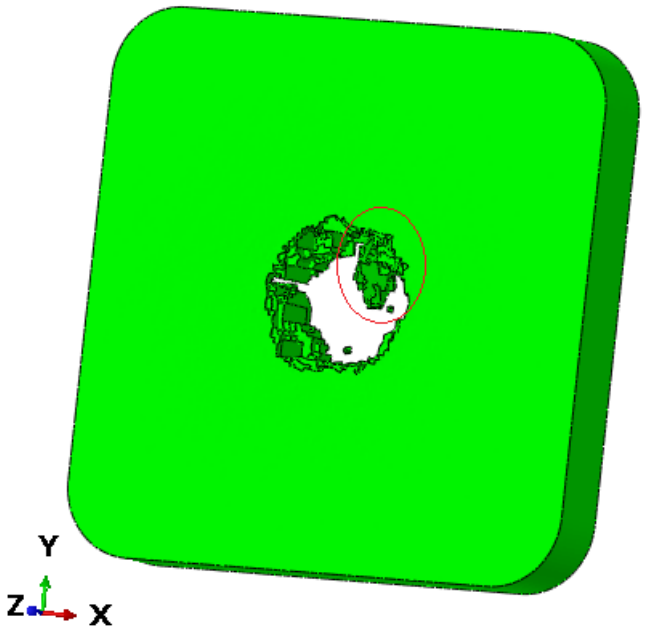


Figure 4.31: Visualization of the material that comes into contact with the striker for material model 2.

are maintained for the new material model. As described for material models 1 and 2 in Section 4.4, the force-displacement curve of the tests and computation are compared. Then the parameters of the material and damage model are varied based on the effects on the results to better approximate the experimental data.

In Figure 4.32, the force-displacement curve of the developed material model 3 for the grid infill structure can be seen in comparison to the test results. The slope of the reaction force until first damage is a good compromise of the shown test curves. However, neither the abrupt failure of specimen 5 nor the reaction force for high displacements of specimen 4 can be approximated well. Besides the high reactions forces after first damage, material model 3 is a good compromise for the highly scattering test results. The dissipated energy using this model is $1.75\,\mathrm{J}$. Considering the mean value of all test results being $1.54\,\mathrm{J}$, the energy absorbed in this model is overestimated by approximately $14\,\%$. The parameters of reference material model 3 are shown in detail in Table 4.12.

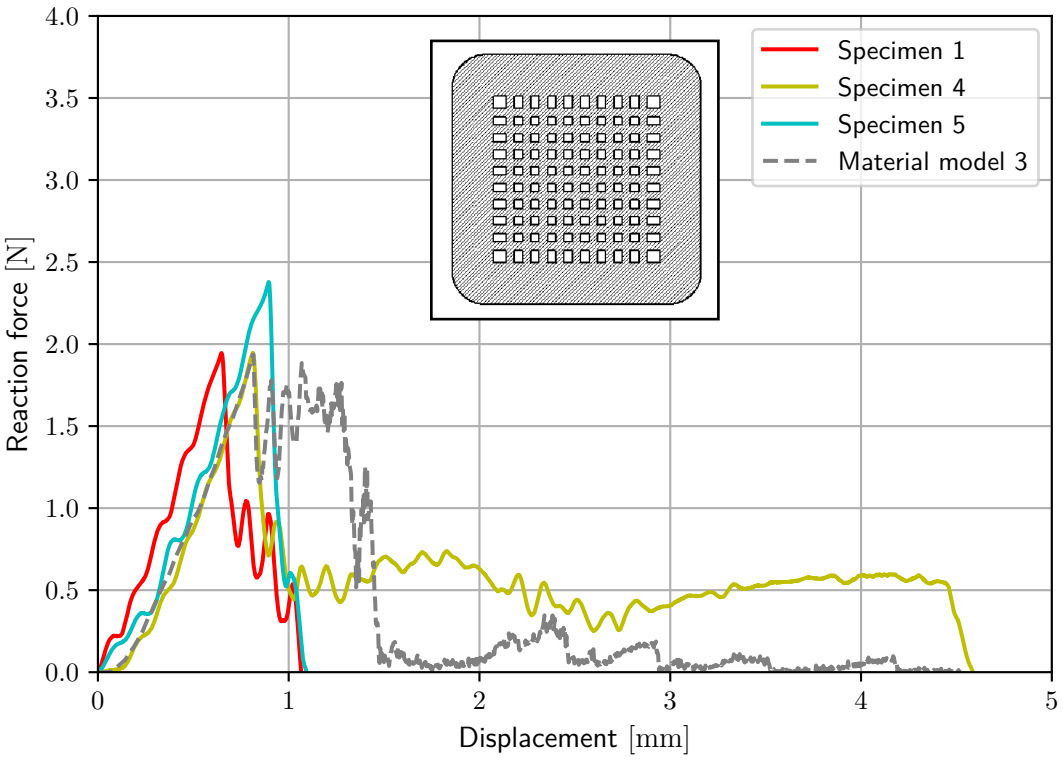


Figure 4.32: Comparison of the material model 3 simulation results to the test results for the grid infill structure

In Table 4.13, the mean value of the dissipated energy for the test result is shown again with the value and deviation for each of the 3 reference material models for a better overview. In Figure 4.33, the dissipated energy for all test specimens and the reference material models is shown using a bar chart again as for the solid specimen in Section

Table 4.12: Overview of the material parameters for the reference material model 3.

| Parameter | Material Model 3 |
|---|---|
| Young's modulus $E$ $[\mathrm{MPa}]$ | $2500$ |
| Poisson's ratio $\nu$ $[-]$ | $0.32$ |
| Tensile strength $\sigma_{\mathrm{t}}$ $[\mathrm{MPa}]$ | $55$ |
| Fracture energy $G_{\mathrm{F}}$ $[\mathrm{J/mm^2}]$ | $6 \cdot 10^{-4}$ |
| Failure strain $\varepsilon_{\mathrm{f}}$ $[-]$ | $0.1$ |
| Shear-failure strain $\varepsilon_{\mathrm{shear,f}}$ $[-]$ | $4.4 \cdot 10^{-5}$ |
| Penalty factor $p$ $[-]$ | $1$ |
| Coefficient of friction $\mu$ $[-]$ | |
| clamping/supporting ring – specimen | $0.3$ |
| Coefficient of friction $\mu_{\mathrm{gen}}$ $[-]$ | |
| general contact | $0.4$ |

4.4.3. Naturally, reference material model 3 best represents the test results for the specimens with grid infill structure, as it was calibrated to approximate the grid infill structure test results.

Table 4.13: Comparison of the mean value for dissipated energy of the test results against the results for all 3 reference material models

| Model | Dissipated energy $[\mathrm{J}]$ | Deviation from mean value |
|---|---|---|
| Mean (test results) | $1.54$ | - |
| Material model 1 | $2.11$ | $+\ 37.01\ \%$ |
| Material model 2 | $4.05$ | $+\ 162.99\ \%$ |
| Material model 3 | $1.75$ | $+\ 13.64\ \%$ |

### 4.5.3 Failure pattern of the test specimens and the simulation results for the grid infill structure

In Figure 4.34, the failure patterns of the 5 tested specimens are shown. The test specimens show a similar failure pattern as the solid specimens. Contrary to the test results, all 3 developed material models show a smooth hole due to impact instead of completely cracking (Figure 4.35). Therefore, in terms of failure pattern the simulation results are not suitable for predicting the actual failure pattern of the physical specimens.

### 4.5.4 Validation of the new material model using the solid specimen structure

A simulation of the solid specimen using material model 3 is done, as there are no results for that geometry yet. In Figure 4.36, the chosen representative test curve (Section 4.2) is compared to all 3 reference material models. The slope up to the first peak is close to reference material model 2. However, reference material model 3 leads to

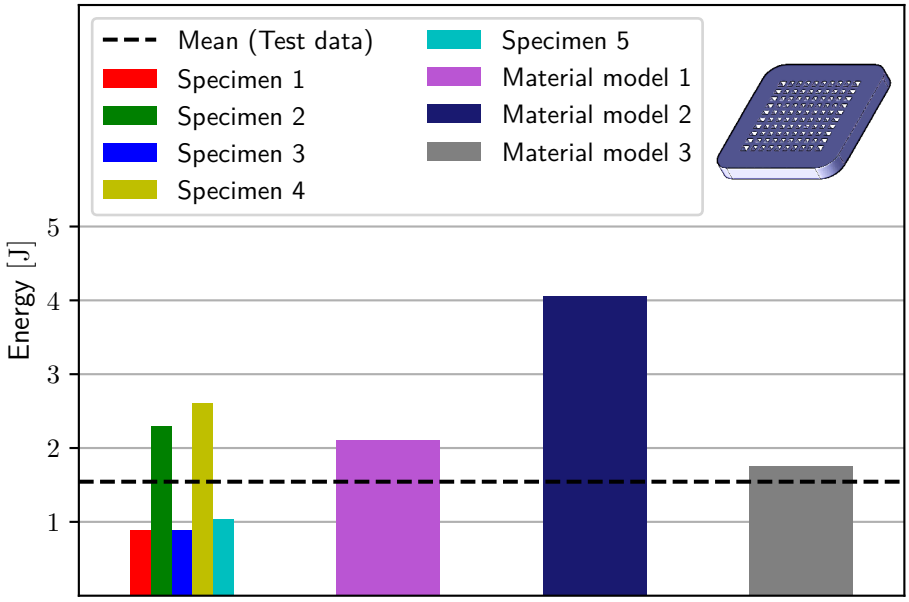


Figure 4.33: Comparison of the dissipated energy of the test specimens with the grid infill structure and the material models.

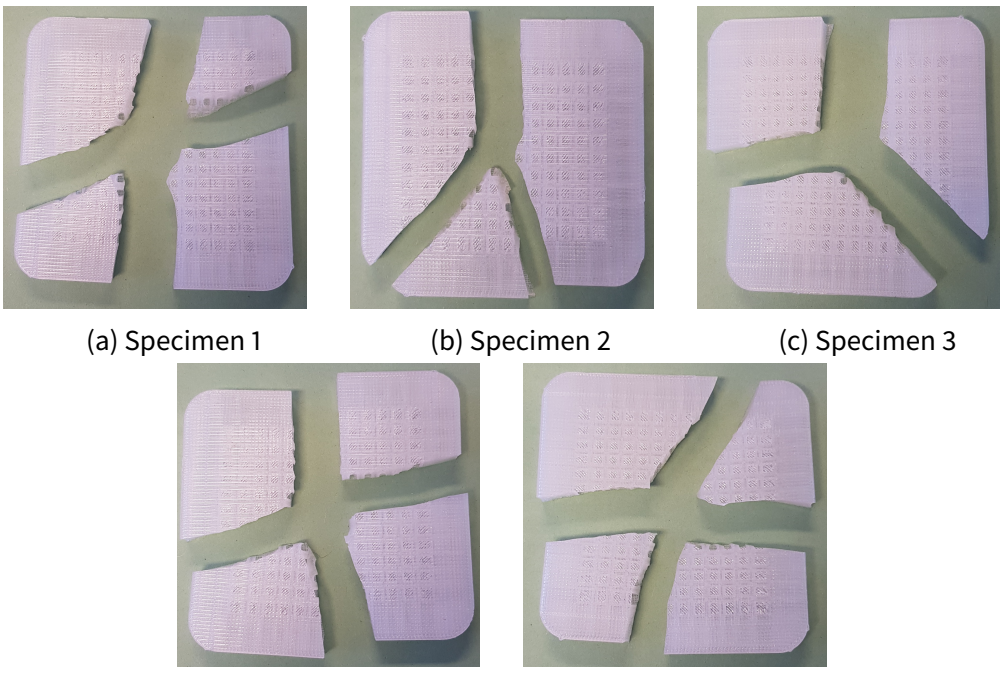

(a) Specimen 1 (b) Specimen 2 (c) Specimen 3

(d) Specimen 4 (e) Specimen 5

Figure 4.34: Failure patterns of the specimens with the grid infill geometry.

abrupt failure significantly earlier resulting in an underestimation of dissipated energy. The computed absorbed energy using reference material model 3 is $5.19\,\mathrm{J}$. The mean of all test specimens is $9.19\,\mathrm{J}$, which means that reference material model 3 underestimates the dissipated energy by approximately $44\,\%$. In Table 4.14, the results of all 3 reference materials are listed for both geometries with their deviation from the mean

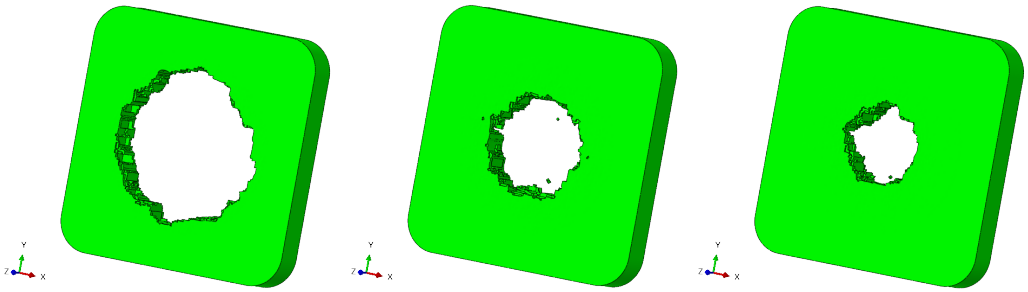

(a) Material model 1 (b) Material model 2 (c) Material model 3

Figure 4.35: Failure patterns of the 3 reference material models for the grid infill structure.

value of the tests. From the Table it can be seen that material model 2 approximates the solid specimen best. On the other hand, the grid infill structure is best represented by material model 3. However, the results show that material model 1 exhibits the lowest difference in prediction accuracy between the solid specimen and the grid infill specimen.

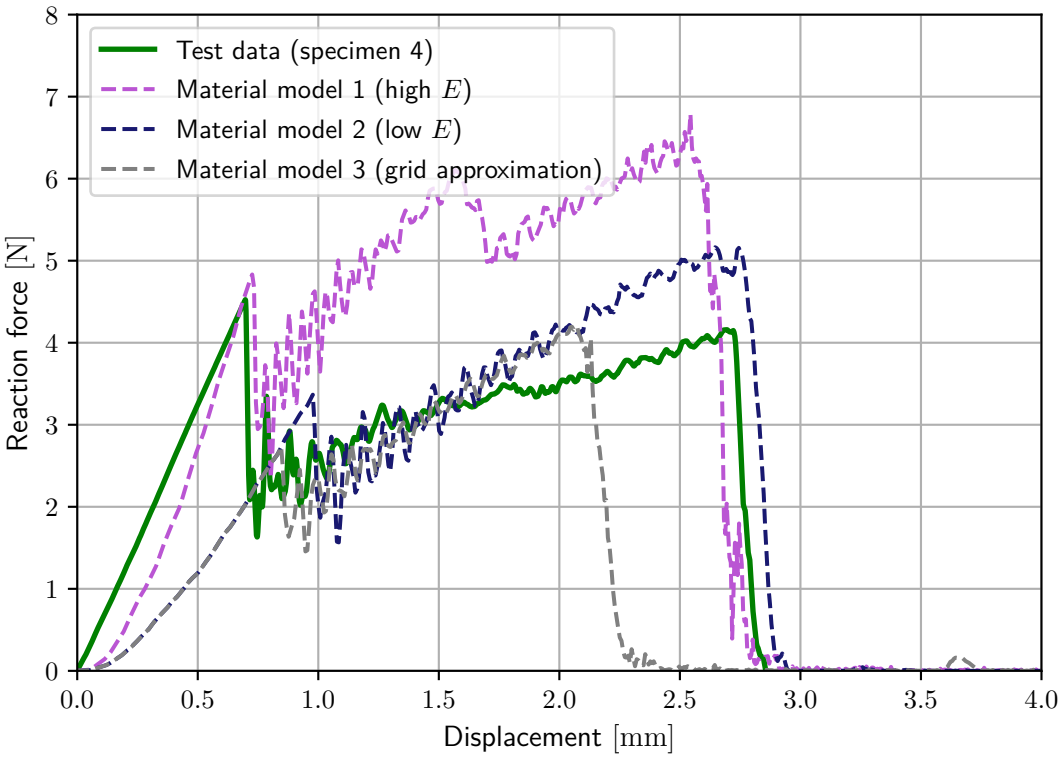


Figure 4.36: Comparison of the representative test curve against all 3 reference material models for the solid specimen

Table 4.14: Comparison of the mean value for dissipated energy of the test results against the results for all 3 reference material models

| Model | Dissipated energy [J] (solid) | Deviation from mean value | Dissipated energy [J] (grid) | Deviation from mean value |
|---|---|---|---|---|
| Mean (test results) | 9.19 | - | 1.54 | - |
| Material model 1 | 11.81 | + 28.51 % | 2.11 | + 37.01 % |
| Material model 2 | 8.49 | − 7.62 % | 4.05 | + 162.99 % |
| Material model 3 | 5.19 | − 43.53 % | 1.75 | + 13.64 % |

## 4.6 Prediction quality of the developed reference material models for varied infill geometries

In this section, the 3 calibrated material models are validated for their prediction quality. For that reason, the impact behaviour of infill geometries different to the solid specimen and the grid infill structure is evaluated. After observing the computed results, the chosen geometries are 3D-printed and tested in order to study how good the impact behaviour of the actual specimens can be predicted using those reference material models. In Figure 4.37, the two chosen infill geometries are shown. Both geometries fulfill the geometric restrictions due to meshing in the model, as mentioned in Section 3.4. These geometries are referred to as pyramid infill structure (Figures 4.37a, 4.37c) and grid-reinforced pyramid infill structure (Figures 4.37b, 4.37d) from now on.

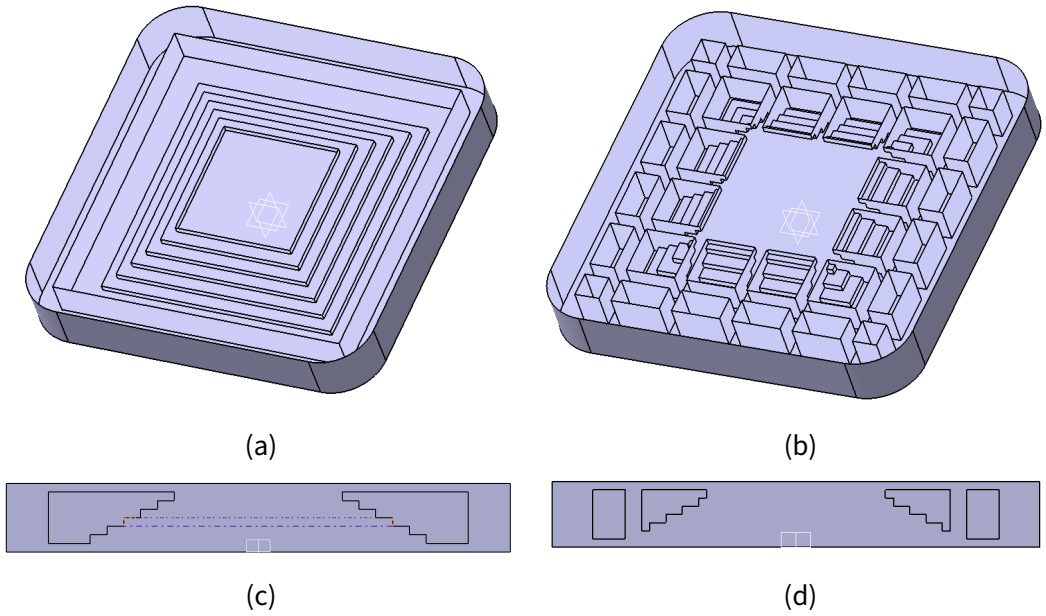


Figure 4.37: Left: Inner structure approximating a pyramid in layers, right: the pyramid infill structure of combined with a grid-reinforcement.

Firstly, the failure patterns for the test specimens (Figure 4.38) with the pyramid infill structure is shown in comparison to the results of the FE-simulation using the 3 material

models (Figure 4.39). It can be seen that the failure pattern for the pyramid structure can be predicted better than for the grid infill structure. Especially the failure pattern using material model 3 looks similar to the failure patterns of test specimens.

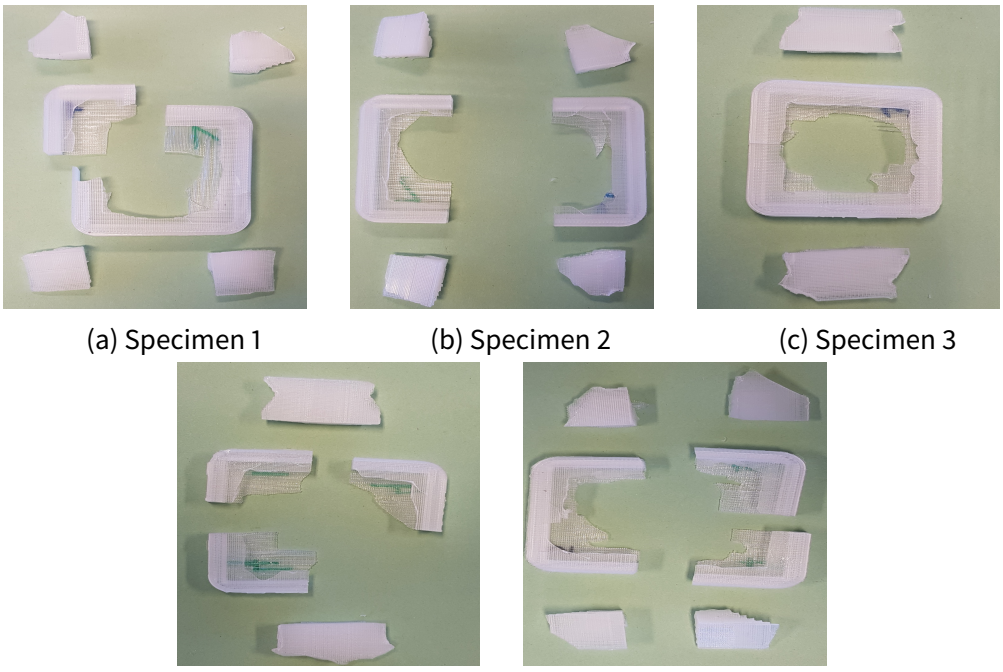

(a) Specimen 1 (b) Specimen 2 (c) Specimen 3

(d) Specimen 4 (e) Specimen 5

Figure 4.38: Failure patterns of the specimens with the pyramid infill geometry.

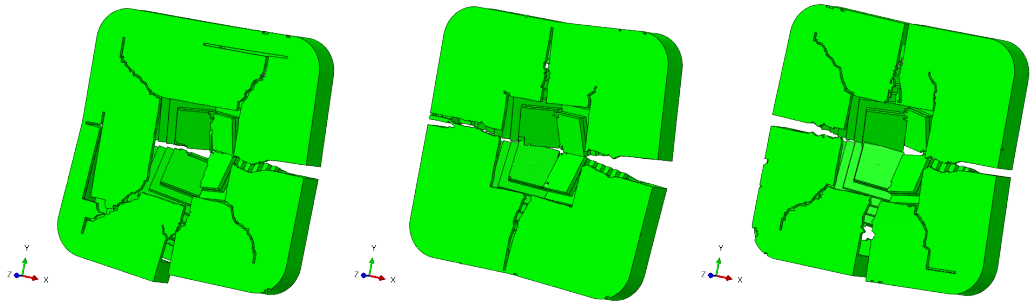

(a) Material model 1 (b) Material model 2 (c) Material model 3

Figure 4.39: Failure patterns of the 3 reference material models for the pyramid infill structure.

As for the pyramid structure, the failure patterns for the test specimens with the grid-reinforced pyramid structure (Figure 4.40) is shown as well as the failure patterns using the material models (Figure 4.41). For the grid-reinforced pyramid infill structure, material model 2 represents the failure patterns of the test specimens best. Material models 1 and 3 do not predict the failure patterns well.

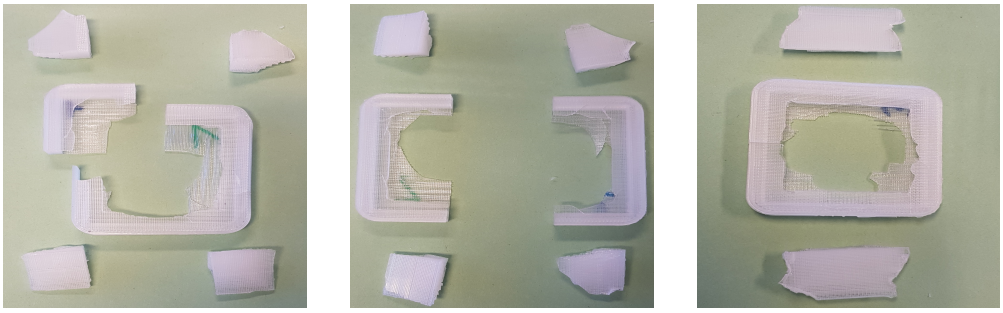

(a) Specimen 1 (b) Specimen 2 (c) Specimen 3

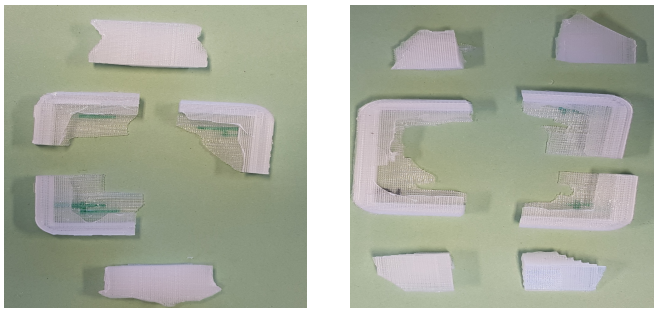

(d) Specimen 4 (e) Specimen 5

Figure 4.40: Failure patterns of the specimens with the grid-reinforced pyramid infill geometry.

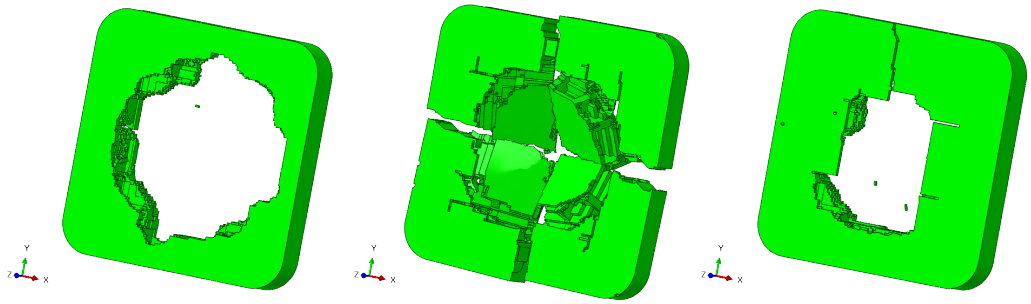

(a) Material model 1 (b) Material model 2 (c) Material model 3

Figure 4.41: Failure patterns of the 3 reference material models for the grid-reinforced pyramid infill structure.

The force-displacement curves of the test specimens with the pyramid infill structure are shown in Figure 4.42a. There seems to be a problem with specimens 2 and 3 as there is still a reaction force at displacements higher than $6\,\mathrm{mm}$. Therefore, those 2 specimens are not considered for the mean value of absorbed energy. The curves of test specimens 1 and 4 are regarded as representative test curves. They are compared to the computed results for the material models in this section. In Table 4.15, the dissipated energy for the test specimens is shown. Leaving the problematic specimens 2 and 3 out, the scatter of the test results for this geometry is lower than for the other geometries.

In Figure 4.42b, the test results for the specimens with the grid-reinforced pyramid infill structure are shown. Again, there is a test which is considered irrelevant regarding dissipated energy (specimen 5). However, the test results are very close to each other except for the mentioned specimen 5. For comparison against the results using the reference material models, the force-displacement curve of specimen 4 is chosen because its absorbed energy is closest to the mean value. The energy dissipated by the test specimens is shown in Table 4.15. For the computation of the mean value, test specimen 5 is ignored.

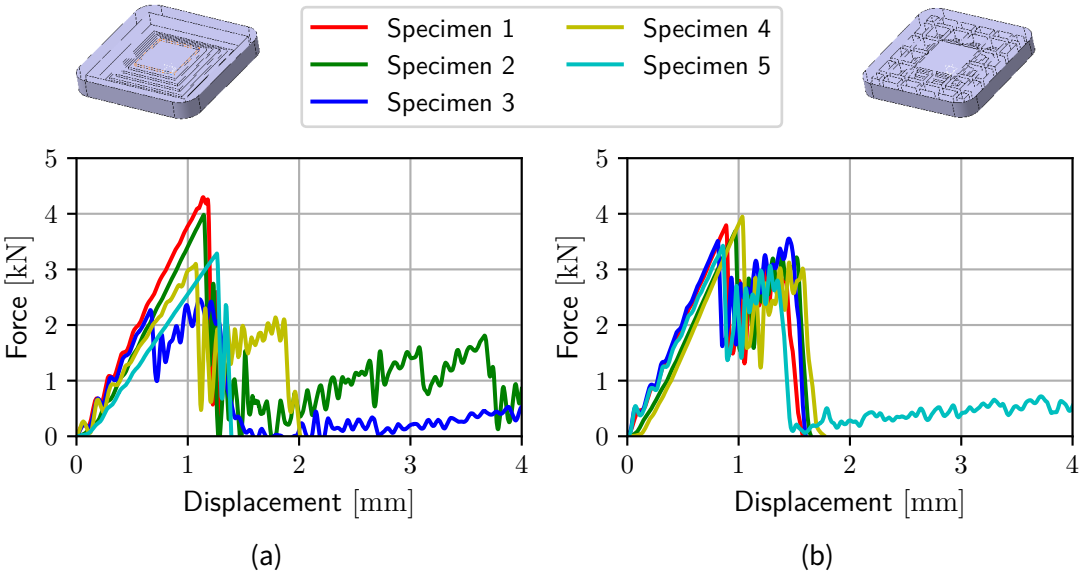


(a) (b)

Figure 4.42: The experimental force-displacement curves for (a) the pyramid infill structure and (b) the grid-reinforced pyramid infill structure.

Table 4.15: Comparison of the absorbed energy for the pyramid infill specimens.

| Specimen | Dissipated energy [J] Pyramid infill | Dissipated energy [J] Grid-reinforced pyramid infill |
|---|---|---|
| 1 | 2.75 | 3.10 |
| 2 | (12.56) | 3.20 |
| 3 | (11.74) | 3.45 |
| 4 | 3.05 | 3.23 |
| 5 | 2.10 | (6.16) |
| Mean | 2.63 | 3.25 |

In Figure 4.43a, the test curves of specimens 1 and 4 with the pyramid infill structure are shown as well as the results using the material models. The slope up to first damage of the test results is in between the different material models. For the computed results, there is a reaction force at displacements above $4\,\mathrm{mm}$, leading to excessive values of dissipated energy. As a consequence, no material model predict the amount of absorbed energy well.

In Figure 4.43b, the test curve of specimen 4 with the grid-reinforced pyramid infill structure is shown together with the computational prediction for the 3 developed material models.

The difference between test specimen 4 and material model 1 is similar to the calibrated curve of material model 1 for the solid specimen. The displacement of abrupt failure is predicted very well. Furthermore, reaction force after first damage is overestimated as for the solid specimen. However, for the grid-reinforced pyramid structure, the slope up to first damage is too steep which results in a higher overestimation of consumed energy compared to the solid specimen.

For material model 2, the reaction force until first damage is underestimated as for the solid specimen. The displacement of first damage is approximated well and the reaction forces after first damage are a good approximation of the test results. Nevertheless, this material model overestimates the dissipated energy because the displacement of final failure is wrongly predicted.

For material model 3, the force-displacement curve up to first damage is not a good prediction of the test data. However, the reaction force after first damage is approximated quite well. As for material model 2, the displacement of final failure is not met closely. As a result of the underestimation for low displacement and overestimation of the displacement at failure, the value for the dissipated energy is close to the test results.

In Table 4.16, the dissipated energy for the material models is shown for the pyramid and the grid-reinforced pyramid infill structure.

Table 4.16: Comparison of the absorbed energy for the pyramid infill specimens using the reference material models.

| Result | Dissipated energy $[\mathrm{J}]$ | Deviation from mean value |
|---|---|---|
| | Pyramid | |
| Mean (test results) | $2.63$ | - |
| Material model 1 | $4.73$ | $+\ 79.85\ \%$ |
| Material model 2 | $5.46$ | $+\ 107.60\ \%$ |
| Material model 3 | $3.83$ | $+\ 45.63\ \%$ |
| | Grid-reinforced pyramid | |
| Mean (test results) | $3.25$ | - |
| Material model 1 | $4.84$ | $+\ 48.92\ \%$ |
| Material model 2 | $5.62$ | $+\ 72.92\ \%$ |
| Material model 3 | $3.36$ | $+\ 3.38\ \%$ |

In Figure 4.44, the difference in energy dissipation of the tests and the predicted computations using the material models is shown. For the pyramid infill structure (Figure 4.44a), the deviation of the computed results from the test results is very high. While material model 2 is closer to the test results for this geometry than for the grid in-

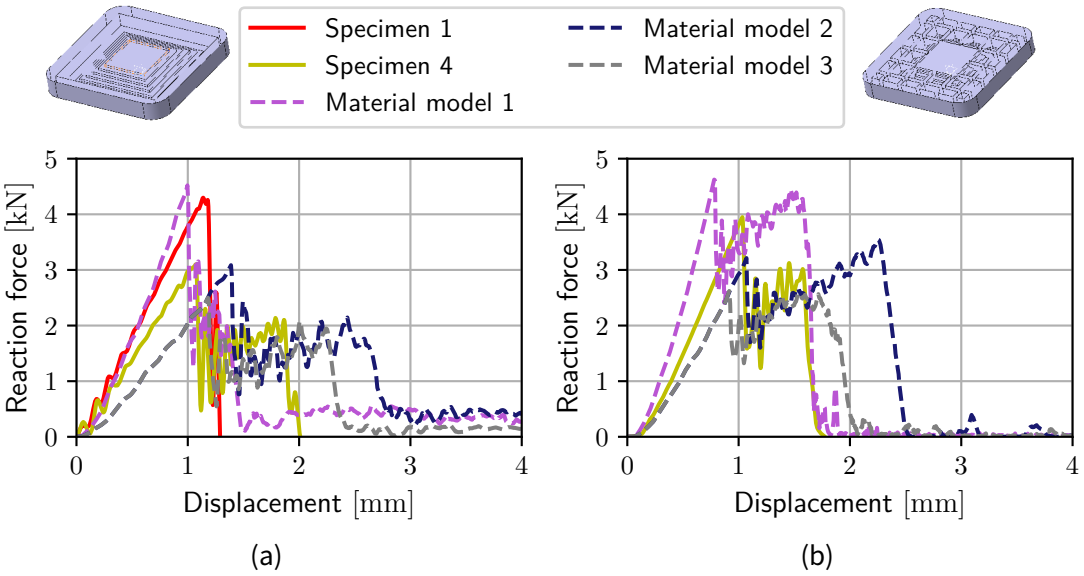


Figure 4.43: Comparison of the experimental vs. the simulation results for the force-displacement curves for (a) the pyramid infill structure and (b) the grid-reinforced pyramid infill structure.

fill structure, the prediction quality of material models 1 and 3 is worse than for the geometrical difference between the solid and the grid infill specimen. For the grid-reinforced pyramid infill structure (Figure 4.44b) the deviation of the dissipated energy compared to the mean value of the test results is less than for the pyramid infill structure.

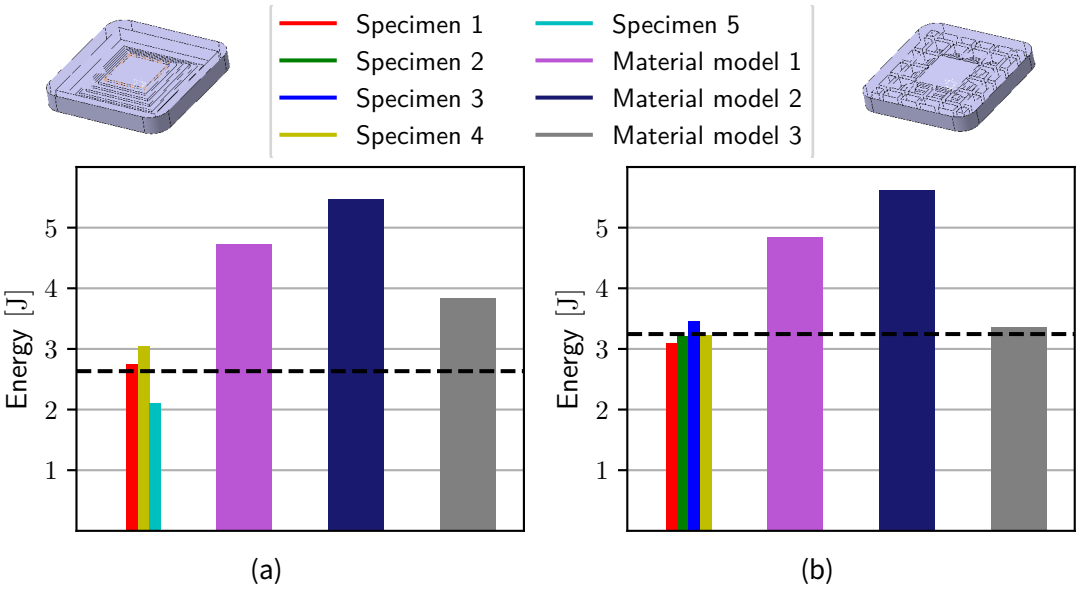


Figure 4.44: The values of absorbed energy for the test specimen and simulation predictions for (a) the pyramid infill structure and (b) the grid-reinforced pyramid infill structure.

## 4.7 Summary and discussion of all results and the prediction quality

In the previous sections, the results for every specimen geometry were discussed in detail. In this section, the overall results are discussed to give an overview of the general prediction quality of the calibrated reference material models. In Figure 4.45, the representative test curves are shown as well as the different results depending on the infill geometry for all 3 material models.

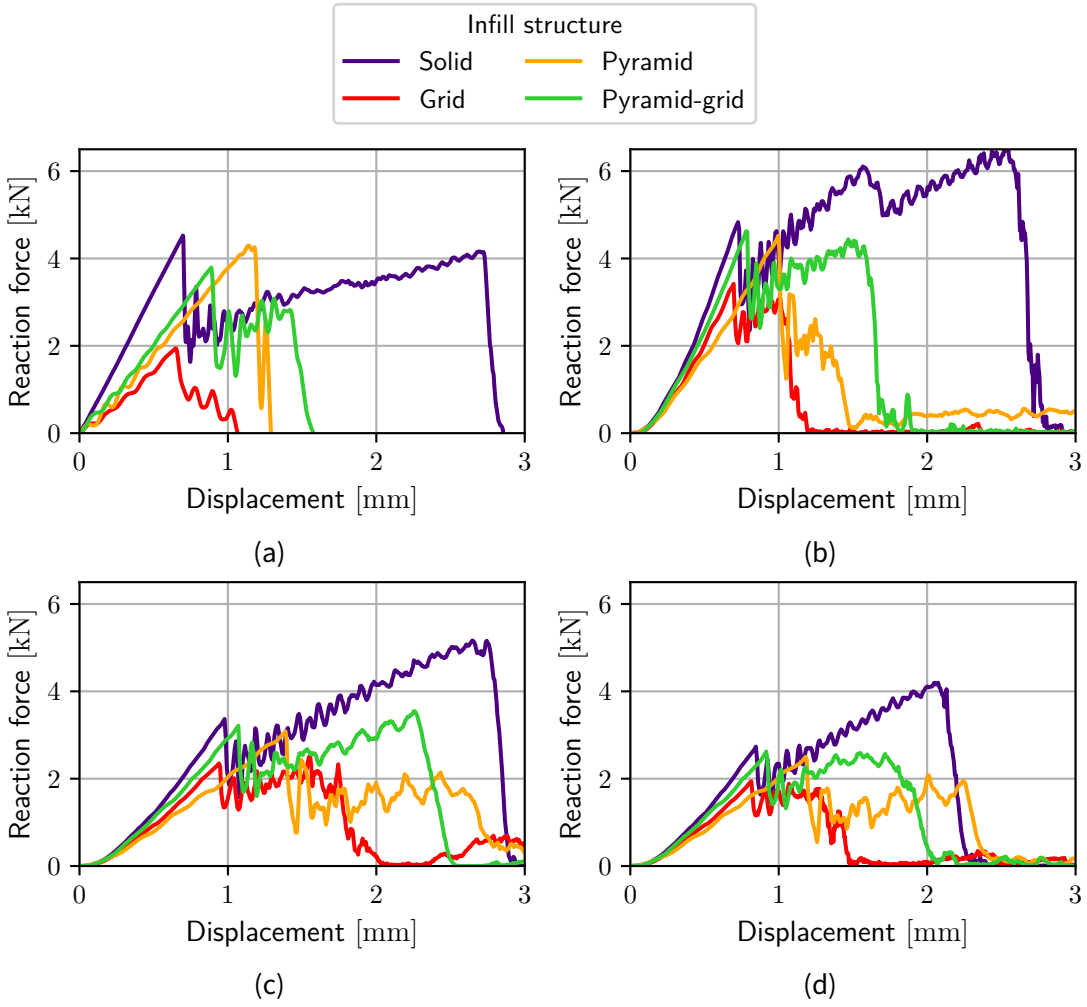


Figure 4.45: The force-displacement curves for (a) the test specimens, (b) material model 1, (c) material model 2 and (d) material model 3.

### 4.7.1 Reference material model 1

This material model is calibrated by manually adjusting the material model parameters to represent the impact behaviour of the solid test specimens. For the solid geometry, the slope up to first damage is slightly underestimated. On the other hand, the force

after first damage is overestimated. The displacement at which abrupt failure occurs is met well. As a consequence, the amount of dissipated energy is overestimated for the solid specimen.

For the grid infill structure, a similar deviation from the test results is shown for reference material model 1. As a difference to the solid specimen, for this geometry also the slope up to first damage is overestimated. The predicted abrupt failure is slightly shifted to a higher displacement compared to the test results. This leads to an overestimation in dissipated energy.

Observing the pyramid infill structure, the force up to first damage is slightly overestimated (compared to specimen 1). The problem in predicting the amount of absorbed energy with this infill structure is that the model displays a reaction force up to very high displacements instead of brittle failure leading to no more reaction force after abrupt failure. This circumstance is the reason for the tremendous overestimation of dissipated energy for this geometry using reference material model 1.

Contrary to the pyramid infill structure, the grid-reinforced pyramid structure shows complete failure using reference material model 1. The force up to first damage and also after first damage is overestimated with this material model. Nevertheless, the displacement of abrupt failure is met well. Altogether, the dissipated energy for the grid-reinforced pyramid structure is overestimated using reference material model 1.

### 4.7.2 Reference material model 2

Reference material model 2 is developed the same way as material model 1. This means that the material model parameters were manually adjusted to approximate the impact behaviour of the solid test specimens. Due to the lower Young's modulus, the slope up to the first peak is underestimated intentionally. As a result, the reaction force after first damage is close to the test values, overestimating the force slightly at higher displacements. The displacement of abrupt failure is met well for the solid specimen.

Predicting the grid infill structure, the force-displacement curve up to first damage is met well using reference material model 2. However, the displacement of abrupt failure is predicted at a higher displacement than the test specimens show. Due to this circumstance, the impact behaviour after first damage using reference material model 2 leads to a tremendous overestimation of dissipated energy.

As for the previous geometries, reference material model 2 underestimates force up to first damage for the pyramid infill structure. Similar to reference material model 1, there is still a reaction force at very high displacements. This leads to a predicted energy dissipation which is by far higher than the test results show.

The difference in force-displacement curves using reference material model 2 for the grid-reinforced pyramid structure is similar to the solid specimen. The slope until first damage is underestimated. On the other hand, the displacement of first damage and

also the force after first damage are predicted well. However, displacement of abrupt failure is higher for the computed results using material model 2 than in the tests. As a result, the computation using material model 2 leads to an overestimation of dissipated energy.

### 4.7.3 Reference material model 3

Contrary to the other reference material models, this material model is developed to approximate the impact behaviour of the grid infill structure test specimens. Therefore, the material model parameters of material model 2 are manually changed to better represent the force-displacement curve of the grid infill structure test specimens. As reference material model 3 is calibrated for the grid infill structure, it represents the tests for this structure best. The force-displacement curve until first damage is met well compared to the test results. However, this material model shows a delayed abrupt failure which results in an overestimation of energy dissipation.

Observing the solid specimen's impact behaviour, the results using material model 3 are close to the results of reference material model 2. The force up to first damage is underestimated, while the force after first damage is close to the representative test curves. Nevertheless, reference material model 3 shows an earlier abrupt failure for the solid specimen than reference material model 2. As a consequence, energy dissipation of the solid specimen is underestimated using this reference material model.

For the pyramid infill structure, force until first damage is overestimated. Similar to the other reference material models, reference material model 3 shows no complete failure resulting in predicted force up to high displacements. Therefore, the amount of energy absorbed is overestimated by a high extent.

Predicting the grid-reinforced pyramid structure, force up to first damage is underestimated using reference material model 3. Nevertheless, force after first damage is predicted well. Abrupt failure is predicted at a higher displacement than the test specimens show. The result of underestimation up to first damage and overestimation due to the delayed abrupt failure is a value for energy dissipation very close to the mean of the test data.

### 4.7.4 Overview of the prediction quality of the reference material models

In Table 4.17, the predicted energy dissipation for all geometries is listed for the material models. This data is also visualized in Figure 4.46. For a better overview, the geometries in the Figure are arranged in decreasing order of dissipated energy for the mean value of the test results. Because of this arrangement, it can be easily seen whether the reference material models give a qualitatively correct prediction or not.

For material models 1 and 2, the predicted energies are decreasing for the different geometries in the same order as the test results. Therefore, those 2 material models give

a qualitatively correct prediction. This is not true for material model 3, as the pyramid infill structure is predicted to dissipate more energy than the grid-reinforced pyramid structure, which is contrary to the test results. However, quantitatively, material model 3 is the most accurate for all different infill structures with the solid specimen being an exception. As said, material model 3 was developed to represent the grid infill structure test results. Using this material model, a similar infill structure – the grid-reinforced pyramid – can be predicted well. Altogether, reference material model 1 is the best for a qualitative prediction. The deviation from the mean values does not vary as much as for the other reference material models. Especially when leaving out the problematic pyramid infill structure, the overestimation of energy is in a range in which the real energy dissipation can be estimated quite well when considering an approximate deviation of about $30$ to $40\,\%$.

Table 4.17: Overview of the predicted energy dissipation for all geometries.

| Geometry | Mean (test scatter) | Material model 1 | Material model 2 | Material model 3 |
|---|---|---|---|---|
| Solid | $9.19$ J<br>$+ 26.4\,\%$<br>$- 37.2\,\%$ | $11.81$ J<br>$+ 28.5\,\%$ | $8.49$ J<br>$- 7.6\,\%$ | $5.19$ J<br>$- 43.5\,\%$ |
| Grid | $1.54$ J<br>$+ 69.5\,\%$<br>$- 42.2\,\%$ | $2.11$ J<br>$37.0\,\%$ | $4.05$ J<br>$+ 163.0\,\%$ | $1.75$ J<br>$+ 13.6\,\%$ |
| Pyramid | $2.63$ J<br>$+ 16.0\,\%$<br>$- 20.2\,\%$ | $4.73$ J<br>$+ 79.9\,\%$ | $5.46$ J<br>$+ 107.6\,\%$ | $3.83$ J<br>$+ 45.6\,\%$ |
| Grid - Pyramid | $3.25$ J<br>$+ 6.2\,\%$<br>$- 4.6\,\%$ | $4.84$ J<br>$+ 48.9\,\%$ | $5.62$ J<br>$+ 72.9\,\%$ | $3.36$ J<br>$+ 3.4\,\%$ |

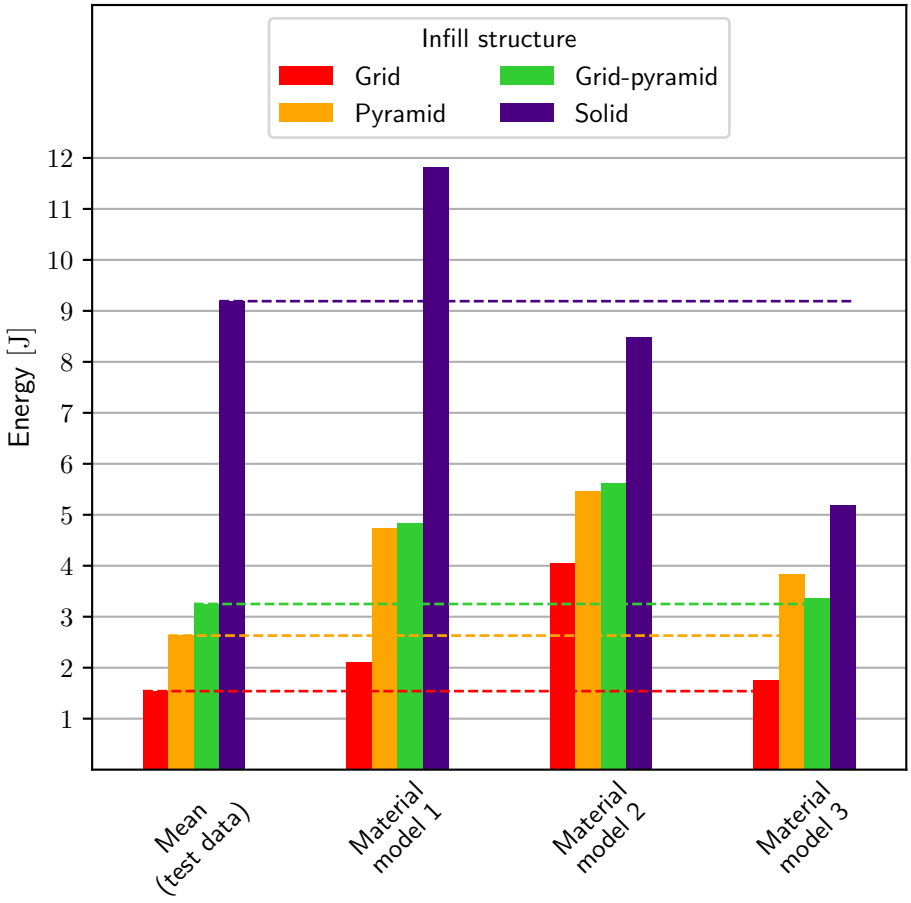


Figure 4.46: Overview of all predicted energy dissipation values compared to the test results.

# 5 Conclusion

The goal of this thesis was to predict the impact behaviour of 3D-printed PMMA test specimens with varied infill geometries. Therefore, the test setup is reproduced in a finite element model and 3 different material models including a brittle damage model were developed. The main difficulty is that either the test data up to first damage or after first damage can be approximated well. Unfortunately, approximating the whole range in the force-displacement curve until absolute failure is not possible. The cause might be the assumptions made for the material model (i.e. an isotropic and linear-elastic material law).

Two of the material models give a correct qualitative prediction of whether an infill geometry dissipates more energy during the test than another. In terms of quantitative prediction of the absorbed energy, all material models differ too much from the test data to give a useful prediction. One material model, however, overestimates the amount of dissipated energy in a range which allows to manually have a rather useful guess of the actual energy dissipation.

In general, the brittle damage model in ABAQUS is highly adjustable. However, defining a linear-elastic and isotropic material law is mandatory for using the brittle damage model. The 3D printing process, on the other hand, leads to anisotropic material properties as there are weld lines between the extruded strands of material. In that respect, the combination of material and damage model in ABAQUS is limited. That circumstance does not allow the precise prediction of the impact behaviour of 3D-printed polymer parts.

Additionally, the geometries modelled are the original designs of the infill structure constructed in a CAD software. Representing the real geometry of the 3D printed parts as a result of the 3D-printer placing the polymer strand could lead to more accurate results. As a big disadvantage of exactly representing the real geometry, the refinement of the geometry to model the real geometry of a 3D-printed part would lead to finer features which require a finer mesh and therefore need a lot of computational time.

Summed up, the impact behaviour of 3D-printed PMMA test specimens can not be accurately predicted with the considerations made in this thesis for a time-efficient FE model. The tests for the solid specimens show that the material properties and failure patterns are dependent on the extrusion direction and the weld lines within the specimens. Using this information, an anisotropic material law considering the extrusion direction of the strands and the effects of the weld lines could reproduce the impact behaviour of the specimens better. However, the combination of an anisotropic mate-

rial law and the brittle damage model had to be implemented in ABAQUS. Then, the effects of the manufacturing process on the material behaviour could be taken into account to a higher extent.

# List of Tables

# List of Figures

# References


1. Puska M., e. a. *Polymer Composites for Bone Reconstruction* chap. 3 (IntechOpen, Rijeka, 2011).
2. Wintermantel, E. & Ha, S.-W. *Medizintechnik: Life Science Engineering ; Interdisziplinarität, Biokompatibilität, Technologien, Implantate, Diagnostik, Werkstoffe, Zertifizierung, Business* (Springer, Berlin and Heidelberg, 2009).
3. Gebhardt, A., Kessler, J. & Thurn, L. *3D-Drucken: Grundlagen und Anwendungen des Additive Manufacturing (AM)* (Hanser, München, 2016).
4. Rosenzweig, D. H., Carelli, E., Steffen, T., Jarzem, P. & Haglund, L. 3D-Printed ABS and PLA Scaffolds for Cartilage and Nucleus Pulposus Tissue Regeneration. *International journal of molecular sciences* **16,** 15118–15135 (2015).
5. Ridwan-Pramana, A. *et al.* Finite element analysis of 6 large PMMA skull reconstructions: A multi-criteria evaluation approach. *PLOS ONE* **12,** 1–16 (2017).
6. Huang, G. J. *et al.* Craniofacial reconstruction with poly(methyl methacrylate) customized cranial implants. *The Journal of craniofacial surgery* **26,** 64–70 (2015).
7. Kim, B.-J. *et al.* Customized cranioplasty implants using three-dimensional printers and polymethyl-methacrylate casting. *Journal of Korean Neurosurgical Society* **52,** 541–546 (2012).
8. Petersmann, S. *et al.* Impact Optimization of 3D–Printed Poly(methyl methacrylate) for Cranial Implants. *Macromolecular Materials and Engineering* **40,** 1900263 (2019).
9. *Önorm DIN EN ISO 6603:2-2002. Plastics – Determination of puncture impact behaviour of rigid plastics* Standard (Austrian Standards, Vienna, AT, Apr. 2002).
10. Polzin, C., Spath, S. & Seitz, H. Characterization and evaluation of a PMMA-based 3D printing process. *Rapid Prototyping Journal* **19** (Jan. 2013).
11. Steinbuch, R. *Finite Elemente - Ein Einstieg* (Springer, Berlin and Heidelberg, 1998).
12. Roth, S., Chamoret, D., Imbert, J. & Gomes, S. *Crash FE Simulation in the Design Process - Theory and Application* (Sept. 2011).
13. *ABAQUS Documentation* `https://abaqus-docs.mit.edu/2017/English/SIMACAEEXCRefMap/simaexc-c-docproc.htm`. Accessed: 2019-11-25.
14. Harewood, F. J. & McHugh, P. E. Comparison of the implicit and explicit finite element methods using crystal plasticity. *Computational Materials Science* **39,** 481–494 (2007).
15. *Implicit vs Explicit FEM* `https://www.simscale.com/blog/2019/01/implicit-vs-explicit-fem/`. Accessed: 2019-10-21.

16. Puri, G. *Python scripts for Abaqus: Learn by example* (abaquspython.com, Charleston, SC, 2011).
17. Ehrenstein, G. W. *Mit Kunststoffen konstruieren* (Hanser, München, 2007).
18. Koltzenburg, S., Maskos, M. & Nuyken, O. *Polymer Chemistry* (Springer Berlin Heidelberg, Berlin, Heidelberg, 2017).
19. Kaiser, W. *Kunststoffchemie für Ingenieure: Von der Synthese bis zur Anwendung* (Carl Hanser Fachbuchverlag, s.l., 2011).
20. Seidler, S., Altstädt, V. & Grellmann, W. *Polymer testing* 2nd edition (Hanser Publishers, Munich, 2013).
21. Lemaitre, J. *A Course on Damage Mechanics* Second Revised and Enlarged Edition (Springer, Berlin and Heidelberg, 1996).
22. Kondo, D., Welemane, H. & Cormery, F. Basic concepts and models in continuum damage mechanics. *Revue européenne de génie civil* **11,** 927–943 (Oct. 2007).
23. Hooke, R. *Lectures de Potentia Restitutiva, Or of Spring Explaining the Power of Springing Bodies* (John Martyn, 1678).
24. Lemaitre, J. & Chaboche, J.-L. *ASPECT PHENOMENOLOGIQUE DE LA RUPTURE PAR ENDOMMAGEMENT* in (1978).
25. Kuna, M. *Finite Elements in Fracture Mechanics: Theory - Numerics - Applications* (Springer Netherlands, Dordrecht and s.l., 2013).
26. Barenblatt, G. in (eds Dryden, H., von Kármán, T., Kuerti, G., van den Dungen, F. & Howarth, L.) 55–129 (Elsevier, 1962).
27. Khan, A., Iqbal, N., Saeed, H. & Tarar, W. Development of material model for assessment of brittle cracking behavior of plexiglas. *IOP Conference Series: Materials Science and Engineering* **146,** 012008 (Aug. 2016).
28. Baumann, F., Bugdayci, H., Grunert, J., Keller, F. & Roller, D. Influence of slicing tools on quality of 3D printed parts. *Computer-Aided Design and Applications* **13,** 14–31 (2016).
29. Stommel, M., Stojek, M. & Korte, W. *FEM zur Berechnung von Kunststoff- und Elastomerbauteilen* German (Hanser, München, 2011).